Alma Mater Studiorum – Università di Bologna

DOTTORATO DI RICERCA IN

CHIMICA

Ciclo 35

**Settore Concorsuale:** 03/A2 - MODELLI E METODOLOGIE PER LE SCIENZE CHIMICHE

**Settore Scientifico Disciplinare:** CHIM/02 - CHIMICA FISICA

# ROTATIONAL AND RO-VIBRATIONAL ANALYSES OF MOLECULES OF ASTROCHEMICAL INTEREST

**Presentata da:** Ningjing Jiang

**Coordinatore Dottorato**

Prof. Luca Prodi

**Supervisore**

Prof.ssa Cristina Puzzarini

**Co-supervisore**

Dott. Mattia Melosso

**Esame finale anno 2023**

# Contents

# Chapter 1

# Introduction

The topic of this thesis is the application of spectroscopy to astrochemistry. In particular, it concerns different spectroscopic studies that can support the investigation of the chemical composition of astronomical objects such as molecular clouds and planetary atmospheres.

## 1.1 Spectroscopy

Spectroscopy is the field that investigates the interaction between radiation and matter: absorption, emission, and scattering of electromagnetic radiation as a function of its frequency. Molecular spectroscopy is that part of spectroscopy where matter is a molecular system.

Spectroscopy has been applied to a wide range of scientific and technical fields. For instance, radio-frequency spectroscopy of nuclei in magnetic fields has been used in the magnetic resonance imaging (MRI) technique, which enables high-resolution imaging of the body tissues. Microwave spectroscopy is largely employed in the structural characterization of isolated molecules. The spectroscopic techniques employing high-energy particle accelerators are applied to explore the intrinsic structure of protons and neutrons, as well as the state of the early universe. Moreover, optical, radio, and X-ray spectroscopy can be used to identify interstellar molecules, the composition of stars, and even the amount of primordial abundance of the elements prior to star formation.

The different spectroscopic techniques are usually classified according to the portion of the electromagnetic spectrum involved. The different regions of the electromagnetic spectrum are classified into radio/TV, microwave (MW), infrared (IR), visible (VIS), ultraviolet (UV), X-ray, and $\gamma-$ray regions, as shown in Table 1.1.1.

Table 1.1.1: Regions of the electromagnetic spectrum.

| Region | Wavelength | Frequency | Properties |
|---|---|---|---|
| Radio/TV | 1 m and more | 300 MHz and below | Nuclear spin transitions |
| Microwave | 1 mm - 1 m | 300 MHz – 300 GHz | Molecular rotations; Electron spin transitions |
| Infrared | 700 nm -1 mm | 300 GHz – 430 THz | Molecular vibrations |
| Visible | 400 nm – 700 nm | 430 THz – 750 THz | Valence electron transitions |
| Ultraviolet | 10 nm – 400 nm | 750 THz – 30 PHz | Valence electron transitions |
| X-ray | 0.01 nm – 10 nm | 30 PHz – 30 EHz | Inner-shell electron transitions |
| $\gamma$-ray | less than 0.01 nm | more than 30 EHz | Nuclear energy transitions |

Two of the regions above, MW and IR, have been considered in this thesis. The corresponding spectroscopic techniques are rotational spectroscopy and (ro-)vibrational spectroscopy, respectively. The former type of spectroscopy investigates the rotational motion of molecules in the gas phase. Rotational transitions occur as the result of the interaction between the molecular electric dipole moment and the electromagnetic field of the radiation. A pure rotational transition takes place between two energy levels belonging to same vibrational state, while a ro-vibrational transition occurs between two rotational energy levels that belong to different vibrational states.

Recording and analyzing rotational and ro-vibrational spectra have been the major activities performed during my PhD. For the purpose of this thesis, it has to be noted that the so-called far-IR (FIR) region, which covers the frequencies from 300 GHz to 3 THz, is also denoted as submillimeter-wave range. Both rotational and ro-vibrational transitions can lie in this frequency range.

## 1.2 Astrochemistry

Astrochemistry is the study of the chemistry that occurs across the universe, with the detection of interstellar molecules being essential to understand cosmic evolution toward molecular complexity [1]. The census of interstellar molecular species currently exceeds 270 different species [2–6], and includes radicals, ions, and organic molecules. Among these, the discoveries of complex organic molecules (COMs) and potentially prebiotic species have further stimulated the search of the building blocks of life in the universe and the attempt of understanding of how they form.

Most of interstellar molecules have been discovered by observations of their rotational transitions, while a small number of them have been identified by optical or IR observations of their electronic or ro-vibrational spectra [5, 7]. Radio astronomy is thus the most powerful technique for the identification of individual molecules in the ISM. The Atacama Large Millimeter/submillimeter Array (ALMA) [8] is one of the most powerful facility for the observation of molecular signatures in a variety of astrophysical objects, including remote galaxies and planets. With ten different bands (from 0.32 to 3.6 mm), ALMA covers a spectral window wherein most of the rotational transitions fall, thus allowing to probe a great variety of chemicals: from light to medium-sized molecules. However, the assignment of radio astronomical spectra requires the accurate knowledge of the spectroscopic features of the molecules present in the astronomical object under consideration [5, 7]. This implies that these molecules have been investigated in the laboratory, which means that the rotational (or ro-vibrational) spectrum is recorded and analyzed. Currently, hundreds of features in the astronomical spectral surveys taken with ALMA or other powerful radio telescopes such as Yebes [9] are still not assignable to molecules already studied in the laboratory. This thus leads to the need of spectroscopic investigations in the millimeter/submillimeter-wave (mm/submm-wave) region for "new" molecular species.

However, radio telescopes are completely blind to molecules that have no permanent electric dipole moment. For instance, the atmospheres of several planets, such as Mars and Titan, have large amounts of $CH_4$, which cannot be observed through radio telescopes (as it will be made clear in Chapter 2). In addition, radio telescopes can only detect species that are in the gas phase. IR telescopes are thus powerful tools for the discovery of molecules that cannot be studied with rotational spectroscopy and for those that are in condensed phases.

Since the Earth atmosphere is not transparent to IR radiation, vibrational and ro-vibrational features are "captured" by space IR telescopes such has the James Webb Space Telescope (JWST), which has been launched on the Christmas day 2021 as a follow-on mission to the Hubble Space Telescope. The JWST has on board three high-sensitivity IR spectrographs and the first spectacular images have already been provided.

## 1.3 Outline

The main topic of this thesis is the investigation of the rotational and ro-vibrational spectra of selected molecules of astrophysical importance. This required the recording and analysis of

spectra in the mm/submm-wave, FIR, and mid-infrared (MIR) regions. The structure of this thesis is as follow:

- **Chapter 2** focuses on the fundamentals of molecular spectroscopy, the focus being on rotational spectroscopy and ro-vibrational spectroscopy. The basic concepts of the Measured Active Rotational–Vibrational Energy Levels (MARVEL) approach are also provided.

- **Chapter 3** describes the spectrometers used during the PhD research work: the millimeter-/submilimeter-wave spectrometer and the Fourier-transform IR spectrometer at the University of Bologna. The largest part of my research has been carried out with the former spectrometer, which is located at the Department of Chemistry "Giacomo Ciamician" of the University of Bologna.

- **Chapter 4** presents the most important systems investigated during my thesis work. The investigated molecules that will be addressed are: $H_2CO$, HDS, $DC_3N$, $HC_3N$, $NH_2CH_2CN$, $CH_2{=}CH{-}CH{=}NH$ and $CH_2{=}CH{-}N{=}CH_2$. These last two species are unstable and the strategies for their production "on-the-fly" will be also presented.

- **Chapter 5** reports the concluding remarks of my work.

# Chapter 2

# Theory

## 2.1 Rotational Spectroscopy

### 2.1.1 Molecular rotation

At the first degree of approximation, the rotational motion of a molecule can be described as that of a rigid body. The associate energy $E$ is a function of the angular velocity vector $\boldsymbol{\omega}$ and parametrically depends on the moment of inertia tensor $\mathbf{I}$ which describes the size and mass distribution of the rotating system

$$E = \frac{1}{2}\boldsymbol{\omega}^T \mathbf{I} \boldsymbol{\omega} \,, \tag{2.1}$$

where the superscript $T$ denotes matrix and vector transposition. The moment of inertia is a $3 \times 3$ matrix whose elements are defined in terms of the mass and coordinates of all $N$ particles which compose the system. They are:

- diagonal elements, also called "moments of inertia"

$$I_{\alpha\alpha} = \sum_i^N m_i \left( r_{\beta i}^2 + r_{\gamma i}^2 \right) \,, \tag{2.2}$$

- off-diagonal elements, also called "products of inertia"

$$I_{\alpha\beta} = -\sum_i^N m_i r_{i\alpha} r_{i\beta} \,, \tag{2.3}$$

where $m_i$ is the mass of the $i$-th particle, $r_{i\alpha}$ its coordinate, and $\alpha, \beta, \gamma = x, y, z$, cyclically. In

principle, the choice of the coordinate system is immaterial for the description of the energy, but the most convenient approach is the one in which the origin is located at the center of mass of the system, and the axis orientation is such that the products of inertia, defined by Equation (2.3), are all vanishing.

Adopting this particular choice, called "principal axis system" (hereafter PAS), Equation (2.1) becomes

$$E = \frac{J_x^2}{2I_x} + \frac{J_y^2}{2I_y} + \frac{J_z^2}{2I_z} \,, \tag{2.4}$$

in which $I_\alpha$ represent the non-zero diagonal elements of the principal inertial tensor, and $J_\alpha$, the $\alpha$ component of the rotational angular momentum, defined as

$$J_\alpha = I_\alpha \, \omega_\alpha^2 \,. \tag{2.5}$$

Conventionally, the body-fixed PAS coordinate $(x, y, z)$ is relabeled as $(a, b, c)$, and its order is defined in such a way that for the three principal moments of inertia it holds

$$I_a \leq I_b \leq I_c \,. \tag{2.6}$$

A rotating system can be classified in terms of the relative relations among the three principal moments of inertia $I_\alpha$. If two such components are equal and the third is non-zero the system is classified as "symmetric rotor", for which two different cases exist:

- prolate (cigar-shaped) symmetric rotor, when $I_c = I_b > I_a$ ,
- oblate (disk-shaped) symmetric rotor, when $I_c > I_b = I_a$ .

Any molecule which possesses (at least) a three-fold symmetry axis enters this classification. Figure 2.1.1 depicts two prototypical examples of prolate and oblate symmetric molecules: fluoromethane ($CH_3F$), in which carbon and fluorine atoms lie on the symmetry axis, is prolate, whereas boron trichloride ($BCl_3$), with three heavy off-axis chlorine atoms, is oblate. If the three moments of inertia are equal one another ($I_a = I_b = I_c$), then the rotor is a spherical one and it is of no interest in rotational spectroscopy because such a high symmetry implies a null dipole moment along each inertial axis.

A linear molecule, is a special case of the prolate symmetric rotor, for which there is no mass contribution outside the $\infty$-fold symmetry axis, thus yielding $I_a = 0, I_b = I_c \neq 0$. A classical example is HCN, shown in Figure 2.1.2. In the most general molecular case, there

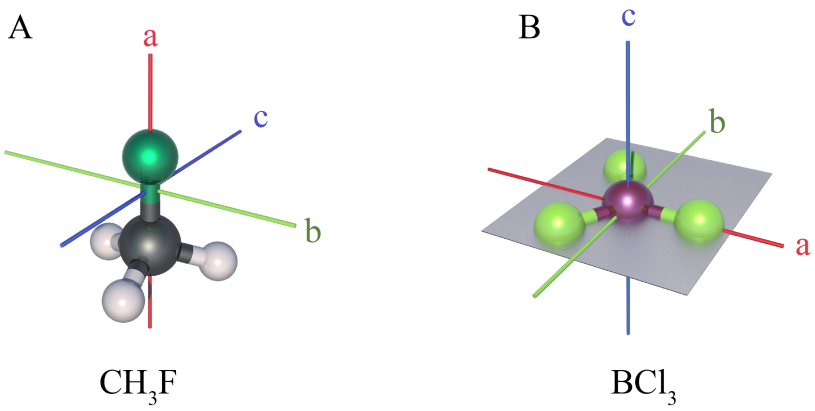


Figure 2.1.1: Principal inertial axes of fluoromethane (A) and boron trichloride (B).

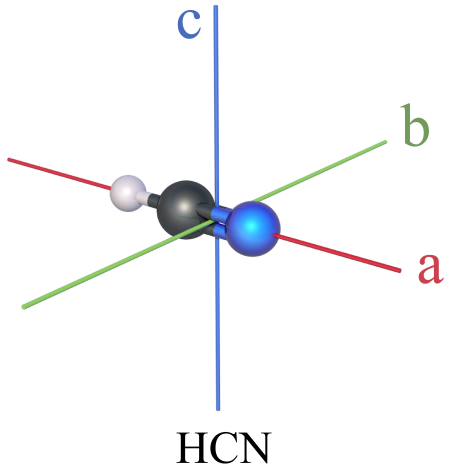


Figure 2.1.2: Principal axes of inertia of inertia of HCN.

is no special relation among the principal moments of inertia, and they are all three non-zero $I_a \neq 0 \neq I_b \neq I_c \neq 0$.

### 2.1.2 Euler angles

A convenient way to describe the rotation of a system in space is to introduce a minimal set of angles $(\theta, \phi, \chi)$ defining the orientation of the reference axis system attached to the molecular frame $(x, y, z)$ with respect to the one fixed in space $(X, Y, Z)$. These three rotation coordinates are called Euler angles and are depicted in Figure 2.1.3.

The space- and molecule-fixed systems can be connected by employing the following trans-

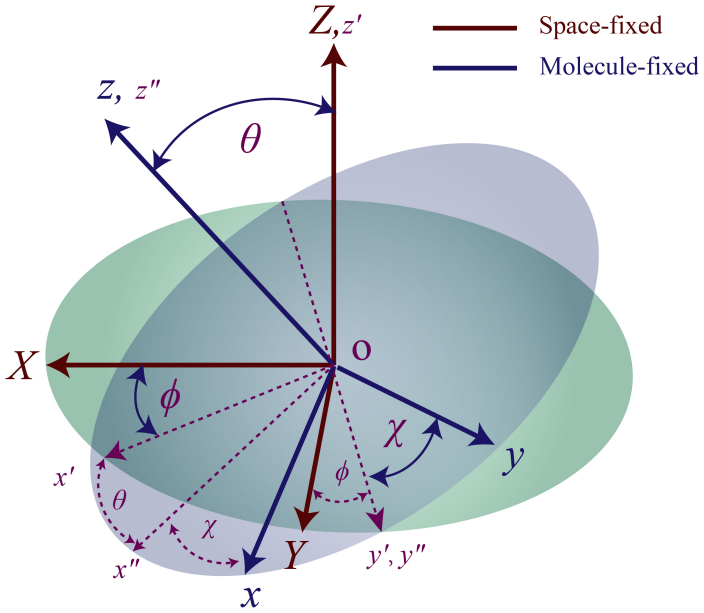


Figure 2.1.3: Euler angles $\theta, \phi, \chi$ (rotational coordinates) related the molecule-fixed and space-fixed reference system. Rotation around $Z$ by $\phi$ to $(x', y', z')$; rotation around $y'$ by $\theta$ to $x'', y'', z''$; rotation around $z''$ by $\chi$ to $(x, y, z)$.

formation:

$$\begin{bmatrix} x \\ y \\ z \end{bmatrix} = R_z(\chi) R_{y'}(\theta) R_z(\phi) \begin{bmatrix} X \\ Y \\ Z \end{bmatrix}, \tag{2.7}$$

that is, three successive rotations by $(\phi, \theta, \chi)$ about the axis $z$, $y'$, and the transformed $z$, respectively. Such an operator product is equivalent to a vector transformation through the following $3 \times 3$ orthogonal matrix

$$\begin{aligned} & R_z(\chi) R_{y'}(\theta) R_z(\phi) = \\ & \begin{bmatrix} \cos\phi\cos\theta\cos\theta - \sin\phi\sin\chi & \sin\phi\cos\theta\cos\chi + \cos\phi\sin\chi & -\sin\theta\cos\chi \\ -\cos\phi\cos\theta\sin\chi - \sin\phi\cos\chi & -\sin\phi\cos\theta\sin\chi + \cos\phi\cos\chi & \sin\theta\sin\chi \\ \cos\phi\sin\theta & \sin\phi\sin\theta & \cos\theta \end{bmatrix} \\ & = \Phi(\phi, \theta, \chi), \end{aligned} \tag{2.8}$$

whose elements are called direction cosines.

### 2.1.3 Quantum mechanical treatment

The quantum formulation of the rotational energy is obtained by replacing the classical expression of the angular momenta with the corresponding quantum operators ($\hat{J}_\alpha$) which, in turn, can be derived from the well known expression of the linear momentum operators $p_\alpha$ by recalling that:

$$\mathbf{J} = \mathbf{r} \times \mathbf{p}\,, \quad \text{and} \quad \hat{\mathbf{p}} = (\hbar/\mathrm{i})\boldsymbol{\nabla}\,, \tag{2.9}$$

where $\boldsymbol{\nabla}$ is the gradient operator whose cartesian components are

$$\boldsymbol{\nabla} = \frac{\partial}{\partial x}\hat{\mathbf{x}} + \frac{\partial}{\partial y}\hat{\mathbf{y}} + \frac{\partial}{\partial z}\hat{\mathbf{z}}\,, \tag{2.10}$$

where $\hat{\mathbf{x}}, \hat{\mathbf{y}}, \hat{\mathbf{z}}$ are unit cartesian vectors. It results:

$$\hat{J}_\alpha = \beta\,\hat{p}_\gamma - \gamma\,\hat{p}_\beta = -\mathrm{i}\left(\beta\frac{\partial}{\partial\gamma} - \gamma\frac{\partial}{\partial\beta}\right)\,, \quad \alpha,\beta,\gamma = x,y,z\,, \quad \text{cyclically}\,. \tag{2.11}$$

The square of the angular momentum is defined as

$$\hat{\mathbf{J}}^2 = \hat{J}_x^2 + \hat{J}_y^2 + \hat{J}_z^2\,; \tag{2.12}$$

such operator has the following commutation properties[1]

$$[\hat{\mathbf{J}}^2, \hat{J}_\alpha] = 0\,, \quad [\hat{J}_\alpha, \hat{J}_\beta] = \mathrm{i}\hat{J}_\gamma\,, \quad \alpha,\beta,\gamma = x,y,z\,, \quad \text{cyclically}\,. \tag{2.13}$$

That is, the square of the angular momentum commutes with any of its components, whereas two different components of $\hat{\mathbf{J}}$ do not commute.

Following standard quantum mechanical theory [10], it can be shown that there exist states $|J, M\rangle$ that are simultaneous eigenfunctions of $\hat{\mathbf{J}}^2$ and any component (but only one) of $\hat{\mathbf{J}}$, say

[1] In quantum mechanics, the commutator of two operators $\hat{A}$ and $\hat{B}$ is defined as $[\hat{A}, \hat{B}] = \hat{A}\hat{B} - \hat{B}\hat{A}$. Two operators "commute" when $[\hat{A}, \hat{B}] = 0$, in this case it can be shown that they share a common set of eigenfunctions. For details see Ref. [10].

$\hat{J}_Z$ . The relevant non-vanishing matrix elements are:

$$\langle J, M|\hat{\mathbf{J}}^2|J', M'\rangle = J(J+1)\,\delta_{J,J'}\delta_{M,M'}\,, \tag{2.14}$$

$$\langle J, M|\hat{\hat{J}}_Z|J', M'\rangle = M'\,\delta_{J,J'}\delta_{M,M'}\,, \tag{2.15}$$

$$\langle J, M|\hat{\hat{J}}_X|J', M'\rangle = \tfrac{1}{2}[J(J+1) - M'(M'\pm 1)]^{1/2}\,\delta_{J,J'}\delta_{M,M'\pm 1}\,, \tag{2.16}$$

$$\langle J, M|\hat{\hat{J}}_Y|J', M'\rangle = \mp \mathrm{i}\tfrac{1}{2}[J(J+1) - M'(M'\pm 1)]^{1/2}\,\delta_{J,J'}\delta_{M,M'\pm 1}\,, \tag{2.17}$$

where $\delta_{A,B}$ represents the Kronecker delta function.

By replacing the angular momentum components with the corresponding operators in the Equation (2.4), one gets the general expression of the quantum mechanical Hamiltonian for a rigid rotor:

$$\hat{H}_{\mathrm{r}} = \frac{1}{2I_x}\hat{J}_x^2 + \frac{1}{2I_y}\hat{J}_y^2 + \frac{1}{2I_z}\hat{J}_z^2\,. \tag{2.18}$$

Once the appropriate relabelling ($x, y, x \to a, b, c$) is made, the above equation becomes

$$\hat{H}_{\mathrm{r}} = A\hat{J}_a^2 + B\hat{J}_b^2 + C\hat{J}_c^2\,, \tag{2.19}$$

Where the coefficients $A, B, C$ defined (in frequency units) as

$$A = \frac{h}{8\pi^2 I_a}\,, \quad B = \frac{h}{8\pi^2 I_b}\,, \quad C = \frac{h}{8\pi^2 I_c}\,, \tag{2.20}$$

are the rotational constants of the molecule under consideration.

**Symmetric molecules**

A symmetric rotor has two equal angular momentum components. For a prolate-type rotor, it holds $I_a < I_b = I_c$ which, in terms of rotational constants, means $A > B = C$. Then, using Equation (2.12), the rotational Hamiltonian, Equation (2.19) can thus be written as

$$\hat{H}_{\mathrm{s,pro}} = B\hat{\mathbf{J}}^2 + (A-B)\hat{J}_a^2\,. \tag{2.21}$$

By standard quantum mechanical treatment [10, 11], it can be shown that, when the rotational Hamiltonian has the form of Equation (2.21), it exists a set of state vectors which are simultaneous eigenfunctions of the square of the total angular momentum $\hat{\mathbf{J}}^2$, of one of its component along the space-fixed reference system (say $\hat{J}_Z$), and of the component referred to the symme-

try axis of the molecule, $\hat{J}_z$. Such state vectors are defined as $|J, K, M\rangle$, where $J$ denotes the principal quantum number, $K$ the quantum number associated to the projection of the total angular momentum along the molecular axis $z$, whereas $M$ is quantum number associated to the projection along the space-fixed axis $Z$. Both $K$ and $M$ quantum numbers can assume $(2J+1)$ values, namely $J, J-1, \ldots -J$; thus, for each rotational level $J$, there are $(2J+1)^2$ sublevels. In absence of applied external fields, however, $(2J+1)$ sublevels with different $M$ are degenerate, according to the fact that all the directions in space are equivalent. The time-independent Schrödinger equation for a rigid symmetric rotor thus takes the form

$$\hat{H}_{\text{s,pro}}|J, K\rangle = E_{J,K}|J, K\rangle \,, \tag{2.22}$$

whose eigenvalues $E_{J,K}$ are

$$E_{J,K} = B\,J(J+1) + (A-B)\,K^2 \,. \tag{2.23}$$

The above expression holds for the prolate rotor; the oblate-type formulation yields

$$E_{J,K} = B\,J(J+1) + (C-B)\,K^2 \,. \tag{2.24}$$

Equation (2.23) and (2.24) show that the rotational energy depends on $K^2$, thus levels with the same $|K|$ (and $K \neq 0$) are doubly degenerate.

**Diatomic and linear molecules**

For a diatomic molecule or, more in general, for any linear molecule, the moment of inertia along the symmetry axis is null, whereas the two perpendicular components are equal to each other: $I_a = 0, I_b = I_c = I$. In the rigid-rotor approximation, the projection of the angular momentum along the ($\infty$-fold) symmetry $a$ axis is identically zero, thus Schrödinger equation simplifies to

$$\hat{H}_{\text{lin}}|J\rangle = B\,J(J+1)|J\rangle \,. \tag{2.25}$$

**Asymmetric molecules**

In the general case, when a molecule lacks a three- (or higher-)fold symmetry axis, the rotational Hamiltonian (Equation (2.18)) cannot be further simplified and the corresponding Schrödinger

equation does not possess a closed analytical solution. A convenient way to obtain the eigenvalues and the eigenfunctions is to apply the variational principle and to adopt the symmetric rotor wavefunctions $|J, K, M\rangle$ as a base to build up a complete representation of the Hamiltonian. The complete subspace for any given $J$ consists of $(2J+1)$ basis functions, each labeled with a different $K$ quantum numbers. This means that the unknown asymmetric rotor eigenfunctions $\phi_{JM}(\theta, \phi, \chi)$ can be expressed in terms of a linear combination of the symmetric rotor basis function $|J, K, M\rangle$ as

$$\Psi_{JM}(\theta, \phi, \chi) = \sum_K a_K |J, K, M\rangle \, . \tag{2.26}$$

On substituting Equation (2.26) into the general Schrödinger equation expression

$$\hat{H}_{\text{asym}} \Phi_{JM}(\theta, \phi, \chi) = E \Phi_{JM}(\theta, \phi, \chi) \, , \tag{2.27}$$

one gets

$$\sum_K a_K \hat{H}_{\text{asym}} |J, K, M\rangle = E \sum_K a_K |J, K, M\rangle \, . \tag{2.28}$$

After multiplying by the bra $\langle J, K', M|$ and integration one easily finds that the energies are the roots of the $(2J+1) \times (2J+1)$ secular determinant

$$|\mathsf{H}_{\text{asym}}(K'K) - E\delta_{K',K}| = 0 \, , \tag{2.29}$$

where $\mathsf{H}_{\text{asym}}(K'K)$ is the $(2J+1) \times (2J+1)$ square Hamiltonian matrix illustrated in Figure 2.1.4. It can be seen that there are no non-zero matrix elements that connect different $J$. As

$$\mathbf{H}_{\text{asym}}(K, K') = \begin{bmatrix} J{=}0 & J{=}1 & & J{=}2 & & \\ \begin{bmatrix} H_{K,K} \end{bmatrix} & & & & & \\ & \begin{bmatrix} H_{K,K} & 0 & H_{K,K+2} \\ 0 & H_{K,K} & 0 \\ H_{K,K-2} & 0 & H_{K,K} \end{bmatrix} & & & & \\ & & & \begin{bmatrix} H_{K,K} & 0 & H_{K,K+2} & 0 & 0 \\ 0 & H_{K,K} & 0 & H_{K,K+2} & 0 \\ H_{K,K-2} & 0 & H_{K,K} & 0 & H_{K,K+2} \\ 0 & H_{K,K-2} & 0 & H_{K,K} & 0 \\ 0 & 0 & H_{K,K-2} & 0 & H_{K,K} \end{bmatrix} & \\ & & & & \ddots \end{bmatrix}$$

Figure 2.1.4: Excerpt of the Hamiltonian matrix for an asymmetric molecule represented using the symmetric rotor basis set.

a consequence, the Hamiltonian matrix is factorized in blocks each of which has $(2J+1) \times (2J+1)$ dimension. Within each block, the relevant matrix elements of the operators present in Equation (2.18) are[2]

$$\langle J,K|\hat{J}_z^2|J,K\rangle = K^2 \,, \tag{2.30}$$

$$\langle J,K|\hat{J}_x^2|J,K\rangle = \langle J,K|\hat{J}_x^2|J,K\rangle = \tfrac{1}{2}\left[J(J+1) - K^2\right] \,, \tag{2.31}$$

$$\begin{aligned}\langle J,K|\hat{J}_x^2|J,K\pm 2\rangle &= \langle J,K|\hat{J}_x^2|J,K\pm 2\rangle = \\ &= \tfrac{1}{4}\left\{\left[J(J+1) - K(K\pm 1)\right]\left[J(J+1) - (K\pm 1)(K\pm 2)\right]\right\}^{1/2} \,.\end{aligned} \tag{2.32}$$

It can be seen that, in the rigid-rotor approximation, the Hamiltonian matrix is in the tridiagonal form as only diagonal ($\Delta K = 0$) and $\Delta K = \pm 2$ matrix elements are non-zero.

The solution of the secular determinant Equation (2.29) can be obtained numerically by diagonalization of the Hamiltonian matrix $\mathsf{H}_{\text{asym}}(K'K)$

$$\mathbf{V}^T \mathsf{H}_{\text{asym}}(K'K)\mathbf{V} = \mathbf{E}(K) \,, \tag{2.33}$$

in which the columns of the square orthonormal matrix $\mathbf{V}$ contains the eigenvectors (i.e. the $a_K$ coefficients of Equation (2.26)), while the vector $\mathbf{E}(K)$ gathers the $2J+1$ energy eigenvalues.

It is useful to visualize an asymmetric molecule as an intermediate case between prolate- and oblate-type symmetric rotors, and the degree of asymmetry can be described by the Ray's parameter $\kappa$, defined as

$$\kappa = \frac{2B - A - C}{A - C} \,. \tag{2.34}$$

Prolate and oblate symmetric molecules have $\kappa = -1$ and $\kappa = 1$, respectively, whereas intermediate values pertain to asymmetric species. Due to the asymmetry, the original degeneracy in $K$ is lifted, and $K$ itself is no longer a good quantum number. On the other hand, the rotational energy levels of an asymmetric molecule can be related to the symmetric prolate and oblate rotor limiting cases, as illustrated in Figure 2.1.5. The plot clearly illustrates the correlation existing between the asymmetry doublets and the corresponding degenerate levels for prolate (referred to the $a$ symmetry axis) and oblate (referred to the $c$ symmetry axis) symmetric rotor. This suggest that the asymmetric rotor energy levels can be labeled using the two "pseudo"

[2] In the following we omit the quantum number $M$ from the state vector notation as the present treatment does not take into consideration the effect of external applied field.

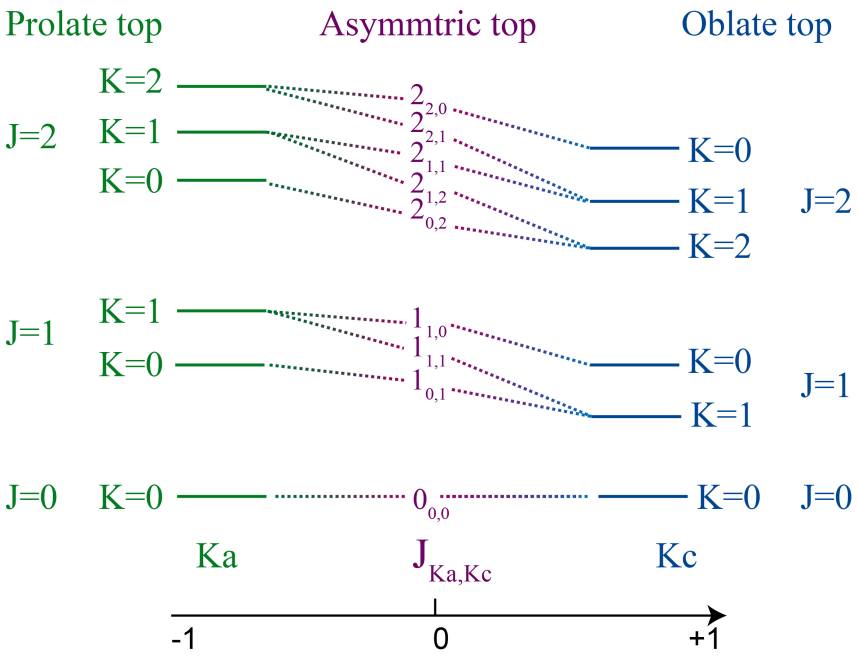


Figure 2.1.5: Relation of the asymmetric rotor energy levels to those of the limiting prolate and oblate symmetric rotor cases.

quantum numbers $K_a, K_c$, which recall the corresponding $K$ to which they correlate to in the two limiting prolate and oblate cases.

### 2.1.4 Vibro-rotational Hamiltonian

When one lifts the rigid rotor approximation, the molecule can distort elastically its structure and thus vibrations shall be considered together with rotation to accurately describe the molecular motion. The derivation of the ro-vibrational Hamiltonian has been obtained in several textbooks and reviews [12, 13] and only the result is reported here:

$$\hat{H} = \frac{1}{2}\sum_{\alpha\beta}(\hat{J}_\alpha - \hat{\Pi}_\alpha)\mu_{\alpha\beta}(\hat{J}_\beta - \hat{\Pi}_\beta) + \frac{1}{2}\sum_{k}^{3N-6}\omega_k\hat{p}_k^2 + V(q_k) - \frac{1}{8}\sum\mu_{\alpha\alpha}\,, \tag{2.35}$$

where $\mu_{\alpha\beta}$ are the components of the inverse inertia tensor, $q_k$ are the dimensionless normal coordinates and $\hat{p}_k$ are their conjugate vibrational momentum operators, defined as,

$$\hat{p}_k = -i\hbar\frac{\partial}{\partial_{q_k}}\,. \tag{2.36}$$

The quantities $q_k$ relates to the normal coordinates[3] $Q_k$ and the corresponding harmonic frequencies $\omega_k$.

$$q_k = \omega_k^{1/2} Q_k \, . \tag{2.37}$$

The operators $\hat{\Pi}_\alpha$ and $\hat{\Pi}_\beta$ are the vibrational angular momentum operator containing the vibration–rotation Coriolis interaction coefficients $\zeta_{kl}^{\alpha}$

$$\hat{\Pi}_\alpha = \sum_{kl} \zeta_{kl}^{\alpha} \left( \frac{\omega_l}{\omega_k} \right)^{1/2} q_k \hat{p}_l \, . \tag{2.38}$$

Here, $\zeta_{kl}^{\alpha}$ represents the elements of the anti-symmetric Coriolis zeta matrix that couples $q_k$ and $q_k$ around the $a-$axis through the rotation [10, 14]. The last term of Equation (2.35) is known as Watson term, which depends on the vibrational coordinates and acts as a mass-contribution correction to the potential. $V(q_k)$ denotes the vibrational potential energy expressed as a Taylor's expansion about the equilibrium position with respect to the dimensionless normal coordinates $q_k$

$$V(q_k) = \frac{1}{2} \sum_k \omega_k q_k^2 + \frac{1}{6} \sum_{k,l,m} f_{k,l,m} q_k q_l q_m + \frac{1}{24} \sum_{k,l,m,n} f_{k,l,m,n} q_k q_l q_m q_n + \dots \, , \tag{2.39}$$

with cubic and quartic force constants expressed as:

$$f_{k,l,m} = \left( \frac{\partial^3 V}{\partial q_k q_l q_m} \right)_e \, , \tag{2.40}$$

$$f_{k,l,m,n} = \left( \frac{\partial^4 V}{\partial q_k q_l q_m q_n} \right)_e \, . \tag{2.41}$$

The final expression of the vibro-rotational Hamiltonian can be summarized in

$$\hat{H} = \sum_{m,n} \hat{H}_{m,n} \, , \tag{2.42}$$

where $m$ expresses the power of the vibrational operators (normal coordinates $q_k$ and linear momentum $\hat{p_k}$), while $n$ indicates the grade of the rotational operators $\hat{J}_\alpha$. This expression enables us to choose the optimal approximation of the ro-vibrational Hamiltonian based on the desired level of precision, and the vibration-rotation term to include in the treatment.

[3]The normal coordinates are expressed as linear combinations of mass-weighted atomic cartesian displacements. The coefficients of this transformation are chosen in such a way that the quadratic expression of the vibrational energy contains no cross terms of the type $Q_k Q_l$, with $k \neq l$. See Ref. [13].

A convenient classification of the various Hamiltonian terms is

$$\begin{aligned} \hat{H}_{\text{vibrot}} = \hat{H}_{2,0} + \hat{H}_{3,0} + \hat{H}_{4,0} + \ldots \quad & \text{vibrational terms} \\ + \hat{H}_{0,2} + \hat{H}_{1,2} + \hat{H}_{2,2} + \ldots \quad & \text{rotational terms} \\ + \hat{H}_{2,1} + \hat{H}_{3,1} + \hat{H}_{4,1} + \ldots \quad & \text{Coriolis terms} \end{aligned} \tag{2.43}$$

The pure vibrational terms are

$$\hat{H}_{2,0} = \frac{1}{2} \sum_k \omega_k (\hat{p}_k^2 + q_k^2) \,, \tag{2.44}$$

$$\hat{H}_{3,0} = \frac{1}{6} \sum_{k,l,m} f_{klm} q_k q_l q_m \,, \tag{2.45}$$

$$\hat{H}_{4,0} = \frac{1}{24} \sum_{k,l,m,n} f_{klmn} q_k q_l q_m q_n + \sum_\alpha B_\alpha \hat{p}_\alpha^2 \,. \tag{2.46}$$

Here $\hat{H}_{2,0}$ is the harmonic oscillator operator while $\hat{H}_{3,0}$ and $\hat{H}_{4,0}$ represents the anharmonicity of the molecular vibration.

The rotational terms include

$$\hat{H}_{0,2} = \sum_\alpha B_\alpha^{(e)} \hat{J}_\alpha^2 \,, \tag{2.47}$$

$$\hat{H}_{1,2} = \sum_{\alpha\beta} \sum_k B_k^{\alpha\beta} q_k \hat{J}_\alpha \hat{J}_\beta \,, \tag{2.48}$$

$$\hat{H}_{2,2} = \frac{3}{8} \sum_{\alpha\beta\gamma} \sum_{k,l} B_\gamma^{-1} (B_k^{\alpha\gamma} B_l^{\gamma\beta} + B_l^{\gamma\alpha} B_k^{\gamma\beta}) q_k q_l \hat{J}_\alpha \hat{J}_\beta \,. \tag{2.49}$$

The term $\hat{H}_{0,2}$ is the Hamiltonian for the rigid rotor approximation, while $\hat{H}_{1,2}$ and $\hat{H}_{2,2}$ are the centrifugal distortion operators. $\hat{H}_{2,1}$, $\hat{H}_{3,1}$ and $\hat{H}_{4,1}$ represent the Coriolis interaction between rotation and vibration.

An exact solution of the Schrödinger equation for the operator $\hat{H}_{\text{vibrot}}$ cannot be found, however for molecules with small vibrational amplitudes, the ro-vibrational energies can be found through perturbation methods. The most efficient way to perform such treatment is the Van Vleck contact transformation. This approach is described in details in Ref. [12] and consists of series of unitary transformations which bring the Hamiltonian (2.43) into an equivalent but simpler form. The most beneficial results of this method is to decouple the vibrational states and to generate a new "effective" Hamiltonian operator whose coefficients are specific for (or

vibrationally averaged in) a given vibrational state.

### 2.1.5 Centrifugal distortion

The contact transformation procedure described in the previous section removes the diagonal contribution of the $\hat{H}_{1,2}$ and introduces a new effective $\hat{H}_{0,4}$ term which depends on the fourth power of the rotational operators only. Such energetic term represents a correction to the rotational energy due to the elastic distortion of the molecular structure produced by the centrifugal forces induced by the end-over-end rotation. Higher-order effects are taken into account by treating several other products of Hamiltonian terms (Equation (2.43)) which are brought onto $\hat{H}_{0,6}$ term, i.e. the energy contribution depending on the sixth power or the rotational operators. The complete "effective" rotational Hamiltonian thus become

$$\begin{aligned}\hat{H}_{rot} =& \hat{H}_{0,2} + \hat{H}_{0,4} + \hat{H}_{0,6} + ... \\ =& \frac{1}{2}\sum_{\alpha} B_{\alpha}^{(e)} \hat{J}_{\alpha}^2 + \frac{1}{4}\sum_{\alpha,\beta,\gamma,\delta} \tau_{\alpha,\beta,\gamma,\delta} \hat{J}_{\alpha}\hat{J}_{\beta}\hat{J}_{\gamma}\hat{J}_{\delta} \\ &+ \sum_{\alpha,\beta,\gamma,\delta,\varepsilon,\eta} \eta_{\alpha,\beta,\gamma,\delta,\varepsilon,\eta} \hat{J}_{\alpha}\hat{J}_{\beta}\hat{J}_{\gamma}\hat{J}_{\delta}\hat{J}_{\varepsilon}\hat{J}_{\eta} + \dots \ ,\end{aligned} \tag{2.50}$$

where $\tau_{\alpha,\beta,\gamma,\delta}$ and $\eta_{\alpha,\beta,\gamma,\delta,\varepsilon,\eta}$ are the fourth- and sixth-order centrifugal distortion coefficients, respectively (greek letters represent the $x, y, z$ cartesian coordinates, cyclically). In the Equation (2.50), there are a total of 81 ($3^4$) terms in the first sum and 729 ($3^6$) terms in the second sum. Algebraic reduction procedures, however, allowed to reduce the numbers of $\tau$ and $\eta$ coefficients to a much smaller figure, namely 5 quartic and 7 sextic quantities [15]. These correspond to the constants which are actually determinable experimentally from the analysis of the rotational spectrum.

Two different reductions exist: the $A$-reduced Hamiltonian with the form

$$\begin{aligned}\hat{H}_{rot}^{A} = &\sum_{\alpha} B_{\alpha}^{A}\hat{J}_{\alpha}^2 - \Delta_J \hat{J}^4 - \Delta_{JK}\hat{J}^2\hat{J}_z^2 - \Delta_K \hat{J}_z^4 - \frac{1}{2}[(\delta_J \hat{J}^2 + \delta_K \hat{J}_z^2), (\hat{J}_+^2 + \hat{J}_-^2)] + \\ &+ \Phi_J(\hat{J}^6) + \Phi_{JK}(\hat{J}^4\hat{J}_z^2) + \Phi_{KJ}(\hat{J}^2\hat{J}_z^4) + \Phi_K(\hat{J}_z^6) \\ &+ \frac{1}{2}[(\phi_J \hat{J}^4 + \phi_{JK}\hat{J}^2\hat{J}_z^2 + \phi_K \hat{J}_z^4), (\hat{J}_+^2 + \hat{J}_-^2)] + ... \ ,\end{aligned} \tag{2.51}$$

while the $S$-reduced Hamiltonian is

$$\begin{aligned}\hat{H}^S_{rot} = &\sum_\alpha B^S_\alpha \hat{J}^2_\alpha - D_J \hat{J}^4 - D_{JK}\hat{J}^2\hat{J}^2_z - D_K \hat{J}^4_z - d_1\hat{J}^2(\hat{J}^2_+ + \hat{J}^2_-) + d_2\hat{J}^2(\hat{J}^4_+ + \hat{J}^4_-) \\ &+ H_J(\hat{J}^6) + H_{JK}(\hat{J}^4\hat{J}^2_z) + H_{KJ}(\hat{J}^2\hat{J}^4_z) + H_K(\hat{J}^6_z) \\ &+ h_1\hat{J}^4(\hat{J}^2_+ + \hat{J}^2_-) + h_2\hat{J}^2(\hat{J}^4_+ + \hat{J}^4_-) + h_3(\hat{J}^6_+ + \hat{J}^6_-) + \dots .\end{aligned} \tag{2.52}$$

The $A$ and $S$ reductions are often used interchangeably. The $A$ reduction has the property of maintaining the tridiagonal structure of the Hamiltonian matrix (i.e. it has only $\Delta K = 0, \pm 2$ non-zero matrix elements), but it fails for accidentally symmetric molecules (e.g. those for which $B \approx C$). The $S$ reduction is more robust and it performs well for practically any asymmetric molecule, at the price of generating a slightly more complex energy matrix ($\Delta K = 0, \pm 2, \pm 4, \pm 6$ matrix elements are non-vanishing).

### 2.1.6 Vibro-rotational interaction

Since a complete separation between rotational and vibrational motions cannot be achieved, the transformed Hamiltonian keeps on containing term of the type $\hat{H}_{m,n}$, where both $m$ and $n$ are different from zero. One of the most important is the $\hat{H}_{2,2}$ term, which expresses the vibrational dependence of the rotational constants, as well as other ro-vibrational effects typical of linear and symmetric molecules. Such "effective" term contains also the contribution from the perturbation products $\hat{H}_{3,0}\hat{H}_{1,2}$, $\hat{H}_{2,1}\hat{H}_{2,1}$, and $\hat{H}_{2,1}\hat{H}_{0,2}$. Collecting all the contributions which depends on $J^2$, a new set of modified rotational constants, specific for each vibrational states, can be defined

$$B^{(\alpha)}_v = B^{(\alpha)}_e - \sum_k \alpha_k \left(v_k + \frac{d_k}{2}\right) , \tag{2.53}$$

where, $B^{(\alpha)}_e$ denotes the equilibrium rotational constant, $B^{(\alpha)}_v$ the "effective" rotational constant for the vibrational state $v$, and $\alpha_k$ the vibration-rotational interaction constant, which depends on the quadratic and cubic potential constants as well as on the Coriolis terms. In general, $\alpha_k$ coefficients can be predicted by ab initio quantum chemical calculations [14], whereas the experimental values can only be derived once the rotational constants of the vibrational ground state and the corresponding vibrational excited state are known.

### 2.1.7 Anharmonic and Coriolis resonance

The contact transformation treatment sketched in the previous sections is essentially a perturbation approach, its validity is thus subject to the conditions that the various vibrational states are widely separated in energy. In case of near degeneracies (i.e. $\omega_k \approx \omega_l$), some of the energy denominators involved in the transformation terms can become singular, thus promoting some second- (or higher-) order contributions to the much larger, first order magnitude. In such cases, the resonant terms are removed from the contact transformation, which become incomplete and leaves the Hamiltonian matrix in a partially factorized form. The ro-vibrational energy are thus obtained by separate variational treatments of these residual blocks in which the $v_k$ and $v_l$ vibrational states are coupled by the relevant $H_{m,n}$ off-diagonal Hamiltonian terms.

The simplest case of anharmonic resonance occurs whenever the frequency $\omega_k + \omega_l$ (or $2\omega_k$) is accidentally close to $\omega_m$ and the cubic force constants $f_{klm}$ or ($f_{kmm}$) — which is part of the $\hat{H}_{3,0}$ Hamiltonian term — is non-zero. This interaction is called "Fermi resonance" and is purely vibrational; its main effect is to increase the energy separation between the two interacting levels.

Coriolis resonance is instead caused by the coupling of the total angular momentum $\hat{J}_\alpha$ and the vibrational angular momentum $\hat{p}_\alpha$. The main term of this interaction included in the first order Hamiltonian is

$$\hat{H}_{2,1} = -2 \sum_\alpha B_\alpha \hat{J}_\alpha \sum_{k,l} \zeta^\alpha_{k,l} (\omega_l/\omega_k)^{1/2} q_k \hat{p}_l \, . \tag{2.54}$$

The Coriolis interaction takes place between the $(v_k, v_l)$ and $(v_k + 1, v_l - 1)$ states if they are nearly degenerate and if the symmetry product of the two vibrational states species contains the rotation species, that is,

$$\Gamma_{v_l} \otimes \Gamma_\alpha \otimes \Gamma_{v_k} \subset A, \tag{2.55}$$

with $\alpha = a, b$ or $c$ and $A$ is the total symmetric representation. The treatment of $\hat{H}_{2,1}$ yields off-diagonal elements between interacting levels that are

$$\langle v_k, v_l | \hat{H}_{2,1} | v_k + 1, v_l - 1 \rangle = \mathrm{i} \xi^\alpha_{v,v'} \hat{J}_\alpha \, , \tag{2.56}$$

where

$$\xi^\alpha_{v,v'} = 2 B_\beta \zeta^\beta_{k,l} [(\omega_l/\omega_k)^{1/2} + (\omega_k/\omega_l)^{1/2}][(v_k + 1) v_l / 4]^{1/2} \, . \tag{2.57}$$

It should be noticed that in the case of strong Coriolis resonance between two vibrational states (close degeneracy), it is necessary to consider a further correction of $k, l$-term to the energy, which can be written as follows:

$$\langle v_k, v_l|\hat{H}_{2,2}|v_k+1, v_l-1\rangle = \eta^{\beta\gamma}_{v,v'}(\hat{J}_\beta\hat{J}_\gamma + \hat{J}_\gamma\hat{J}_\beta)\,. \tag{2.58}$$

Here, $\eta^{\beta\gamma}_{v,v'}$ is the parameter of same order of magnitude as the $\alpha$ vibration-rotation interaction constant.

From $\hat{H}_{2,1}$ and $\hat{H}_{2,2}$, the "effective" Hamiltonian of the Coriolis interaction between normal modes $v_k$ and $v_l$ can be expressed as

$$\begin{aligned}\hat{H}^{k,l}_c = {} & \mathrm{i}(G_\alpha + G^J_\alpha\hat{J}^2 + G^J_\alpha\hat{J}^2 + G^K_\alpha\hat{J}^2_z + G^{JJ}_\alpha\hat{J}^4 + ...)\hat{J}_\alpha \\ & + (F_{\beta\gamma} + F^J_{\beta\gamma}\hat{J}^2 + F^J_{\beta\gamma}\hat{J}^2 + F^K_{\beta\gamma}\hat{J}^2_z + F^{JJ}_{\beta\gamma}\hat{J}^4 + ...)(\hat{J}_\beta\hat{J}_\gamma + \hat{J}_\gamma\hat{J}_\beta)\,,\end{aligned} \tag{2.59}$$

in which the first-order Coriolis coupling constants $G_\alpha$ has the form

$$G_\alpha = B^\alpha\zeta^\alpha_{k,l}(\sqrt{\omega_k/\omega_l} + \sqrt{\omega_l/\omega_k})\,. \tag{2.60}$$

Perturbation formulas for the higher-order corrections (e.g. $F_{\beta\gamma}$ constants) are given in Ref. [16].

### 2.1.8 Hyperfine interactions

Hyperfine effects are the result of magnetic and/or electric interactions of the molecular fields with the nuclear moments. The most important one is the so-called nuclear quadrupole coupling, and arises from the interaction between the molecular electric field gradient at the "quadrupolar" nucleus and the nuclear quadrupole moment, which is present in the nuclei with the nuclear spin $I \geq 1$. For instance, nitrogen-containing molecules usually undergo nuclear quadrupole coupling due to the $^{14}$N nucleus. Therefore, for nuclei with $I \geq 1$, the Hamiltonian $H_Q$ has to be added to the rotational one and can be expressed as

$$\hat{H}_Q = \frac{eQq_J}{2I(2I-1)J(2J-1)}[3(\hat{I}\cdot\hat{J})^2 + \frac{3}{2}(\hat{I}\cdot\hat{J}) - \hat{I}^2\cdot\hat{J}^2]\,. \tag{2.61}$$

Here, $eQ$ is the quadrupole moment of the nucleus, and $q_J$ is rotationally averaged electric field gradient, whose form depends on the molecular type. The nuclear quadrupole-coupling constant $eQq_J$ is usually designated by $\chi$. The hyperfine states are labeled by the quantum number $F$,

which is defined as the vector sum of the rotational momentum **J** with the nuclear spin **I**:

$$\mathbf{F} = \mathbf{J} + \mathbf{I}\,. \tag{2.62}$$

For diatomic and linear molecules it holds

$$q_J = -\frac{qJ}{2J+3}\,, \tag{2.63}$$

and the quadrupole coupling energy can be expressed as

$$E_Q = -\chi Y(J, I, F), \tag{2.64}$$

where $Y(J, I, F)$, the Casimir function, is given by

$$Y(J, I, F) = \frac{\frac{3}{4}C(C+1) - I(I+1)J(J+1)}{2(2J-1)(2J+3)I(2I-1)}\,, \tag{2.65}$$

with $C = F(F+1) - J(J+1) - I(I+1)\ldots$.

The symmetric-top rotor formulation provides a slightly modified definition

$$q_J = q\frac{J}{2J+3}\left[\frac{3K^2}{J(J+1)} - 1\right]\,. \tag{2.66}$$

Consequently, the quadrupole coupling energy for symmetric-top rotor is

$$E_Q = \chi_{zz}\left[\frac{3K^2}{J(J+1)}\right] Y(J, I, F)\,, \tag{2.67}$$

where $z$ is the symmetry axis.

The asymmetric-top rotor case is more complicated since the $q_J$ cannot be expressed in closed form. Following the same approach described for the rotational energies (section 2.1.3), the symmetric rotor eigenbasis can be used to represent the rotation-hyperfine Hamiltonians which contains explicitly the $q_{aa}$, $q_{bb}$, and $q_{cc}$ components of the electric field gradient tensor multiplied by the relevant directions cosines (see section 2.1.2). This produces new diagonal hyperfine terms ($\Delta J = 0$) plus smaller off-diagonal $\Delta J = \pm 1, \pm 2$ connections (the so called "2nd-order contributions"). The hyperfine energies are then obtained by matrix diagonalization as illustrated in section 2.1.3. Regardless of the form of the quadrupole coupling energy, this

interaction leads to a splitting of the rotational energy levels. In addition to the quadrupole interaction discussed in this section, other hyperfine interactions can occur such as spin-rotation and dipolar spin-spin interactions [10].

### 2.1.9 Selection rules for rotational and vibrational transitions

In the framework of quantum mechanics, a radiation-induced transition from an initial state $|i\rangle$ to a final state $|f\rangle$ occurs if at least one of the following matrix elements of the components of electric dipole moment operator along the space fixed axes does not vanish:

$$\langle i|\mu_X|f\rangle\ , \quad \langle i|\mu_Y|f\rangle\ , \quad \langle i|\mu_Z|f\rangle\ . \tag{2.68}$$

When dealing with free, isolated rotating and vibrating molecules, it is customary to express the space-fixed component by means of the corresponding molecule-fixed components $\mu_x, \mu_y, \mu_z$ through the appropriate direction cosines (see section 2.1.2), e.g.,

$$\mu_Z = \sum_\alpha \Phi(\theta,\phi,\chi)_{Z\alpha}\mu_\alpha,\ , \quad \alpha = x,y,z \quad \text{cyclically}\ . \tag{2.69}$$

Then, each $\mu_\alpha$ can be expanded in terms of dimensionless normal coordinates $q_k$ about its equilibrium position

$$\mu_\alpha = \mu_\alpha(e) + \sum_k \left(\frac{\partial\mu_\alpha}{\partial q_k}\right)_e q_k + \frac{1}{2}\sum_{k,l}\left(\frac{\partial^2\mu_\alpha}{\partial q_k \partial q_l}\right)_e q_k q_l + \dots\ , \tag{2.70}$$

In the following calculation, we only retain the first two terms of Equation (2.70). By adopting the harmonic oscillator and rigid rotor approximation, and using the wavefunctions in the usual form $\langle v; J, K| = \langle v| \times \langle J, K|$, where $v$ represent the vibrational quantum number, the matrix elements of Equation (2.68) take the form

$$\sum_\alpha \left[\mu_\alpha(e)\langle v|v'\rangle + \sum_k \left(\frac{\partial\mu_\alpha}{\partial q_k}\right)_e \langle v|q_k|v'\rangle\right] \langle J,K|\Phi(\theta,\phi,\chi)_{Z\alpha}|J',K'\rangle\ . \tag{2.71}$$

Pure rotational transitions in a given vibrational state $|v\rangle$ are determined by the first term in the square brackets, for which it is clear the need for a permanent dipole moment. The second term controls the vibrational transitions. The selection rules can be obtained easily by evaluating the matrix elements $\langle J,K|\Phi(\theta,\phi,\chi)_{Z\alpha}|J',K'\rangle$ and $\langle v|q_k|v'\rangle$.

For vibrational transitions, two conditions are readily seen. First, according to the rule of vanishing integrals, the direct product of the symmetry species of the two vibrational wavefunctions must contain the species of the normal coordinate $q_k$

$$\Gamma_v \otimes \Gamma_{v'} \subset \Gamma_{q_k} \,, \tag{2.72}$$

second, the harmonic oscillator matrix elements are non-vanishing only if $\delta_v = \pm 1$. This latter rule is partially lifted by the anharmonicity, thus weaker transitions with $|\delta_v| > 1$ (vibrational overtones) are also possible.

For rotational transitions, one has to determine the conditions for which the matrix element

$$\langle J, K | \Phi(\theta, \phi, \chi)_{Z\alpha} | J', K' \rangle \,, \tag{2.73}$$

does not vanish. This is straightforward for linear and symmetric molecules ($\mu_z \neq 0$), for which it holds

$$\Delta J = \pm 1 \,, \quad \Delta K = 0 \,. \tag{2.74}$$

For asymmetric molecules the calculation is more complicated as one needs to consider the symmetry properties of the various components of the permanent dipole moment together with those of the $J_{K_a,K_c}$ rotational levels (see section 2.1.3). A detailed treatment is reported in Ref. [10], here we only summarize the results. The relevant invariance group is the $D_2$, also called $V$ group. The three components of the dipole moment, $\mu_a, \mu_b, \mu_c$, transform as $B_a, B_b, B_c$, while the rotational state transform according to the parity of the $K_a, K_c$ pseudo-quantum numbers (e.g. $ee$ is $A$, $eo$ is $B_a$, etc.). The resulting selection rules are:

$$\begin{array}{llll}
\mu_a \neq 0 & A \longleftrightarrow B_a & B_b \longleftrightarrow B_c & \Delta K_a = 0, \pm 2, \ldots \\
 & ee \longleftrightarrow eo & oo \longleftrightarrow oe & \Delta K_c = \pm 1, \pm 3, \ldots \\
\mu_b \neq 0 & A \longleftrightarrow B_b & B_a \longleftrightarrow B_c & \Delta K_a = \pm 1, \pm 3, \ldots \\
 & ee \longleftrightarrow oo & eo \longleftrightarrow oe & \Delta K_c = \pm 1, \pm 3, \ldots \\
\mu_c \neq 0 & A \longleftrightarrow B_c & B_a \longleftrightarrow B_b & \Delta K_a = \pm 1, \pm 3, \ldots \\
 & ee \longleftrightarrow oo & eo \longleftrightarrow oe & \Delta K_c = 0, \pm 2, \ldots
\end{array}$$

When the molecule shows a resolvable hyperfine interaction (see section 2.1.8), selection rules in $F$ should also be considered. Their calculation involves the use of spherical tensor

algebra and is presented in details in Ref. [10]. After a rather lengthy derivation, one finds that

$$\Delta F = 0, \pm 1 \, , \tag{2.75}$$

with the transitions having $\Delta F = \Delta J$ being the most intense. The overall result is that a rotational transition is split in several components. This is the so-called hyperfine structure of the rotational spectrum.

For asymmetric rotors, the notation ${}^{m}M_{x}$ is used to identify the type of rotational and ro-vibrational transitions, where $M = P, Q, R$ denotes the transitions with $\Delta J = -1, 0, +1$, respectively; $m = p, q, r$ indicates the transitions with $\Delta K_a = -1, 0, +1$, respectively; $x$ denotes the $K_a$ value of the initial state. In this notation, only $K_a$ values are given because all molecular systems studied in this thesis are near-prolate asymmetric rotors, for which the $K_a$ value is much more important than $K_c$. For linear and symmetric molecules, a simpler $M_x$ notation is sufficient to indicate the types of transitions.

## 2.2 Measured Active Rotational–vibrational Energy Levels (MARVEL)

The theory presented in the previous sections relies on physical models that describe the rotation-vibration problem and are able to reproduce the experimental findings in most instances. However, in some cases these models are not satisfactory – or the parameterization is inaccurate/incomplete – so that it is not possible to use an effective Hamiltonian for reproducing the observed spectra within the experimental accuracy. For example, due to the slow converge of the standard Watson Hamiltonian, ro-vibrational transitions with high $K_a$ values observed in the spectrum of water cannot be modeled successfully. In a more general example, if the energy levels of a given vibrational excited states are strongly perturbed through anharmonic resonances with nearby unknown states, the lack of available information prevents an accurate modeling of the effect of such interactions.

These difficulties can be overcome by means of the Measured Active Rotational–Vibrational Energy Levels (MARVEL) method, which derives energy levels and the corresponding uncertainties from the inversion of different rotational and ro-vibrational transitions through a weighted least-squares procedure. In the MARVEL analysis, the influence of potential pertur-

bations or the weakness of a given physical model can be ignored. However, the main limitation is given by the fact that the MARVEL algorithm cannot predict transition frequencies involving unknown energy levels.

In the next subsections, the main details about the MARVEL procedure are presented and explained.

### 2.2.1 Methodological details

In this section we present a short summary of the simple weighted least-squares theory behind MARVEL. The MARVEL input file contains a grand list of $N_t$ experimental transitions. In addition to the quantum labeling of each transition, the required information for MARVEL includes the transition frequency ($\sigma_{ij}$) as well as the corresponding uncertainties ($\delta_{ij}$). The relationship between the frequency of an experimental transition and the experimental energy levels ($E_{\mathrm{up}(i)}$ and $E_{\mathrm{low}(j)}$) is

$$\sigma_{ij} = E_{\mathrm{up}(i)} - E_{\mathrm{low}(j)} \, . \tag{2.76}$$

The MARVEL energy levels can be obtained by solving the following matrix equation:

$$\mathbf{aX} = \mathbf{Y} \tag{2.77}$$

where the vector $\mathbf{Y}$ is the transition matrix containing the $N_t$ experimental transitions, the vector $\mathbf{X}$ is the energy level matrix with $N_l - 1$ dimensions, and $\mathbf{a}$ is the input matrix that describes the relation between the transition frequency $\sigma_{ij}$ and the energy levels $E_{\mathrm{up}(i)}$ and $E_{\mathrm{low}(j)}$. In detail, if the energy level is the lower level of the transition $E_{\mathrm{low}(j)}$, the element of the $\mathbf{a}$ matrix is -1; if the energy level is the upper level of the transition $E_{\mathrm{up}(i)}$, the element of $\mathbf{a}$ is equal to +1; otherwise, the element is 0.

The weighted least-squares solution of Equation (2.77) can be derived by solving:

$$\mathbf{AX} = \mathbf{B} \; (\mathbf{A} = \mathbf{a}^T\mathbf{ga}; \mathbf{B} = \mathbf{a}^T\mathbf{gY}), \tag{2.78}$$

where the $g_{ij}$ element of the weighted matrix $\mathbf{g}$ is related to the transition uncertainty $\delta_{ij}$ by

$$g_{ij} = \frac{1}{{\delta_{ij}}^2}. \tag{2.79}$$

Figure 2.2.1 shows the general representation of the MARVEL approach for the inversion of experimental transition information to derive MARVEL energy levels.

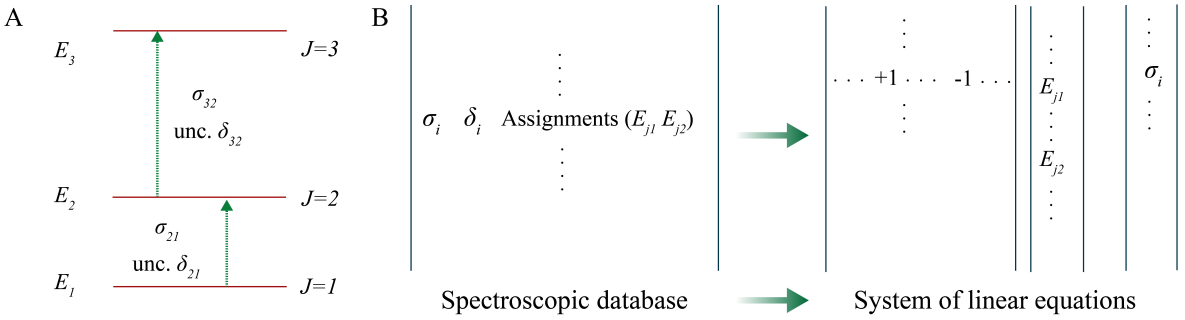


Figure 2.2.1: The left panel (A): A simple case of MARVEL energy level; The right panel (B): Pictorial representation of the MARVEL approach for the inversion of experimental line information to derive energy levels.

A simple example is the case of a MARVEL dataset containing two transitions $J = 2 \leftarrow 1$ and $J = 3 \leftarrow 2$, as shown in Figure 2.2.1. The form of the matrix equation 2.78 is

$$\begin{bmatrix} -1 & 0 \\ +1 & -1 \\ 0 & +1 \end{bmatrix} \times \begin{bmatrix} 1/\delta_{21}^2 & 1/\delta_{32}^2 \end{bmatrix} \times \begin{bmatrix} -1 & +1 & 0 \\ 0 & -1 & +1 \end{bmatrix} \times \begin{bmatrix} E_1 \\ E_2 \\ E_3 \end{bmatrix} = \begin{bmatrix} -1 & 0 \\ +1 & -1 \\ 0 & +1 \end{bmatrix} \times \begin{bmatrix} 1/\delta_{21}^2 & 1/\delta_{32}^2 \end{bmatrix} \times \begin{bmatrix} \sigma_{21} \\ \sigma_{32} \end{bmatrix} \tag{2.80}$$

## 2.2.2 Uncertainties of energy levels

It is crucial that the inversion procedure provides relevant estimates of the uncertainty associated with each energy level. MARVEL algorithm employs both analytical estimation and bootstrap method for evaluating the uncertainty of energy levels. For a given energy level $E_j$, the uncertainty $\varepsilon_j$ can be expressed as

$$\varepsilon_j^1 = t\sigma_j. \tag{2.81}$$

Here $\sigma_j$ is the standard derivation, which is obtained by

$$\sigma_j = \sqrt{(\mathbf{A})_{jj}^{-1}}, \tag{2.82}$$

where $\mathbf{A}^{-1}$ is the inversion matrix. The confidence interval depends on the value of $t$. For example, $\varepsilon_j$ represents the 95% confidence interval for the uncertainty of the energy level when $t = 2$. Unfortunately, Equation 2.81 tends to be overoptimistic in estimating the uncertainty of the energy levels, as it may ignore the fact that some transitions can be somewhat wrong or have unreliably small uncertainty. A slightly more complex expression for evaluating the uncertainty $\varepsilon_j$ is given by:

$$\varepsilon_j^2 = t\sqrt{(\mathbf{A})_{jj}^{-1}\frac{\sum_i g_{ij}\Delta_{ij}^2}{N_t - N_l}}, \tag{2.83}$$

where $\Delta_{ij}$ is

$$\Delta_{ij} = \sigma_{ij} - (E_{\text{up}(i)} - E_{\text{lo}(j)}) \tag{2.84}$$

Equation (2.84) makes MARVEL easy to distinguish effectively either a misassignment or an incorrect line position. In most cases, a misassignment or a faulty line position may be well demonstrated if $\Delta_{ij}$ is substantially larger than the stated uncertainty $\delta_{ij}$.

Generally, analytical methods making use of Equation (2.83) and (2.84) allow to estimate uncertainty. However, there are no reliable analytical expressions that permit to estimate the uncertainty of energy levels if the database contains complex data. In this case, the bootstrap technique, a CPU intensive resampling approach, is a valid method. The bootstrap method is usually employed for determining standard errors and confidence intervals in statistically complicated situations. Two common bootstrap procedures, resampling cases and resampling residuals, are actually used to estimate the uncertainties of the MARVEL energy levels. Resampling cases in the MARVEL algorithm make use of the experimental uncertainties of the transitions, while the resampling residuals method uses the calculated $\Delta_{ij}$ uncertainties. With 400 resamplings in bootstrap procedures, it was found that the $\varepsilon_j^1 = \varepsilon_j^2$ condition could be satisfied after appropriate adjustment of the uncertainty of the transitions, and the uncertainty of the MARVEL energy level is provided to be $\varepsilon_j^1$ or $\varepsilon_j^2$. The adjustment process is described in the next section.

### 2.2.3 Adjustment of line uncertainties

The input data for MARVEL may have considerably different uncertainties for a variety of observed transitions. Numerous problems can be encountered when combining the experimental

transitions from different experiments. For instance, Fourier transform spectra may be affected by pressure shifts, calibration errors, or effects caused by impurities, and the uncertainties associated with automated line center determinations through first and second derivatives. Moreover, in the case of overlapping or very weak lines, the determination of line centers may suffer from large errors. All of these factors can have a huge impact on the energy level uncertainty determination, which mostly relies on the precision of the observed transition frequencies. Consequently, the pre-processing of experimental transitions is a prerequisite for acquiring MARVEL energy levels with as low as possible uncertainties.

The robust re-weighting approach is employed in the MARVEL algorithm to adjust the uncertainties of the transitions database. The adjustment formula can be expressed as follows:

$$g_{ij} = \frac{1}{\delta_{ij}^2 + \alpha\Delta_{ij}^2}, \tag{2.85}$$

where $\alpha$ depends on the fractional number of outlier and the size of their residual. A positive number of $\alpha$ (typically $\leq 1/3$) is suggested for spectroscopic applications. The adjustment by the robust re-weighting technique is quenched when

$$\sum_i \frac{g_{ij}\Delta_{ij}^2}{N_t - N_l} \simeq 1, \tag{2.86}$$

which means that $\varepsilon_j^1 \simeq \varepsilon_j^2$.

With the use of Equation (2.84) to distinguish and clean misassignments in the database and by application of the robust re-weighting algorithm, the MARVEL results should contain correct and self-consistent transitions related with best uncertainties. The MARVEL database will enable us to derive precise MARVEL energy levels with reliable uncertainties.

### 2.2.4 Spectroscopic networks

Quantum mechanics (QM) provides a simple and straightforward way to construct complex spectral networks for a molecule system: the quantized energy levels are the nodes and the allowed transitions between energy levels are links. The QM networks can be characterized experimentally via high-resolution spectroscopy. To be more descriptive, the QM networks are also known as spectroscopic networks (SNs) [17–19]. It is possible to identify which rotational or ro-vibrational energy levels belong to a specific SN based on the quantum mechanical selection rules. Even when a large number of experiments are conducted, however, only a tiny

fraction of the allowed transitions are observable. The advantage of the SNs is that, using the lines list observed in the laboratory, the rotational energy levels associated with the transitions can be obtained. MARVEL can compute the frequencies corresponding to all the allowed transitions based on the MARVEL energy levels. It is important to note that the experiments can be carried out by various spectrometers, which will also lead to nodes of the SNs with different uncertainties. To obtain robust energy levels from MARVEL, the accuracy of the nodes needs to be improved by reducing the uncertainty of the MARVEL energy levels. For example, in general, encompassing centimeter-wave or millimeter-wave measurements would be highly beneficial in improving the overall accuracy of the SNs.

### 2.2.5 Practical Derivation of MARVEL energy levels

The derivation of MARVEL energy levels is based on the following steps:

1. The collection of the available experimental transitions into a spectroscopic database, labeled with vibrational and rotational quantum numbers, transition frequencies, uncertainties, and the reference tag;

2. Construction of the SNs based on the energy levels of the experimental transitions in the database;

3. Cleaning of the transitions with unacceptable error, which may be caused by misassignment or mislabeling;

4. Setting up the matrix equation of Figure 2.2.1 within a given SNs;

5. Solution of the resulting set of linear equations and the inversion matrix. The energy levels with corresponding uncertainties are then determined.

A giant spectroscopic database will generally have multiple transitions associated to a single energy level, which serves as a crossover point for the construction of extensive SNs. Each energy level of the spectroscopic network and the corresponding uncertainty could be derived by means of the MARVEL procedure. In this thesis, the MARVEL energy levels of $H_2CO$ and HDS are investigated and derived. Moreover, MARVEL was used to check the correct assignment of all the analyzed ro-vibrational spectra for other molecules.

# Chapter 3

# Experimental Techniques

Depending on both the type of molecule to be investigated and the frequency range of the rotational/ro-vibrational spectra to be measured, different spectrometers have been used to record the spectra. Mainly, my PhD activities were carried out using the Frequency-Modulation Millimeter-/Submillimeter-wave (FM-mmW) spectrometer located at the Department of Chemistry "Giacomo Ciamician", University of Bologna. In addition, some of the high-resolution IR spectroscopy studies in this thesis made use of the Fourier-Transform Infrared spectrometer (FT-IR) located at the Department of Industrial Chemistry "Toso Montanary", University of Bologna. The experimental setups of the two spectrometers will be described in some detail in this section.

## 3.1 Millimeter/Submillimeter-Wave Spectrometer

The FM-mmW spectrometer in Bologna works in the mm/submm-wave region covering the 75 GHz – 1.2 THz frequency range. The primary source of monochromatic polarized radiation of the spectrometer consists of several Gunn diodes that emit in the frequency range between 75 and 134 GHz with an output power between 30 and 48 mW. Higher frequencies can be obtained by coupling the Gunn diodes to passive frequency multipliers in cascade. In this process, the resulting output power is typically reduced by one order of magnitude for each multiplication step.

The Gunn diode output frequency is stabilized through a Phase-Lock-Loop (PLL) system which works as follows. The radiation of a radio-frequency synthesizer (HP8672A, 2-18 GHz) is sent to a harmonic mixer which mixes it with the millimeter-wave radiation coming from

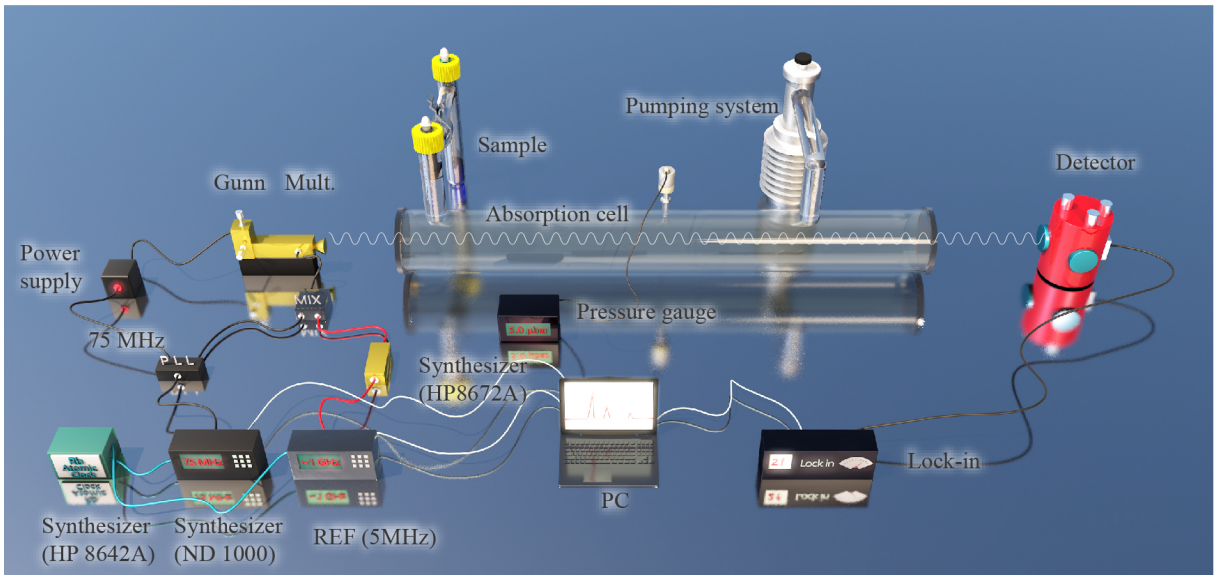


Figure 3.1.1: The FM-mmW spectrometer in Bologna.

the Gunn diode, previously tuned at the approximate desired frequency. The beat signal obtained from the difference between the two radiation frequencies is sent to the PLL, where it is compared to a 75 MHz reference signal (also known as Intermediate Frequency, IF). In our spectrometer, the IF signal is derived by mixing the radiation of two radio-frequency synthesizers, namely the HP8642A (0.1-1000 MHz) and the Schomandl ND1000 (0.01-1000 MHz) synthesizers, in order to exploit the sine-wave modulation of the former (*vide infra*) and the fast frequency switching of the latter. In the synchronization cycle, the beat signal is phase-locked to the reference signal of 75 MHz by adjusting the voltage of the power supply of the Gunn oscillator, thus stabilizing the output frequency of the millimeter-wave source.

The signal-to-noise ratio (S/N) of the recorded spectra is greatly improved by exploiting the frequency-modulation technique. The frequency modulation of the radiation is achieved by modulating the signal of the HP8642A synthesizer with a sine wave at a frequency $f$ between 0.5 and 48 kHz, depending on the desired spectral resolution. The same modulation signal is transferred to the Gunn diode radiation in the PLL. All frequency synthesizers are referenced to a 5 MHz rubidium atomic clock with a precision of a few part over $10^{11}$, thus ensuring the accuracy of the frequency emitted by the Gunn diode as well.

The spectrometer can be equipped with two different absorption cells, depending on the molecular system to be investigated. One of them is a Pyrex tube, with a length of 3.25 m and a diameter of 5 cm. The cell contains two cylindrical hollow electrodes for a DC plasma discharge (up to 5 kV and 120 mA) and it surrounded by a plastic pipe for liquid nitrogen circulation.

A solenoid is also used to produce a magnetic field inside the cell that is longitudinal to the absorption path. The discharge system and magnetic field are primarily employed for producing radicals and ions. Moreover, the cell is connected to a flash vacuum pyrolysis apparatus. The second cell is a 5 cm in diameter, 1.5 m long, quartz tube. The quartz cell is encased in a 90 cm long tubular furnace capable of reaching temperatures as high as 1200 °C. This setup permits the investigation of semi-stable compounds that can be produced during thermal vacuum pyrolysis.

Both cells are connected to a pumping system composed by a diffusion pump and a rotary pump which ensure high vacuum conditions inside the cell. A pressure gauge (0.1 $\mu$bar resolution) MKS Baratron is used to monitor the pressure inside the cells, while several thermocouples allow the measurement of their temperature.

The detection system is consist of a series of zero-bias Schottky-barrier detectors, a preamplifier, a lock-in amplifier, and an analog-to-digital converter board. The lock-in amplifier filters out part of the noise by acting as a resistor-capacitor circuit and demodulates the incoming radiation at twice the modulation frequency ($2f$ detection scheme), thus acquiring the absorption signal in second derivative. The digitized signal is finally sent to a computer.

### 3.1.1 Lamb-dip technique

A double-pass configuration in the FM-mmW spectrometer is used to perform Lamb-dip measurements. In this setup, a roof-top mirror is located at the end of the cell to reflect the radiation back and rotate its polarization by 90 °. A wire-grid polarizer is placed at the other end between the incoming radiation and the cell. The overall result is that the radiation enters the cell passing through the polarizer, whereas the radiation back from the roof-top mirror with its polarization

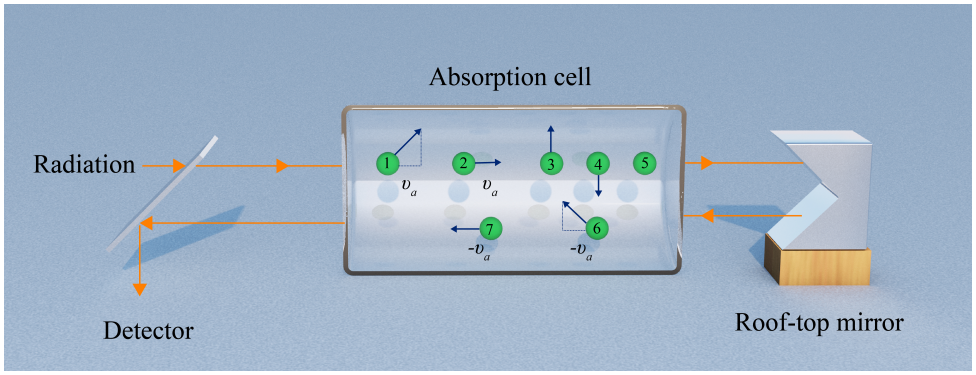


Figure 3.1.2: Graphical representation of double-pass arrangement in the FM-mmW spectrometer. It is also made evident that molecules have different velocity along the direction of the radiation.

rotated by 90° is reflected at right angle onto the detector. A schematic representation of the double-pass configuration is shown in Figure 3.1.2.

The resolution of a rotational spectrometer is mainly limited by two effects: collisions and Doppler effect. Both of them determine a broadening of rotational lines. The pressure broadening, due to collisions, can be reduced by working at a sufficiently low pressure. Instead, overcoming the Doppler requires specific techniques. The one employed in this work is the Lamb-dip technique. Figure 3.1.3 shows the overall result of this technique: the Doppler-broadened line has a narrow dip at its center.

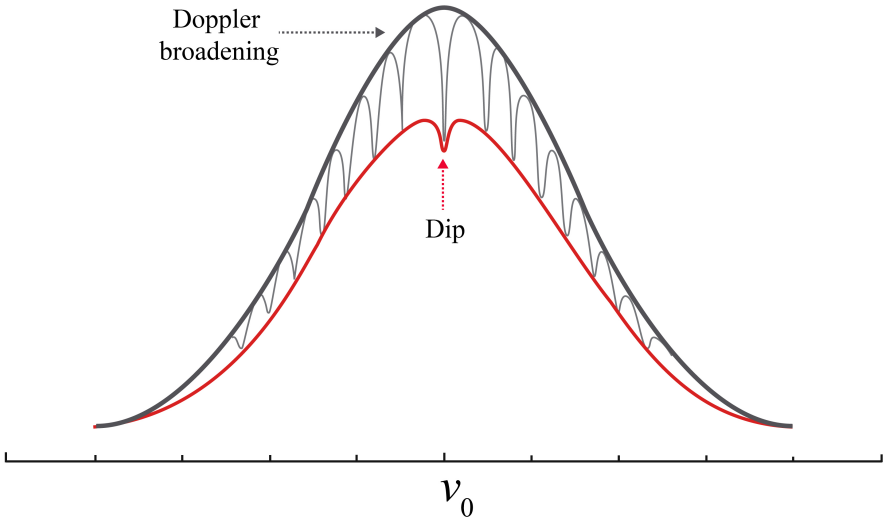


Figure 3.1.3: The black trace is the Doppler line profile. The gray one shows, in a discrete manner, what physically happens at any frequency different from $\nu_0$ as well as the sum of two dips at $\nu_0$. The red trace is the resulting profile and shows the lowering of the line profile and the surviving dip at $\nu_0$.

The frequency at which a given molecule absorbs a radiation depends on the velocity of the molecule with respect to the direction of the radiation. The molecule $a$ absorbs the radiation $\nu_0$ at the frequency $\nu_a$ that depends on its velocity component $v_a$ along the radiation direction:

$$\nu_a = \nu_0 \left(1 \pm \frac{v_a}{c}\right), \tag{3.1}$$

where $c$ is the speed of light. This is so-called Doppler effect. To exploit sub-Doppler resolution, we employed the Lamb-dip technique, which requires three conditions to be fulfilled:

1. measurements should be carried out at very low pressure in order to have the line only broadened by the Doppler effect;

2. measurements should be performed using high power in order to have partial saturation;

3. the radiation should go back and forward inside the cell (double-pass arrangement).

In such conditions, absorptions at frequencies different from $\nu_0$ (i.e. due to $v_a$ different from zero) determine a lowering of the line profile (because of saturation) as shown in Figure 3.1.3. For $v_a = 0$, this effect sums up and the overall result is a narrow dip at the $\nu_0$ frequency. This allows to accurately retrieve the transition frequency or to make a hyperfine structure evident.

## 3.2 Fourier-Transform Infrared Spectrometer

A Bomem DA3.002 FT-IR was employed to acquire ro-vibrational spectra with high resolution in the IR region. A schematic representation of the interferometer optics is shown in Figure 3.2.1.

Three radiation sources can be chosen depending on the working frequency range. For measurements in the FIR region, an Hg lamp is employed. A globar source (silicon carbide bar) is used in the MIR part of the spectrum, while a quartz halogen lamp is employed for near-infrared (NIR) frequencies. The radiation is first focused into an iris (0.5-10 mm) through an ellipsoid mirror and a filter wheel, and then sent to a series of mirrors before passing through a beam splitter composed of $CaF_2$, KBr, or Mylar sheets, which are optimal in the NIR, MIR, and FIR regions, respectively. The radiation is divided in two by the beam splitter. The length of the beam can be adjusted using two mirrors, one of which is fixed while the other is movable; then, the radiation is reflected back toward the beam splitter and recombined.

The spectrometer consists of a Michelson interferometer, which serves as the core of FT-IR. The signal is captured at various positions of the movable mirror to generate the interferogram. The interference pattern that arises is then directed towards the absorption cell. Generally, a White-type multipass cell with path lengths up to 10 m was utilized to contain the sample in its gaseous form. The radiation exiting from the absorption cell is finally focused onto the detector. The radiation is collected using a variety of thermal (bolometers) and photodetector technologies. The case-by-case detector selection is based on the operating frequency yielding the highest sensitivity. Figure 3.2.2 provides a schematic summary of the various setup detectors.

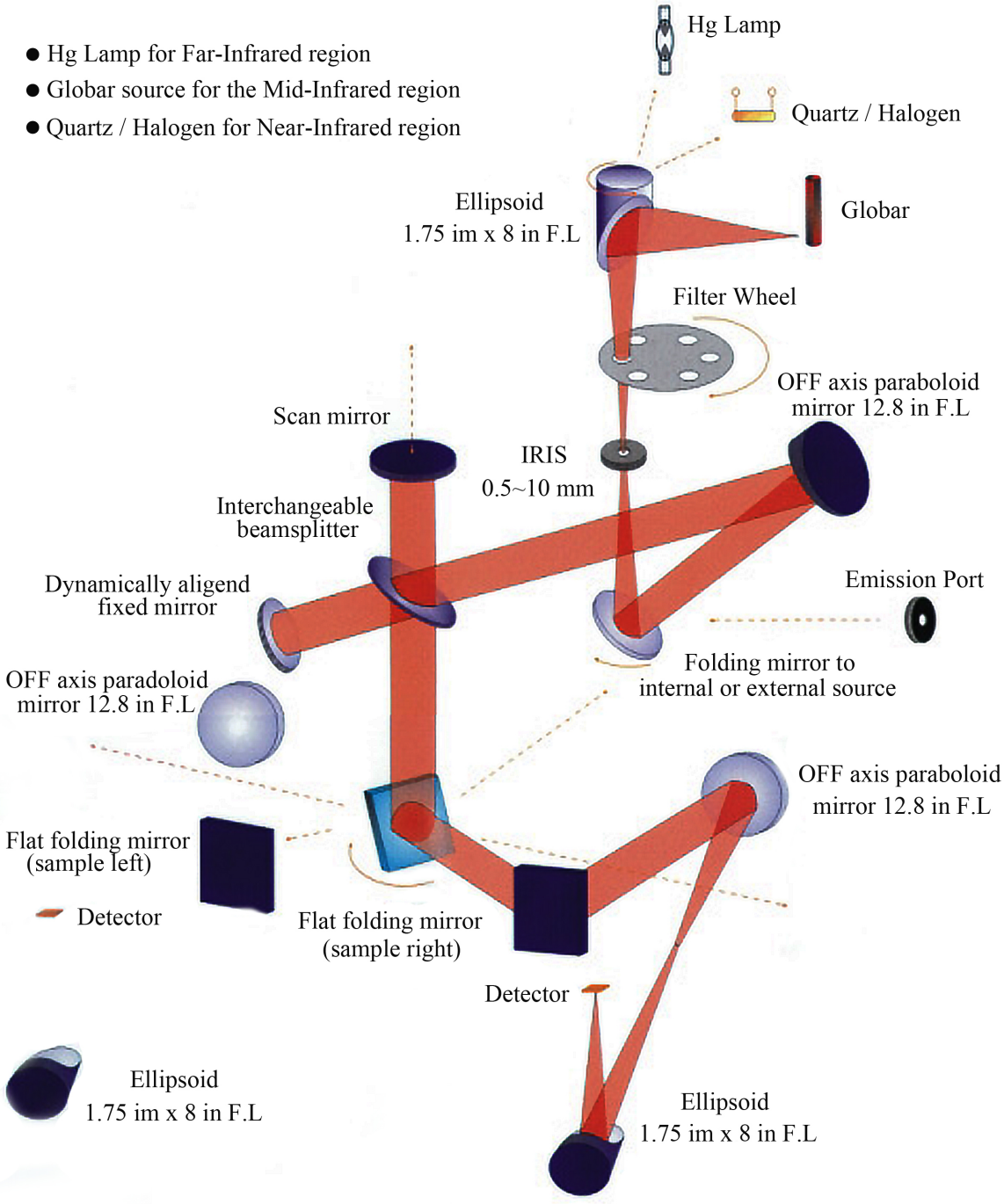


Figure 3.2.1: Scheme of the Bomem DA3.002 FT-IR spectrometer at the Dipartimento di Chimica Industriale "Toso Montanari" as taken from the user manual.

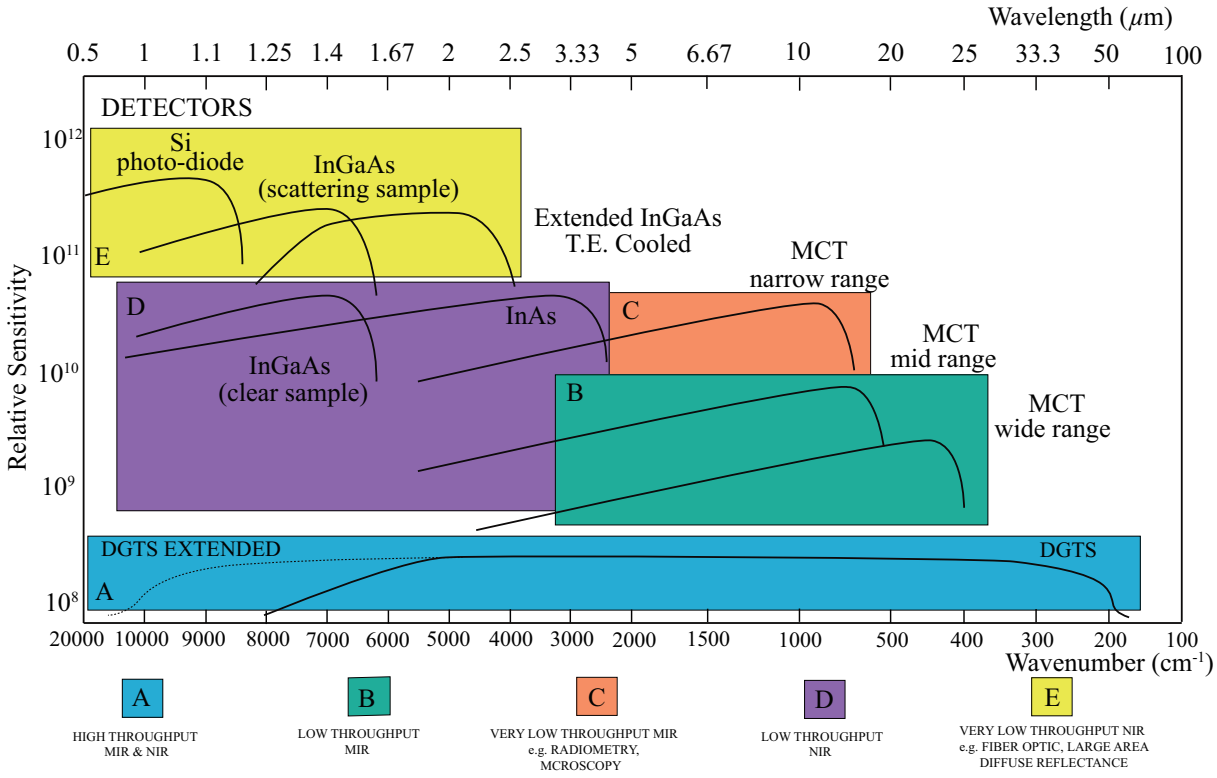


Figure 3.2.2: Possible detectors of the FT-IR spectrometer as illustrated within the user manual.

# Chapter 4

# Case Studies

In this section, the six main projects addressed during the Ph.D. work are presented and discussed. These concerned the following molecules: formaldehyde ($H_2CO$) and deuterated hydrogen sulfide (HDS), which have been investigated using the MARVEL approach; deuterated cyanoacetylene ($DC_3N$) and aminoacetonitrile, whose (ro)-vibrational spectra have been studied; allylimine and 2-aza-1,3-butadiene, whose pure rotational spectra have been recorded and analyzed.

## 4.1 Formaldehyde

### 4.1.1 Introduction

Formaldehyde is a small molecule of great astrochemical relevance. In fact, it has been discovered in a variety of interstellar sources, such as cold molecular clouds [20], star-forming regions [21] and comets [22]. $H_2CO$ maser emission was not only observed towards galaxies, but also in extragalactic sources [23, 24]. The spectral features of $H_2CO$ allowed it to be used as a probe for investigating the kinetic temperature in molecular clouds [24]. $H_2CO$ is also a crucial molecule for the study of planets and protoplanetary disks. Apart from the detection of formaldehyde in the Martian atmosphere [25], its IR absorption features have been observed in protoplanetary disks [26–30].

The importance of line-by-line information on formaldehyde has led to a large number of laboratory studies of its high-resolution rotational and ro-vibrational spectra by means of different spectroscopic techniques [31–51]. From a spectroscopic point of view, $H_2CO$ is a near-prolate asymmetric rotor, with the asymmetry parameter $\kappa$ being -0.9610. Consequently, $H_2CO$

transitions are very well suited to test the convergence of Watson-type Hamiltonians and to compare the performance of the $A-$reduction and $S-$reductions. In view of the large set of high-resolution experimental data available for $H_2CO$, this molecule is also a suitable candidate for determining empirical ro-vibrational energy levels using the MARVEL analysis, whose methodological details are described in Chapter 2 (section 2.2).

In this work, the MARVEL approach has been used to accurately derive the rotational and ro-vibrational energy levels from the experimental data available in the literature. To refine the MARVEL treatment, the FM-mmW spectrometer and the Lamb-dip technique have been employed for recording highly accurate rotational transitions of $H_2CO$ in the ground state and several vibrational excited states. The new measurements have been incorporated into the MARVEL database together with the published data. In total, the MARVEL analysis considered 19831 transitions, with only 16403 that could be verified and actually used. This yielded 5029 ro-vibrational energy levels of $H_2CO$ with well-defined uncertainties. The ro-vibrational energy levels have then been employed to improve the ExoMol line list for $H_2CO$.

**Nuclear spin statistics**

$H_2CO$ has two equivalent hydrogens (nuclear spin of $I = 1/2$), and thus it exists in two nuclear spin isomers: *ortho* and *para*. To build the symmetry combinations of the rotational and nuclear wavefunctions, one has to consider the effect of exchanging two hydrogens on the total wavefunction ($\Psi_{total}$), which can be expressed as

$$\Psi_{total} = \Psi_v \Psi_r \Psi_{ns} \Psi_{el}. \tag{4.1}$$

where $\Psi_v$, $\Psi_r$, $\Psi_{ns}$, and $\Psi_{el}$ denote the vibrational, rotational, nuclear spin, and electronic wavefunction, respectively. The overall wavefunction of $H_2CO$ should be antisymmetric with respect to the exchange of the two hydrogen atoms because they are femions. In the present case, since we consider the electronic ground state, the electronic wavefunction is symmetric. The product of the other three wavefunctions must thus be antisymmetric. In vibrational ground excited state, the vibrational wavefunction $\Psi_v$ is symmetric, thus the product of rotational and nuclear spin wavefunction must be antisymmetric: symmetric rotational wavefunctions combine with antisymmetric $\Psi_{ns}$, antisymmetric rotational wavefunctions combine with symmetric $\Psi_{ns}$. Consequently, the $ortho$-$H_2CO$ rotational energy levels have $K_a$ odd, whereas the $para$-

$H_2CO$ ones have $K_a$ even. In the contrast, if the vibrational wavefunction $\Psi_v$ is antisymmetric, the $ortho$-$H_2CO$ rotational energy levels have $K_a$ even, while $para$-$H_2CO$ ones have $K_a$ odd.

### Vibrational modes

$H_2CO$ belongs to the $C_{2v}$ point group symmetry and has six ($3N-6$, with $N$=number of atoms) vibrational modes. Figure 4.1.1 shows a pictorial representation of the normal modes of $H_2CO$. The $\nu_1$ (symmetric CH stretch), $\nu_2$ (C=O stretch), and $\nu_3$ (HCH angle deformation) fundamentals of formaldehyde transform according to the fully symmetric irreducible representation (irrep $A_1$) of the $C_{2v}$ point group, while the $\nu_4$ fundamental (out-of-plane bending) has $B_1$ symmetry and $\nu_5$ (asymmetric CH stretch) and $\nu_6$ (OCH angle deformation) transform according to the $B_2$ irreducible representation.

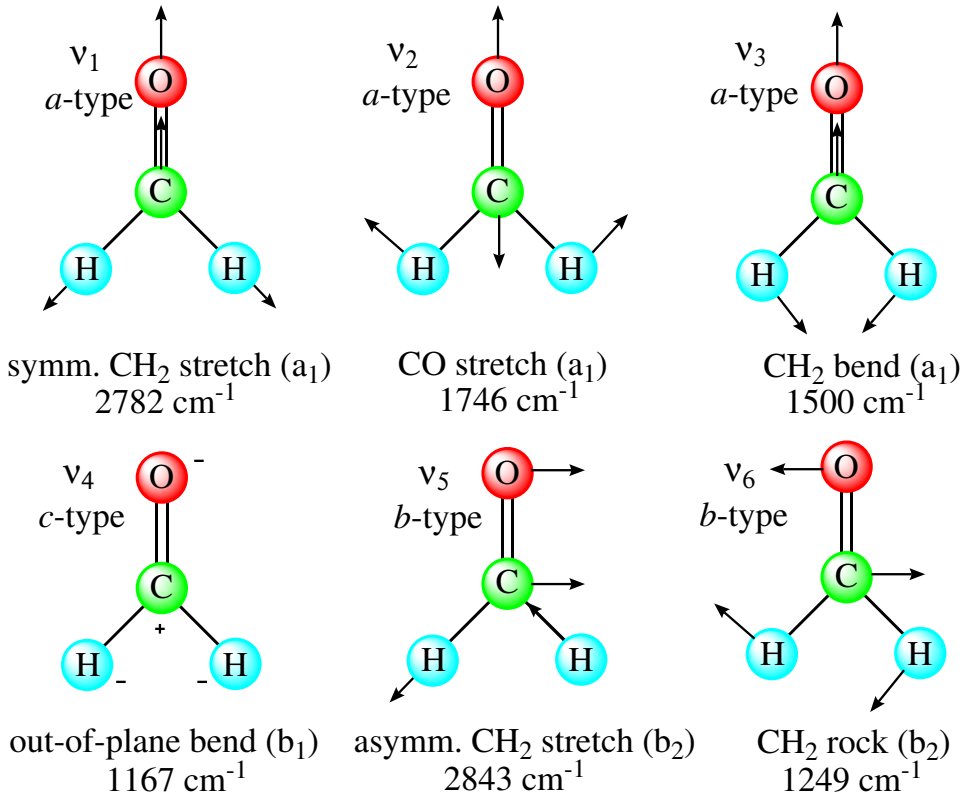


Figure 4.1.1: Vibrational modes of $H_2CO$, together with their symmetry species and the fundamental frequencies indicated. The arrows representing atomic motions during the normal-mode vibrations are not proportional to the actual displacements.

The vibration-rotation motion of $H_2CO$ can be represented by a set of quantum numbers: six vibrational normal modes leading to the notation $(\nu_1, \nu_2, \nu_3, \nu_4, \nu_5, \nu_6)$ and the $(J, K_a, K_c)$ notation for the rotational energy levels. Consequently, the ro–vibrational energy levels of

$H_2CO$ are denoted by a set of nine quantum numbers: $(\nu_1, \nu_2, \nu_3, \nu_4, \nu_5, \nu_6, J, K_a, K_c)$. Quantum numbers and selection rules have been introduced in Chapter 2.

### 4.1.2 The rovibrational database

All published spectral data retrieved from the literature are collected in Tables 4.1.1 and 4.1.2, for a total of 19831 transitions (obtained from 43 different literature sources), 16596 of which are non-redundant. Table 4.1.1 incorporates information employed in the MARVEL analysis, while Table 4.1.2 reports the data that have been discarded. Several old sources [52–54] were excluded from this study because their measurements have been superseded by more accurate investigations.

Table 4.1.1: Data source segments and their characteristics for the $H_2CO$ molecule[a]

| Segment tag | Range | $A/N/V$ | ESU | MSU | LSU | Recalib. Factor |
|---|---|---|---|---|---|---|
| 72TuToTh [55] | 0.483 28–0.483 28 | 1/1/1 | 2.67e-09 | 2.67e-09 | 2.67e-09 | |
| 71TuToTh [56] | 0.141 30–0.165 74 | 3/3/3 | 3.67e-09 | 3.67e-09 | 5.34e-09 | |
| 81ChMi [57] | 0.002 373–0.064 793 | 14/9/9 | 6.67e-09 | 1.00e-08 | 3.34e-08 | |
| 73ChGu [58] | 0.000 003–0.966 50 | 23/21/21 | 1.00e-08 | 1.00e-08 | 3.66e-07 | |
| 73ChGu_S2 [58] | 2.415 3–2.415 3 | 1/1/1 | 3.34e-05 | 3.34e-05 | 3.34e-05 | |
| 68Takami [59] | 0.000 022–0.001 829 | 12/10/10 | 1.67e-08 | 3.15e-08 | 6.44e-07 | |
| 77ChGu [60] | 0.000 005–0.002 305 | 39/39/35 | 3.34e-08 | 3.34e-08 | 1.33e-07 | |
| 96BoDePoLi [61] | 0.000 003–0.708 93 | 68/35/35 | 3.34e-08 | 1.67e-07 | 1.67e-07 | |
| 96BoDePoLi_S2 [61] | 0.000 059–46.275 | 93/45/44 | 1.00e-06 | 1.00e-06 | 4.37e-06 | |
| 96BoDePoLi_S3 [61] | 0.165 27–63.241 | 91/72/72 | 3.34e-06 | 3.34e-06 | 1.67e-05 | |
| 96BoDePoLi_S4 [61] | 34.009–84.711 | 21/21/21 | 1.67e-04 | 1.67e-04 | 1.67e-04 | |
| 21AlTeYuMe | 9.390 7–10.035 | 7/7/7 | 7.00e-08 | 7.00e-08 | 1.33e-07 | |
| 21AlTeYuMe_S2 | 8.237 6–12.988 | 82/82/82 | 7.00e-07 | 7.00e-07 | 4.74e-06 | |
| 66TaEvSh [62] | 0.000 153–0.000 610 | 2/2/2 | 1.00e-07 | 1.00e-07 | 1.33e-07 | |
| 77FaKrMu [63] | 0.002 373–0.082 838 | 4/4/4 | 1.67e-07 | 1.67e-07 | 1.67e-07 | |
| 63Esterowi [64] | 0.010 044–0.035 553 | 4/4/4 | 2.50e-07 | 4.17e-06 | 1.11e-05 | |
| 80CoWi [65] | 0.000 003–15.039 | 127/95/94 | 3.34e-07 | 3.34e-07 | 3.15e-06 | |
| 17MuLe [50] | 45.744–49.915 | 45/45/45 | 3.34e-07 | 3.34e-07 | 3.34e-07 | |
| 88NaReDaJo [32] | 0.000 020–0.561 82 | 10/10/10 | 6.67e-07 | 6.67e-07 | 1.12e-05 | |
| 88NaReDaJo_S2 [32] | 0.000 005–10.029 | 64/64/63 | 1.00e-06 | 1.00e-06 | 1.72e-05 | |
| 88NaReDaJo_S3 [32] | 608.85–630.67 | 2/2/2 | 5.00e-05 | 1.00e-05 | 1.00e-05 | |
| 88NaReDaJo_S4 [32] | 922.63–1 578.4 | 314 9/312 8/312 8 | 2.00e-04 | 1.19e-04 | 2.01e-02 | |
| 88NaReDaJo_S5 [32] | 681.57–1 201.9 | 9/9/9 | 5.00e-03 | 1.00e-03 | 1.00e-03 | |
| 03ThCaRiMu [31] | 0.163 02–0.164 96 | 3/3/2 | 8.34e-07 | 8.34e-07 | 1.00e-06 | |
| 03BrMuLeWi [35] | 27.793–66.778 | 136/136/136 | 1.00e-06 | 1.00e-06 | 2.74e-05 | |
| 09MaPeJaBa [44] | 5.016 8–30.115 | 172/172/171 | 1.00e-06 | 1.00e-06 | 1.33e-05 | |
| 12ElCuGuHi [48] | 23.353–58.596 | 87/87/87 | 1.00e-06 | 1.00e-06 | 5.55e-06 | |

*Continued on next page*

Table 4.1.1 – *Continued from previous page*

| Segment tag | Range | $A/N/V$ | ESU | MSU | LSU | Recalib. Factor |
|---|---|---|---|---|---|---|
| 21virt | 0.000 000–0.000 000 | 446/446/446 | 1.00e-06 | 1.00e-06 | 1.00e-06 | |
| 21virt_S2 | 0.000 001–0.000 009 | 178/177/177 | 1.00e-05 | 1.00e-05 | 2.21e-04 | |
| 21virt_S3 | 0.000 010–0.000 098 | 157/151/151 | 1.00e-04 | 1.00e-04 | 2.78e-03 | |
| 21virt_S4 | 0.000 100–0.000 999 | 168/166/166 | 1.00e-03 | 1.00e-03 | 3.89e-03 | |
| 72Nerf [66] | 1.610 6–10.035 | 15/15/15 | 1.47e-06 | 1.60e-06 | 7.86e-06 | |
| 51LaSt [67] | 0.245 59–2.429 6 | 18/18/18 | 1.67e-06 | 2.40e-06 | 2.03e-05 | |
| 56Erlandss [68] | 2.429 6–7.528 5 | 9/8/8 | 1.67e-06 | 1.60e-05 | 2.79e-05 | |
| 64OkTaMo [69] | 0.000 153–2.437 1 | 70/49/44 | 1.67e-06 | 1.80e-06 | 2.66e-05 | |
| 97CaHaDe [70] | 10.539–10.539 | 1/1/1 | 2.30e-06 | 2.30e-06 | 2.30e-06 | |
| 72JoLoKi [71] | 0.000 153–4.504 1 | 37/10/10 | 3.34e-06 | 8.34e-07 | 5.00e-06 | |
| 78DaWiBe [72] | 0.353 87–12.187 | 86/82/82 | 6.67e-06 | 6.67e-06 | 2.31e-05 | |
| 73ChFrJoOk [73] | 0.553 19–1.979 8 | 7/7/7 | 1.67e-05 | 1.67e-05 | 2.67e-05 | |
| 85TiChKuHu [74] | 4 211.6–5 224.0 | 100 5/100 5/100 3 | 1.00e-04 | 1.10e-04 | 1.16e-02 | |
| 82BrJoMcWo [75] | 1 693.1–1 793.4 | 248/248/248 | 4.00e-04 | 1.59e-04 | 8.99e-04 | |
| 79BrHuPi [76] | 2 700.0–3 000.2 | 319 3/318 9/318 3 | 5.00e-04 | 3.27e-04 | 4.52e-02 | |
| 81SwSa [77] | 1 707.1–1 746.9 | 76/76/76 | 5.00e-04 | 6.50e-04 | 3.38e-03 | |
| 88ClVa [78] | 2 867.2–2 880.4 | 24/22/22 | 5.00e-04 | 3.48e-04 | 7.23e-03 | |
| 94ItNaTa [79] | 2 276.2–2 553.6 | 320/320/317 | 5.00e-04 | 3.91e-04 | 5.56e-03 | |
| 10JaLaTcGa [47] | 1 675.0–3 089.8 | 782/781/781 | 5.00e-04 | 1.62e-04 | 6.45e-03 | 1.000 001 293 |
| 07TcPeLa_S2 [41] | 0.000 006–10.029 | 84/84/84 | 2.10e-04 | 1.00e-04 | 2.25e-03 | |
| 07TcPeLa [41] | 927.68–1 821.6 | 402 4/110 1/110 1 | 8.00e-04 | 1.04e-04 | 5.00e-03 | |
| 06PeBrUtHa [40] | 2 756.6–2 864.6 | 147/143/143 | 1.00e-03 | 1.00e-03 | 3.82e-02 | |
| 09CiMaCi [46] | 4 350.9–4 360.6 | 49/46/36 | 1.00e-03 | 1.00e-03 | 7.97e-03 | |
| 07SaBaHaRi [43] | 5 597.8–5 698.3 | 424/422/418 | 1.50e-03 | 1.00e-03 | 9.08e-03 | |
| 17TaAdNg [51] | 3 398.7–3 529.7 | 786/786/785 | 1.60e-03 | 1.11e-03 | 3.66e-02 | |
| 73Toth [80] | 3 428.2–3 507.4 | 299/299/298 | 3.00e-03 | 2.83e-03 | 4.23e-02 | |
| 77AlJoMc [81] | 945.23–1 540.0 | 991/922/904 | 5.00e-03 | 3.94e-03 | 4.57e-02 | |
| 77AlJoMcb [82] | 1 483.0–1 518.1 | 70/70/70 | 5.00e-03 | 4.14e-03 | 3.57e-02 | |
| 76NaYaKu [83] | 2 643.9–3 011.8 | 184 8/184 5/171 1 | 3.00e-02 | 1.68e-02 | 9.89e-02 | |

[a] Tags denote segments used in this study. The column 'Range' indicates the range (in $cm^{-1}$) corresponding to validated wavenumbers within the transition list. $A$ is the number of assigned transitions, $N$ is the number of non-redundant lines (with distinct wavenumbers or labels), and $V$ is the number of validated transitions obtained at the end of the xMARVEL analysis. In the heading of this table, ESU, MSU, and LSU denote the estimated, the median, and the largest segment uncertainties, respectively, in $cm^{-1}$. Rows are arranged in the order of the ESUs with the restriction that the segments of the same data source should be listed consecutively.

Some comments on the data of Table 4.1.1 are warranted:

- We employed the xMARVEL facility to calibrate the wavenumbers of the transitions reported in Ref. [47] because the authors claim that their line positions were not calibrated.
- 78DaWiBe [72] reassigned the high-resolution measurements of pure rotational transitions in vibrationally excited states from 64OkTaMo [69]. We have implemented the assignments of 78DaWiBe and confirmed their validity.

- 76NaYaKu [83] contains several lines which are not available in any other publications. A total of 134 lines from this work could not be validated because of their relatively low-resolution and thus they were removed from our analysis.

- 88NaReDaJo [32] provides only the line frequencies resulting from their analysis and the corresponding residuals. Therefore, the observed frequencies had to be derived from these data. Similarly, the line transitions in 79BrHuPi [76] were reconstructed by extensive comparison with the HITRAN database [84].

- 02BaCoHaPe [34] measured the $5\nu_2$ overtone band of $H_2CO$, which was analyzed by 07SaBaHaRi [43].

- 72JoLoKi [71] presented a large collection of early microwave experiments on $H_2CO$. Additionally, this source includes several hyperfine-resolved transitions. Hyperfine structure data could be obtained from 59TaShSh [85], 70TuThTo [86], 71TuToTh [56], 72TuToTh [55], and 17MuLe [50]. We entirely neglected hyperfine effects in our study and instead employed central, hyperfine-unresolved line positions where appropriate.

Table 4.1.2: High-resolution spectroscopic studies on $H_2CO$ which were considered but not employed in the present MARVEL analysis.

| Tag | Range / $cm^{-1}$ | Reason for exclusion |
|---|---|---|
| 17FjHeBaLe [87] | 6230 – 6240 | 700 K emission spectrum, line parameters not provided |
| 15RuHeHeFi [49] | 6547 – 7051 | No line assignments |
| 09PeJaTcLa [45] | 1600 – 3200 | Calculated line positions only |
| 07ZhGaDeHu [42] | 6351 – 6362 | No line assignments |
| 06FlLaSaSh [38] | 3096 – 5263 | Data not made available by the authors |
| 06PeVaDa [39] | 2600 – 3100 | No line parameters provided, data not made available by the authors |
| 05StGaVeRu [37] | 6547 – 6804 | No line assignments |
| 03PeKeFl [36] | 1000 – 2000 | Data not made available by the authors |
| 02BaCoHaPe [34] | 5600 – 5700 | Data analyzed by 07SaBaHaRi [43] |
| 96BoHaGrSt [33] | – | Dispersed fluorescence, vibrational state data only |
| 96LuCoFrCr [88] | 7800 – 15200 | No line parameters provided |
| 89ReNaDaJo [89] | 890 – 1590 | No line parameters provided |
| 87NaDaRe [90] | 1148 – 1193 | Lines included in 88NaReDaJo [32] |
| 78Pine [91] | 2700 – 3000 | No line parameters provided |
| 75Nerf [92] | 1 – 10 | Lines included in 72Nerf [66] |
| 73JoMc [93] | 1707 – 1767 | No line parameters provided |
| 70TuThTo [86] | 0.15 – 0.15 | Lines included in 71TuToTh [56] |
| 60OkHiSh [94] | 0.98 | Lines included in 64OkTaMo [69] |

### 4.1.3 New rotational measurements

To refine the MARVEL treatment, we recorded 89 pure rotational transitions of $H_2CO$ in the ground state and several vibrationally excited states. While the instrumental setup of the spec-

trometer and all related information are detailed in Chapter 3, here we mention that $H_2CO$ in the gas phase was obtained from the vapors of poly-formaldehyde at room temperature.

Table 4.1.3: Rotational transitions of $H_2CO$ measured in this study at Doppler-limited resolution (accuracy: 20 kHz, $6.67 \times 10^{-7}$ cm$^{-1}$).[a]

| $\sigma_{\rm new}$/cm$^{-1}$ | Line assignment | $\sigma_{\rm new}$/cm$^{-1}$ | Line assignment | $\sigma_{\rm new}$/cm$^{-1}$ | Line assignment |
|---|---|---|---|---|---|
| 9.396 103 294 | $\nu_3, 4_{1,4} \leftarrow 3_{1,3}$ | 12.098 165 470 | $\nu_4, 5_{3,3} \leftarrow 4_{3,2}$ | 9.694 153 398 | $\nu_0, 4_{0,4} \leftarrow 3_{0,3}$ |
| 9.720 532 400 | $\nu_3, 4_{0,4} \leftarrow 3_{0,3}$ | 12.098 598 600 | $\nu_4, 5_{3,2} \leftarrow 4_{3,1}$ | 9.714 646 044 | $\nu_0, 4_{2,3} \leftarrow 3_{2,2}$ |
| 9.745 845 447 | $\nu_3, 4_{2,3} \leftarrow 3_{2,2}$ | 12.129 667 850 | $\nu_4, 5_{2,3} \leftarrow 4_{2,2}$ | 9.719 405 501 | $\nu_0, 4_{3,2} \leftarrow 3_{3,1}$ |
| 9.753 700 377 | $\nu_3, 4_{3,2} \leftarrow 3_{3,1}$ | 12.432 459 250 | $\nu_4, 5_{1,4} \leftarrow 4_{1,3}$ | 9.719 535 726 | $\nu_0, 4_{3,1} \leftarrow 3_{3,0}$ |
| 9.753 859 167 | $\nu_3, 4_{3,1} \leftarrow 3_{3,0}$ | 9.366 709 450 | $\nu_6, 4_{1,4} \leftarrow 3_{1,3}$ | 9.738 339 087 | $\nu_0, 4_{2,2} \leftarrow 3_{2,1}$ |
| 9.773 007 973 | $\nu_3, 4_{2,2} \leftarrow 3_{2,1}$ | 9.682 101 847 | $\nu_6, 4_{0,4} \leftarrow 3_{0,3}$ | 9.834 452 846 | $\nu_0, 22_{2,20} \leftarrow 23_{0,23}$ |
| 10.088 575 460 | $\nu_3, 4_{1,3} \leftarrow 3_{1,2}$ | 9.697 356 479 | $\nu_6, 4_{2,3} \leftarrow 3_{2,2}$ | 10.034 829 710 | $\nu_0, 4_{1,3} \leftarrow 3_{1,2}$ |
| 11.739 822 940 | $\nu_3, 5_{1,5} \leftarrow 4_{1,4}$ | 9.696 151 729 | $\nu_6, 4_{3,2} \leftarrow 3_{3,1}$ | 10.248 367 590 | $\nu_0, 9_{2,7} \leftarrow 10_{0,10}$ |
| 12.129 667 850 | $\nu_3, 5_{0,5} \leftarrow 4_{0,4}$ | 9.696 255 862 | $\nu_6, 4_{3,1} \leftarrow 3_{3,0}$ | 10.364 365 470 | $\nu_0, 18_{3,15} \leftarrow 19_{1,18}$ |
| 12.178 445 400 | $\nu_3, 5_{2,4} \leftarrow 4_{2,3}$ | 9.718 870 594 | $\nu_6, 4_{2,2} \leftarrow 3_{2,1}$ | 10.448 342 040 | $\nu_0, 37_{4,33} \leftarrow 37_{4,34}$ |
| 12.192 149 190 | $\nu_3, 5_{4,2} \leftarrow 4_{4,1}$ | 10.029 447 240 | $\nu_6, 4_{1,3} \leftarrow 3_{1,2}$ | 10.555 863 330 | $\nu_0, 11_{1,10} \leftarrow 11_{1,11}$ |
| 12.192 149 190 | $\nu_3, 5_{4,1} \leftarrow 4_{4,0}$ | 11.704 713 210 | $\nu_6, 5_{1,5} \leftarrow 4_{1,4}$ | 10.896 074 830 | $\nu_0, 19_{2,17} \leftarrow 19_{2,18}$ |
| 12.194 013 170 | $\nu_3, 5_{3,3} \leftarrow 4_{3,2}$ | 12.086 508 690 | $\nu_6, 5_{0,5} \leftarrow 4_{0,4}$ | 11.212 427 070 | $\nu_0, 28_{3,25} \leftarrow 28_{3,26}$ |
| 12.194 571 510 | $\nu_3, 5_{3,2} \leftarrow 4_{3,1}$ | 12.120 488 600 | $\nu_6, 5_{2,4} \leftarrow 4_{2,3}$ | 11.733 738 380 | $\nu_0, 5_{1,5} \leftarrow 4_{1,4}$ |
| 12.232 626 840 | $\nu_3, 5_{2,3} \leftarrow 4_{2,2}$ | 12.109 817 660 | $\nu_6, 5_{4,2} \leftarrow 4_{4,1}$ | 12.073 937 490 | $\nu_0, 8_{2,6} \leftarrow 9_{0,9}$ |
| 12.604 848 190 | $\nu_3, 5_{1,4} \leftarrow 4_{1,3}$ | 12.109 817 660 | $\nu_6, 5_{4,1} \leftarrow 4_{4,0}$ | 12.099 570 770 | $\nu_0, 5_{0,5} \leftarrow 4_{0,4}$ |
| 9.384 944 381 | $\nu_4, 4_{1,4} \leftarrow 3_{1,3}$ | 12.121 054 530 | $\nu_6, 5_{3,3} \leftarrow 4_{3,2}$ | 12.139 927 050 | $\nu_0, 5_{2,4} \leftarrow 4_{2,3}$ |
| 9.649 643 518 | $\nu_4, 4_{0,4} \leftarrow 3_{0,3}$ | 12.121 422 250 | $\nu_6, 5_{3,2} \leftarrow 4_{3,1}$ | 12.145 176 040 | $\nu_0, 5_{4,2} \leftarrow 4_{4,1}$ |
| 9.670 558 195 | $\nu_4, 4_{2,3} \leftarrow 3_{2,2}$ | 12.163 422 430 | $\nu_6, 5_{2,3} \leftarrow 4_{2,2}$ | 12.145 176 040 | $\nu_0, 5_{4,1} \leftarrow 4_{4,0}$ |
| 9.677 770 970 | $\nu_4, 4_{3,2} \leftarrow 3_{3,1}$ | 12.532 770 930 | $\nu_6, 5_{1,4} \leftarrow 4_{1,3}$ | 12.150 912 170 | $\nu_0, 5_{3,3} \leftarrow 4_{3,2}$ |
| 9.677 893 765 | $\nu_4, 4_{3,1} \leftarrow 3_{3,0}$ | 8.237 600 872 | $\nu_0, 21_{2,19} \leftarrow 22_{0,22}$ | 12.151 369 510 | $\nu_0, 5_{3,2} \leftarrow 4_{3,1}$ |
| 9.693 290 175 | $\nu_4, 4_{2,2} \leftarrow 3_{2,1}$ | 8.600 996 014 | $\nu_0, 35_{3,32} \leftarrow 36_{1,35}$ | 12.187 211 040 | $\nu_0, 5_{2,3} \leftarrow 4_{2,2}$ |
| 9.949 961 352 | $\nu_4, 4_{1,3} \leftarrow 3_{1,2}$ | 8.615 829 497 | $\nu_0, 10_{2,8} \leftarrow 11_{0,11}$ | 12.441 481 610 | $\nu_0, 12_{1,11} \leftarrow 12_{1,12}$ |
| 11.726 529 220 | $\nu_4, 5_{1,5} \leftarrow 4_{1,4}$ | 8.798 468 478 | $\nu_0, 36_{4,32} \leftarrow 36_{4,33}$ | 12.538 447 510 | $\nu_0, 5_{1,4} \leftarrow 4_{1,3}$ |
| 12.045 134 760 | $\nu_4, 5_{0,5} \leftarrow 4_{0,4}$ | 8.815 102 825 | $\nu_0, 10_{1,9} \leftarrow 10_{1,10}$ | 12.795 269 680 | $\nu_0, 20_{2,18} \leftarrow 20_{2,19}$ |
| 12.084 311 370 | $\nu_4, 5_{2,4} \leftarrow 4_{2,3}$ | 9.160 256 575 | $\nu_0, 18_{2,16} \leftarrow 18_{2,17}$ | | |
| 12.093 976 360 | $\nu_4, 5_{4,2} \leftarrow 4_{4,1}$ | 9.390 727 004 | $\nu_0, 4_{1,4} \leftarrow 3_{1,3}$ | | |
| 12.093 936 030 | $\nu_4, 5_{4,1} \leftarrow 4_{4,0}$ | 9.461 197 252 | $\nu_0, 27_{3,24} \leftarrow 27_{3,25}$ | | |

[a] $\sigma_{\rm new}$ denotes newly measured transition wavenumbers. The line assignments are given in the form of $\nu_i, J'_{K'_a,K'_c} \leftarrow J''_{K''_a,K''_c}$, where $\nu_i$ and $J_{K_a,K_c}$ represent the vibrational and the rotational assignment of the measured lines, respectively, $\nu_0$ refers to the ground vibrational state, while $\nu_3,\ \nu_4,$ and $\nu_6$ designate vibrational fundamentals (see Figure 4.1.1).

The new measurements consist of two complete $a$-type $^qR$-branch transitions ($J = 4 \leftarrow 3$ and $5 \leftarrow 4$) within the $\nu_0$, $\nu_3$, $\nu_4$, and $\nu_6$ bands, where $\nu_0$ denotes the ground vibrational state, and about 20 ground-state $P$ and $Q$ transitions with $\Delta K_a = 0$ or 2, with integrated intensity ranging from $10^{-23}$ and $10^{-27}$ cm molecule$^{-1}$. The uncertainty of our measurements is estimated to be 20 kHz and 2 kHz for Doppler-limited and Lamb-dip measurements, respectively. We label the seven Lamb-dip transitions of Table 4.1.4 with the reference tag 21AlTeYuMe, and the others as 21AlTeYuMe_S2, see Table 4.1.3.

Table 4.1.4: Rotational transitions of $H_2CO$ measured in this study at sub-Doppler resolution (Lamb-dip technique; accuracy: 2 kHz, $6.67 \times 10^{-8}$ cm$^{-1}$).[a]

| $\sigma_{\rm new}$/cm$^{-1}$ | Line assignment | $\sigma_{\rm lit}$/cm$^{-1}$ |
|---|---|---|
| 9.390 727 127 | $\nu_0, 4_{1,4} \leftarrow 3_{1,3}$ | 9.390 727 53(33) [65] |
| 9.694 153 448 | $\nu_0, 4_{0,4} \leftarrow 3_{0,3}$ | 9.694 153 31(33) [65] |
| 9.714 646 159 | $\nu_0, 4_{2,3} \leftarrow 3_{2,2}$ | 9.714 646 7(67) [72] |
| | | 9.714 646 0(67) [65] |
| 9.719 405 248 | $\nu_0, 4_{3,2} \leftarrow 3_{3,1}$ | 9.719 407(10) [65] |
| 9.719 536 101 | $\nu_0, 4_{3,1} \leftarrow 3_{3,0}$ | 9.719 532 8(33) [61] |
| 9.738 339 080 | $\nu_0, 4_{2,2} \leftarrow 3_{2,1}$ | 9.738 339 0(67) [72] |
| 10.034 829 847 | $\nu_0, 4_{1,3} \leftarrow 3_{1,2}$ | 10.034 830 00(33) [65] |

[a] In the first and last columns, the new, $\sigma_{\rm new}$, and the best previous, $\sigma_{\rm lit}$, transition wavenumbers are reported, respectively. The "Line assignment" column contains the assignments of the lines in the form of $\nu_0, J'_{K'_a,K'_c} \leftarrow J''_{K''_a,K''_c}$, where $J_{K_a,K_c}$ denotes the rotational assignment and $\nu_0$ refers to the ground vibrational band both for the upper and the lower state.

### Magic Numbers

The experimental transitions of $H_2CO$ form two distinct *ortho* and *para* SNs [95] in the MARVEL database. As is typical [19] in the MARVEL analysis of experimental transitions of species having *ortho* and *para* nuclear-spin isomers, the two components are connected by means of an artificial transition, informally denoted as "magic number", possibly taken from effective Hamiltonian fits [96]. For $H_2CO$, the artificial rotational transition is $J$ = $1_{1,1} \leftarrow 0_{0,0}$ and its frequency is 10.539 039 1 cm$^{-1}$ [70], which is the "magic number" of $H_2CO$.

## 4.1.4 Results and discussion

### Final energies

The MARVEL analysis produced 5029 validated ro-vibrational energy levels for $H_2CO$. The maximum rotational quantum number is $J = 38$, whereas the highest empirical energy is 6188 cm$^{-1}$. Table 4.1.5 displays the vibrational band origins (VBO) and an overview of the number of empirical ro-vibrational energy levels for each vibrational state. The $2\nu_3 + \nu_6$, $\nu_2 + \nu_5$, and $\nu_2 + \nu_3 + \nu_4$ bands have been omitted from the table because they contain only six rotational energy levels in total. Table 4.1.5 summarizes vibrational band origins for 14 vibrational modes, including the six fundamentals. The $\nu_2$, $\nu_3$, and $\nu_4$ fundamentals are determined very precisely because, in these cases, the upper states have been characterized by high-accuracy microwave studies. At least three transitions are attributed with each energy level belonging to these fundamentals. In contrast, the term values of the combination bands are defined by just one or two

transitions and are far less precise. Figure 4.1.2 is a representation of the $H_2CO$ SNs, depicting the upper-state energies of the observed transitions versus their corresponding lower-state energies. This figure also presents a visual impression of the number of transitions connecting them.

Table 4.1.5: MARVEL-based vibrational band origins (VBO) of $H_2CO$ and their literature counterparts obtained from accurate effective Hamiltonian fits.[a]

| Band | Symmetry | VBO(MARVEL) | $N_0$ | $N_{\rm RL}$ | $J_{\rm max}$ | VBO(lit) |
|---|---|---|---|---|---|---|
| $\nu_0$ | $a_1$ | 0.0 | 31 | 525 | 38 | 0.0 |
| $\nu_4$ | $b_1$ | 1167.256 76(10) | 6 | 346 | 30 | 1167.258(2) [81] |
| | | | | | | 1167.256 28(2) [36] |
| $\nu_6$ | $b_2$ | 1249.094 42(10) | 3 | 405 | 30 | 1249.091(2) [81] |
| | | | | | | 1249.094 68(2) [36] |
| $\nu_3$ | $a_1$ | 1500.174 50(10) | 4 | 382 | 30 | 1500.176(3) [81] |
| | | | | | | 1500.174 74(12) [36] |
| $\nu_2$ | $a_1$ | 1746.009 14(10) | 4 | 446 | 37 | 1746.008 9(1) [75] |
| | | | | | | 1746.008 86(13) [36] |
| $2\nu_4$ | $a_1$ | – | 0 | 65 | 11 | 2327.523 9(5) [39] |
| | | | | | | 2327.1(8) [97] |
| $\nu_4+\nu_6$ | $a_2$ | – | 0 | 47 | 11 | 2422.970 1(50) [39] |
| $2\nu_6$ | $a_1$ | – | 0 | 81 | 25 | 2494.354 3(5) [39] |
| $\nu_3+\nu_4$ | $b_1$ | – | 0 | 15 | 10 | 2667.048 1(20) [39] |
| | | | | | | 2655.5 [76] |
| $\nu_3+\nu_6$ | $b_2$ | 2719.156 04(50) | 1 | 232 | 25 | 2719.155 9(10) [76] |
| $\nu_1$ | $a_1$ | 2782.456 91(50) | 2 | 440 | 36 | 2782.456 9(10) [76] |
| $\nu_5$ | $b_2$ | 2843.323 54(12) | 4 | 388 | 35 | 2843.325 6(10) [76] |
| $\nu_2+\nu_4$ | $b_1$ | – | 0 | 153 | 24 | 2905.968 5(20) [39] |
| | | | | | | 2905(1) [76] |
| $2\nu_3$ | $a_1$ | – | 0 | 38 | 25 | 2998.987 3(5) [39] |
| | | | | | | 2999.5(5) [76] |
| $\nu_2+\nu_6$ | $b_2$ | 3000.065 74(50) | 1 | 100 | 21 | 3000.065 6(10) [76] |
| $2\nu_2$ | $a_1$ | 3471.720 8(78) | 2 | 373 | 31 | 3471.718(4) [80] |
| $\nu_1+\nu_4$ | $b_1$ | 3941.530 8(10) | 1 | 30 | 10 | – |
| $\nu_4+\nu_5$ | $b_2$ | 3996.518 6(10) | 1 | 35 | 9 | – |
| $\nu_3+\nu_5$ | $b_2$ | 4335.0989 4(10) | 1 | 170 | 24 | – |
| $2\nu_2+\nu_6$ | $b_2$ | – | 0 | 207 | 26 | 4734.207 8(50) [38] |
| $3\nu_2$ | $a_1$ | – | 0 | 176 | 26 | 5177.759 52(70) [38] |
| $2\nu_5$ | $a_1$ | 5651.196 4(15) | 1 | 179 | 20 | – |

[a]The VBO values are in $cm^{-1}$. The uncertainties are given in parentheses. The symmetry of the band, the number of transitions determining a particular VBO ($N_0$), as well as the number of rotational levels ($N_{\rm RL}$) and the maximum $J$ value within a given vibrational band are also displayed.

### Updated $H_2CO$ database

The ExoMol line list [98] for $H_2CO$ (denoted as AYTY) contains about 10 billion transitions connecting 10.3 million rotational-vibrational states. As part of this work, we replaced the

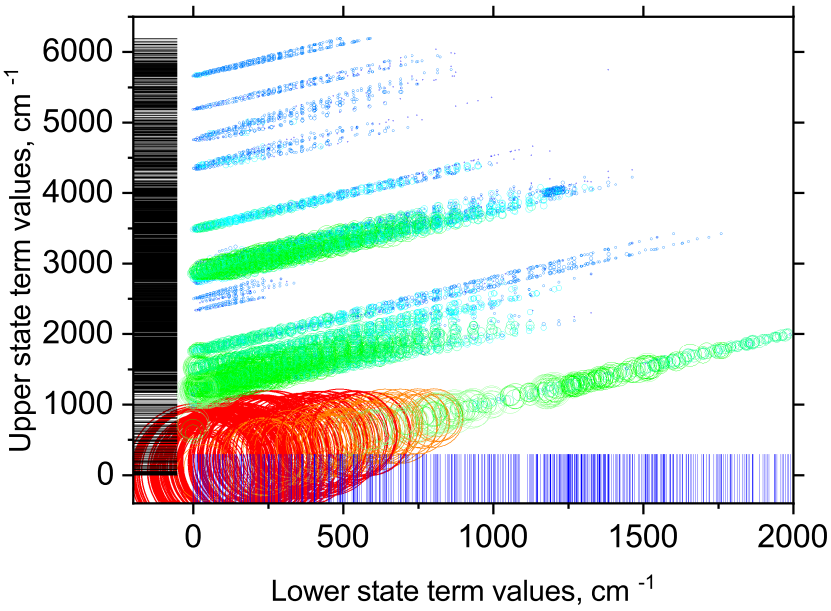


Figure 4.1.2: The upper-state energies of the experimental transitions used in this work, against corresponding lower-state energies of $H_2CO$. The vertical bars along the horizontal axis show the lower state energies, while the horizontal bars along the vertical axis give the upper state energies. Each circle represents a particular transition, with the size proportional to the number of transitions supporting the corresponding upper state. This value ranges from 1 (dark blue) to 102 (red).

energy levels in the AYTY list that were established empirically, using the MARVEL procedure. Compared to that spectral database, our analysis encompasses a broader frequency range. The HITRAN database [84] offers limited data on $H_2CO$: in addition to pure rotations, only two bands are covered. Figure 4.1.3 shows the comparison between the HITRAN and our MARVEL analysis. The good agreement indicates that this latter well covers these regions. Figure 4.1.3 also points out the relative (in)completeness of the HITRAN when used to simulate the spectra

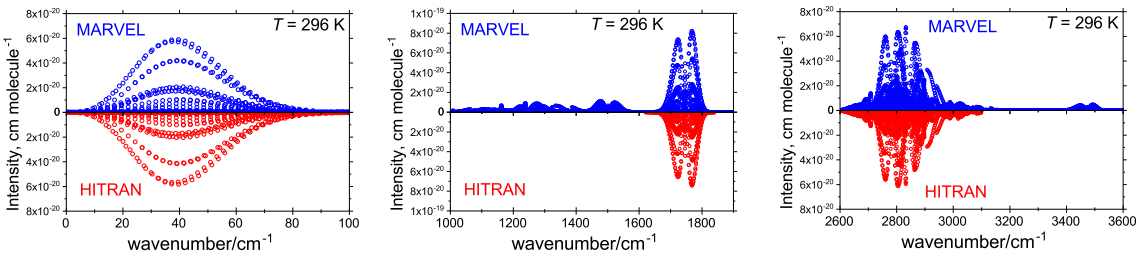


Figure 4.1.3: Room-temperature ($T = 296$ K) spectra of $H_2CO$ in three different regions covered by HITRAN 2016 [84]. The upper panels, in blue, show stick spectra simulated using the MARVEL energy term values from this work and the Einstein-$A$ coefficients from the AYTY line [98]. The lower panels, in red, show the corresponding spectra taken from HITRAN 2016.

of $H_2CO$ at room temperature. A few bands are missing in HITRAN, but this database can now be supplemented with our synthetic line list constructed using the line positions determined by MARVEL and AYTY.

### 4.1.5 Summary and conclusions

Apart from a few sources where the authors were reluctant to provide their published results for our analysis [36, 38, 39], all literature lines measured for $H_2CO$ were collected and analyzed. New measurements of rotational transitions within the ground, $\nu_3$, $\nu_4$, and $\nu_6$ states, namely seven lamb-dip lines and 82 Doppler-limited new frequencies, were added to the MARVEL database together with the literature sources. The study was carried out with the MARVEL approach and the xMARVEL algorithm. The present study is the first in a series where a MARVEL analysis is performed with the intention of updating an available line list.

## 4.2 Deuterated Hydrogen Sulfide

### 4.2.1 Introduction

Despite their apparent simple structure, small hydrides such as water ($H_2O$), methylene radical ($CH_2$), and amidogen radical ($NH_2$), can be difficult to accurately characterize. In fact, these light species are somewhat very floppy, thus showing large centrifugal and anharmonic effects [99, 100]. Therefore, a complete modeling of their ro-vibrational energy levels is a challenging task and it is difficult to achieve an accuracy that reflects that of experimental measurements. This is mainly due to the slow converge of the Watson Hamiltonian [101,102], which is the gold-standard model Hamiltonian used in ro-vibrational spectroscopy. Furthermore, the rotational spectra of these species are often complicated by the hyperfine structure [103–105]. Finally, the spectra of these hydrides are sparse, thus limiting the number of observable spectroscopic features.

However, these light species have a relevant role in astrochemistry. They are usually used to investigate the chemical differentiation and complexity across our Galaxy and beyond. Moreover, they are useful proxies of the evolutionary stage of astronomical objects [106–110]. Several simple hydrides species, including $H_2O$, $NH_2$, $CH_2$, $H_2S$, and some of their isotopologues, have already been detected in the ISM [111–123]. Among these small interstellar species, hydrogen sulfide ($H_2S$) is one of the most abundant S-bearing species in the ISM, and it is a promising proxy for exploring sulfur chemistry under astrophysical conditions [124–126], which is particularly interesting because of the "sulphur depletion problem" [127]. This might be related to the fact that S-containing species are locked in icy grain bulks, as suggested by the identification of $H_2S$ in cometary ices [128]. The astrophysical importance of $H_2S$ is clear. Furthermore, the observation of deuterium enrichment (or deuterium fractionation) for a given molecular species can shed light on its formation mechanism in the ISM. In view of what pointed out above, HDS can provide new insights into the issues of "sulphur depletion" and the deuterium fractionation.

Since the precise knowledge of the rotational-vibrational energy levels is crucial in astrochemical studies, in this work, we collected all the rotational and high-resolution ro-vibrational data available for HDS and analyzed them by means of the MARVEL algorithm. Our dataset is composed by previously published rotational and ro-vibrational transitions plus some unpublished high-resolution mm/submm-wave measurements performed in our laboratory in the

past years. The MARVEL results are expected to provide the most comprehensive database of ro-vibrational energy levels for HDS.

### 4.2.2 MARVEL Analysis

The description of the methodological details of MARVEL algorithm is presented in Chapter 2.

#### Quantum numbers labeling

HDS is an asymmetric-top molecule belonging to the $C_s$ point group. Its ro-vibrational energy levels are unequivocally labeled using six quantum numbers, as shown in Table 4.2.6. Three of them are the vibrational quantum numbers: $\nu_1$ is the S−D stretching, $\nu_2$ is the bending mode, and $\nu_3$ is the S−H stretching. The other three quantum numbers, $J$, $K_a$, and $K_c$, are the standard quantum numbers for the description the rotational energy levels of asymmetric rotors.

Table 4.2.6: The quantum numbers for labelling the upper and lower states of HDS.

| Label | Description |
|---|---|
| $\nu_1$ | S−D stretching ( 1902.85 $cm^{-1}$) |
| $\nu_2$ | Bend (1032.71 $cm^{-1}$) |
| $\nu_3$ | S−H stretching (2621.45 $cm^{-1}$) |
| $J$ | Rotational angular momentum |
| $K_a$ and $K_c$ | Projections of the rotational angular momentum |

#### Experimental sources

All spectroscopic data available in the literature for HDS have been collected, many of them dating before 2010. These were collected in the W@DIS (wadis.saga.iao.ru) database. They have been converted in the MARVEL format and combined with the unpublished measurements from our laboratory (223 new rotational transitions). There are 10 additional data sources available in literature. All these data are summarized in Table 4.2.7. Figure 4.2.1A shows the established SNs of HDS for the MARVEL analysis. The massive spectral network deriving from one of the (000000) nodes is presented in Figure 4.2.1B. Table 4.2.8 collects a summary of all the data sources with their energy range. In this table, A/V provides the number of assigned and validated transitions, respectively. Finally, Table 4.2.9 lists some of the data sources which had

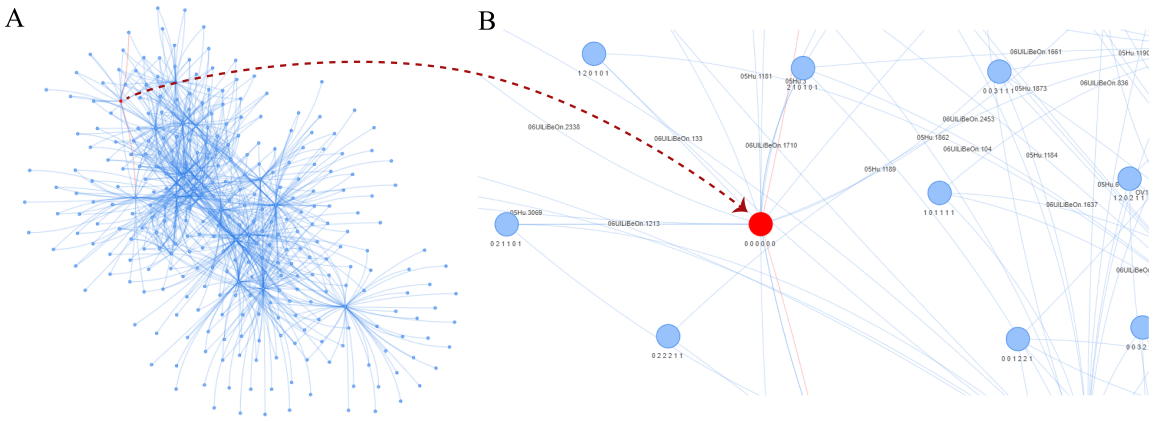


Figure 4.2.1: The SNs of HDS.

been considered but not used in MARVEL analysis, the reasons of their exclusion being also commented.

Comments on the experimental sources (Table 4.2.8) are warranted:

- 51HiSt [129]: 12 pure rotational $Q$-type transitions recorded in the vibrational ground state with $J$ values ranging from 1 to 12, in the frequency region from 0.265 $cm^{-1}$ to 2.520 $cm^{-1}$. This was the first experimental observation of rotational absorptions of HDS in the microwave region.

- 70Burrus [130]: 6 pure rotational transitions recorded in the vibrational ground state with the $J$ values of 1-3, in the 5.110 - 11.117 $cm^{-1}$ range. These transitions were measured by Helminger *et al.* [131] as well.

- 71HeCoLu [130]: 27 rotational transitions measured in the vibrational ground state in the 3.679 - 20.948 $cm^{-1}$ range.

Table 4.2.7: The required format of MARVEL input file for HDS.

| Wavenumber/$cm^{-1}$ | Uncertainty/$cm^{-1}$ | Upper state | Lower state | Reference Tag |
|---|---|---|---|---|
| 0.264741150[a] | 3.34E-06[a] | 0 0 0 6 4 2 | 0 0 0 6 4 3 | 51HiSt.1 |
| 0.264741150[a] | 3.34E-06[a] | 0 0 0 11 6 5 | 0 0 0 11 6 6 | 51HiSt.2 |
| 0.362286299[a] | 0.001 | 0 0 0 4 3 1 | 0 0 0 4 3 2 | 51HiSt.3 |
| 2585.041570 | 0.001 | 0 0 1 3 2 1[b] | 0 0 0 4 2 2 | 95UlToMeKo.1 |
| 2585.993090 | 0.001 | 0 0 1 3 2 1[b] | 0 0 0 4 1 3 | 95UlToMeKo.2 |
| 2587.901110 | 0.001 | 0 0 1 3 2 2[b] | 0 0 0 4 2 3 | 95UlToMeKo.3 |

[a] Frequencies and/or uncertainties converted from MHz to $cm^{-1}$. [b] Energy levels of $v_3 = 1$ vibrational excited state.

- 73Steenbec: 5 pure rotational transitions recorded in the vibrational ground state in the 0.280 - 1.426 $cm^{-1}$ range. These transitions have been retrieved from Lovas *et al.* [132].

- 85CaFlLeJo [133]: 535 pure rotational transitions measured in the FIR region (25.184 - 267.612 $cm^{-1}$), with a resolution of 0.004 $cm^{-1}$.

- 95UlToMeKo [134]: 69 ro-vibrational transitions recorded in the $\nu_3$ and $\nu_1 + \nu_2$ vibrational bands, in the 2585.042 - 2980.261 $cm^{-1}$ range.

Table 4.2.8: HDS data source segments and their characteristics

| TAG | Ref. | Range | A/V[a] | MiU[b] | MaU[c] | AvU[d] |
|---|---|---|---|---|---|---|
| 51HiSt | [129] | 0.265 - 2.520 | 12/12 | 3.3E-7 | 3.3E-7 | 3.3E-7 |
| 70Burrus | [130] | 5.110 - 11.117 | 6/6 | 3.3E-7 | 3.3E-7 | 3.3E-7 |
| 71HeCoDe | [130] | 3.679 - 20.948 | 27/27 | 3.3E-7 | 3.3E-7 | 3.3E-7 |
| 73Stee | [132] | 0.280 - 1.426 | 5/5 | 2.0E-6 | 3.0E-6 | 2.6E-6 |
| 23MeJiGaPu | This work | 8.157 - 53.038 | 223/223 | 3.0E-8 | 1.0E-5 | 1.4E-6 |
| 85CaFlLeJo | [133] | 25.184 - 267.612 | 535/535 | 2.0E-4 | 9.0E-4 | 2.3E-4 |
| 95UlToMeKo | [134] | 2585.042 - 2980.261 | 69/69 | 1.0E-3 | 1.0E-3 | 1.0E-3 |
| 19SyUlBeGr | [135] | 690.089 - 1511.468 | 2282/2282 | 1.0E-3 | 1.0E-3 | 1.0E-3 |
| 19UlBeGrRa | [136] | 2006.402 - 2939.482 | 1532/1532 | 1.0E-3 | 1.0E-3 | 1.0E-3 |
| 06UlLiBeOn | [137] | 3731.728 - 7219.680 | 2520/2520 | 2.0E-3 | 2.0E-3 | 2.0E-3 |
| 05LiGaChQi | [138] | 4951.018 - 8662.091 | 3379/2891 | 2.0E-3 | 2.0E-3 | 2.0E-3 |

[a] Assigned/Validated. [b] Minimum uncertainty. [c] Maximum uncertainty. [d] Average uncertainty.

- 19SyUlBeGr [135]: 2282 ro-vibrational transitions measured in the $\nu_2$ vibrational band, in the 690.089 - 1511.468 $cm^{-1}$ region.

- 19UlBeGrRa [136]: 1532 ro-vibrational transitions recorded in the $\nu_3$ vibrational band, in the 2006.402 - 2939.482 $cm^{-1}$ region.

- 05LiGaChQi [138]: 3379 ro-vibrational transitions belonging to the $2\nu_3$, $\nu_2 + 2\nu_3$, $3\nu_3$, and $\nu_2 + 3\nu_3$ bands, recorded in the region from 5000 $cm^{-1}$ to 9000 $cm^{-1}$. The lines with uncertainty larger than 0.01 $cm^{-1}$ have been discarded because not used by the authors in their fit. Wrong assignments have also been removed. Overall, 2891 valid lines have been employed in the MARVEL analysis.

- 06UlLiBeOn [137]: 2520 ro-vibrational transitions belonging to the $\nu_1 + 2\nu_2$, $\nu_1 + \nu_3$, $2\nu_2 + \nu_3$, $2\nu_1 + \nu_2$, $\nu_1 + \nu_2 + \nu_3$, $3\nu_1$, $\nu_1 + 2\nu_3$, and $2\nu_2 + 2\nu_3$ vibrational modes, measured

in the region from 3731.728 $cm^{-1}$ to 7219.680 $cm^{-1}$.

Table 4.2.9 summarizes the data sources that were considered but omitted from our MARVEL analysis. Explanations are provided in the following.

- 04Vladimir [139]: Variational calculations. No experimental data on ro-vibrational transitions are provided for HDS.
- 64Thaddeus [140]: hyperfine structure of $2_{2,0} \leftarrow 2_{2,1}$ transition resolved; however the corresponding unsplit frequency is not reported and we ignored the hyperfine splittings for simplicity.
- 95Ulenikov [141]: $\nu_2$ band of HDS, including its $^{34}$S isotopologue. Only the ro-vibrational term values are provided without the list of experimental transitions.
- 98Ulenikov1 [142]: high resolution IR spectra of the $\nu_1$, $2\nu_1$ and $\nu_2 + \nu_3$ bands. Only the ro-vibrational term values are provided without the list of experimental transitions.
- 98Ulenikov2 [143] high resolution IR spectra of the $2\nu_2$ and $3\nu_2$ bands. Only the ro-vibrational term values are provided without the list of experimental transitions.

### 4.2.3 Results and discussion

10377 ro-vibrational transitions of HDS from 10 different publications were incorporated in the MARVEL database, with 223 new rotational transitions from our laboratory being included in the final analysis. In total, 10057 transitions have been connected in the main SN of HDS. The MARVEL results produced 2541 validated ro-vibrational energy levels. The highest energy level lies at 9552.886 $cm^{-1}$ and belongs to the $v_2 + 3v_3$ combination state, while the highest energy level of the vibrational ground state is the $J_{K_a,\,K_c} = 18_{14,\,4}$ rotational level at 2458.727

Table 4.2.9: Data source considered but not used in this work.

| TAG | Ref. | Comments |
|---|---|---|
| 04Vladimir | [139] | Data source does not list any ro-vibrational transitions |
| 64Thaddeus | [140] | Only one hyperfine-resolved transition reported, not used for simplicity |
| 95Ulenikov | [141] | Only term values are provided ($\nu_2$ band of the HDS) |
| 98Ulenikov1 | [142] | Only term values are provided ($\nu_1$ and $2\nu_1/\nu_2 + \nu_3$ bands of HDS) |
| 98Ulenikov2 | [143] | Only term values are provided ($2\nu_2$ and $3\nu_2$ bands of HDS) |

Table 4.2.10: Summary of the energy levels derived from the MARVEL analysis. Results are collected state-by-state [a].

| State ($v_1v_2v_3$) | $J$ range | $K_a$ range | Levels | MiU – MaU ($cm^{-1}$) | AvU ($cm^{-1}$) | Energy Range ($cm^{-1}$) |
|---|---|---|---|---|---|---|
| 0 0 0 | 0 – 25 | 0 – 15 | 372 | 0.0000 – 0.0071 | 0.0013 | 0.0000 – 2458.7271 |
| 0 0 1 | 0 – 22 | 0 – 14 | 293 | 0.0010 – 0.0064 | 0.0015 | 2621.4558 – 4624.0959 |
| 0 0 2 | 0 – 23 | 0 – 11 | 214 | 0.0020 – 0.0054 | 0.0023 | 5147.3553 – 6960.4715 |
| 0 0 3 | 0 – 20 | 0 – 7 | 130 | 0.0020 – 0.0050 | 0.0022 | 7577.8435 – 9089.2572 |
| 0 1 0 | 0 – 25 | 0 – 16 | 381 | 0.0010 – 0.0077 | 0.0019 | 1032.7151 – 3852.8277 |
| 0 1 2 | 0 – 20 | 0 – 12 | 219 | 0.0020 – 0.0050 | 0.0023 | 6139.7320 – 7744.0663 |
| 0 1 3 | 0 – 17 | 0 – 6 | 116 | 0.0020 – 0.0032 | 0.0021 | 8548.8927 – 9552.8861 |
| 0 2 1 | 0 – 19 | 0 – 8 | 97 | 0.0020 – 0.0048 | 0.0022 | 4638.8489 – 5893.7850 |
| 0 2 2 | 0 – 16 | 0 – 6 | 71 | 0.0020 – 0.0042 | 0.0021 | 7123.8864 – 8022.9404 |
| 1 0 1 | 0 – 21 | 0 – 11 | 227 | 0.0020 – 0.0057 | 0.0025 | 4522.6485 – 6187.8216 |
| 1 0 2 | 1 – 10 | 0 – 5 | 66 | 0.0020 – 0.0022 | 0.0020 | 7055.1149 – 7502.1927 |
| 1 1 0 | 3 – 3 | 0 – 3 | 7 | 0.0010 – 0.0010 | 0.0010 | 2971.5943 – 3027.4063 |
| 1 1 1 | 2 – 7 | 0 – 4 | 15 | 0.0020 – 0.0020 | 0.0020 | 5548.9136 – 5845.9678 |
| 1 2 0 | 0 – 16 | 0 – 10 | 131 | 0.0020 – 0.0046 | 0.0022 | 3938.6388 – 5541.4066 |
| 2 1 0 | 0 – 19 | 0 – 10 | 189 | 0.0020 – 0.0046 | 0.0022 | 4767.7069 – 6010.9407 |
| 3 0 0 | 2 – 8 | 0 – 1 | 12 | 0.0020 – 0.0020 | 0.0020 | 5583.5559 – 5809.1718 |

[a] See notes of Table 4.2.8.

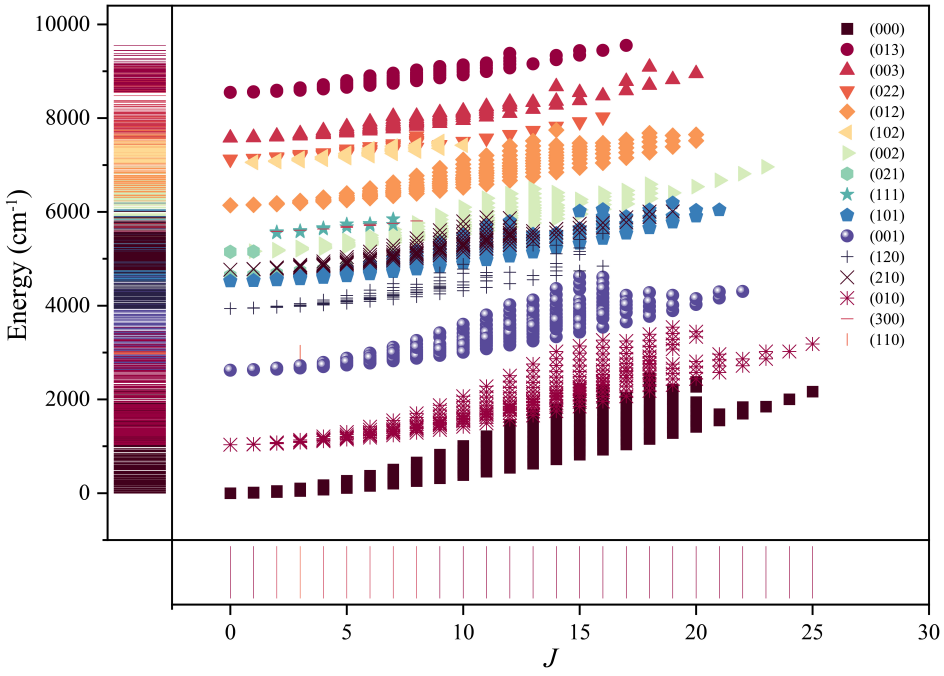


Figure 4.2.2: The MARVEL energy levels derived from the HDS spectroscopic network. The horizontal axis refers to the $J$ values of the energy levels, while the vertical axis reports the energies of each levels. Each vibrational state is represented by a different symbol, for which a legend is provided using the format ($v_1v_2v_3$).

$cm^{-1}$. The average uncertainty is of the order of $2 \times 10^{-3}\,cm^{-1}$. Figure 4.2.2 depicts the HDS spectroscopic network, thus showing MARVEL energy levels versus their corresponding rotational quantum number $J$.

Table 4.2.10 provides an overview of the number of empirical ro-vibrational energy levels for each vibrational state, for a total of 16 vibrational states. Moreover, 45 transitions of our global database connect floating levels only. These are not linked to any level of the main spectroscopic network and therefore the energy of the corresponding levels could not be calculated. The energy levels of $v_1 + v_2$, $v_1 + v_2 + v_3$, $v_1 + 2v_2 + v_3$, $3v_1$ are by far less precise than the others because they have been derived from only few transitions.

### 4.2.4 Conclusion

On the basis of the available HDS spectral data in the literature – in combination with new, unpublished highly accurate measurements from our laboratory – we have obtained the most comprehensive database of energy levels for HDS to date. This is an important result because, among high-resolution spectral databases such as `HITRAN` [144], no one provides access to HDS spectral information. The CDMS database [2,3] and JPL Catalog [4], which are commonly used in the astronomical field, only partially contain the rotational transitions for the vibrational ground state. It is worth mentioning that the MARVEL database is able to predict unknown transitions based on the selection rules and experimental energy levels.

## 4.3 Deuterated Cyanoacetylene

### 4.3.1 Introduction

Cyanoacetylene ($HC_3N$) is a widespread molecule in the ISM. Its abundance is such that isotopic species have also been discovered in space. The deuterated isotopologue $DC_3N$ was first discovered in the dark cloud TMC-1 (Taurus Molecular Cloud 1) through the observation in emission of its $J = 5 - 4$ rotational transition lying at about 42.2 GHz [145]. Subsequently, deuterated cyanoacetylene has been extensively observed in cold molecular clouds, such as L1498, L1544, L1521B, L1400K, and L1400G [146], as well as in the hot cores of the high-mass star-forming regions Orion KL and Sagittarius B2(N) [147, 148]. Recently, $DC_3N$ has been employed to investigate the evolutionary stage of massive star-forming regions: Rivilla et al. [149] detected the emission of $DC_3N$ ($J = 11 - 10$ transition) in a sample of 15 sources containing both cold and warm high-mass star-forming cores, and acquired the first emission map of $DC_3N$ in the high-mass proto-cluster IRAS 05358+3543.

The astrophysical relevance of $DC_3N$ is related both to the ubiquitous presence of its parent species ($HC_3N$) in space and to its deuteration. Indeed, the study of interstellar D-containing molecules provides important information on the properties and the evolution of star-forming regions (see, e.g., Ref. [150], and references therein), and is a key tool to follow the chemical history of the materials which eventually enter into the composition of planetary bodies.

The laboratory spectroscopic knowledge of $DC_3N$ is not homogeneous over the full spectral range of interest to astronomy. While the rotational spectrum of $DC_3N$ has been accurately studied and it is well suited to guide astronomical observations at millimeter wavelengths, a detailed knowledge of its IR spectrum is limited to the spectral range between 200 and 1100 $cm^{-1}$ [151]. At higher frequencies, only low-accuracy spectroscopic data are available in the literature [152]. The same applies to the MIR spectrum of $HC_3N$ above 1000 $cm^{-1}$, for which the ro-vibrational bands were recorded either at low resolution (0.025 and 0.050 $cm^{-1}$) [152] or in a narrow spectral interval [153–155]. Such patchy results were mainly due to the type of instrumentation employed, i.e., Ebert-type and Diode-laser spectrometers. Currently, these limitations are easily overcome by employing FT-IR spectrometers, which offer the possibility of recording high-resolution ro-vibrational spectra in a wide frequency range.

To fill the lack of information described above, a comprehensive investigation of the high-resolution MIR spectra of $DC_3N$ and $HC_3N$ has been carried out using FT-IR spectroscopy.

In addition, the pure rotational spectra in some vibrational excited states of $DC_3N$ have been recorded in order to determine highly-accurate spectroscopic parameters. The new assignments of the IR and millimeter-wave spectra were combined into a single global fit from which a consistent set of spectroscopic constants has been determined. The present analysis of $DC_3N$ provides a highly-precise rest-frequency catalog useful for astronomical observations.

### 4.3.2 Experimental details

The $DC_3N$ sample was synthesized in Rennes by Prof. J.-C. Guillemin following the procedure described in Ref. [156]. In brief, the dropwise addition of methyl propanol ($HC{\equiv}CCOOCH_3$) to liquid ammonia yields a 100% conversion into propanolamide ($HC{\equiv}CCONH_2$). The latter was subsequently mixed with phosphonic anhydride ($P_4O_{10}$) and calcined white sand and heated at 470 K for more than 2 h. Using a liquid nitrogen-cooled trap, pure $HC_3N$ could be collected during the process. Then, $HC_3N$ (3 g), heavy water ($D_2O$, 4 mL) and potassium carbonate ($K_2CO_3$, 50 mg) were mixed together in an inert atmosphere. The diphasic mixtures were then stirred at room temperature for about 20 min. Subsequently, a portion of the $DC_3N$ sample was condensed in the vacuum line through a 77 K cooled trap. The procedure of the addition of $D_2O$ and $K_2CO_3$ was replicated three times. Finally, almost pure $DC_3N$ ($> 98\%$ ) could be condensed in a trap cooled at 150 K after removing the residual $D_2O$ by vaporisation on $P_4O_{10}$.

#### Fourier-transform IR interferometer

IR spectra of $DC_3N$ and $HC_3N$ were recorded in the 1500–3500 $cm^{-1}$ range with the Bomem DA3.002 FT-IR [157, 158] described in Chapter 3. Two spectra were recorded in the 1500–3500 $cm^{-1}$ region using different pressures of $DC_3N$, namely 16 and 32 Pa, at a nominal resolution of 0.004 $cm^{-1}$. Both of them were obtained from the co-addition of 140–200 scans, for a total integration time of 13–18 hours. The frequency axis of the spectra was calibrated by using about 50 transitions of $H_2O$ and $CO_2$ as references, whose wavenumbers were taken from the `HITRAN` database [84]. On average, the calibration residuals are about $5 \times 10^{-5}$ $cm^{-1}$. Absorptions due to $HC_3N$ were also detected in the same spectra with a good S/N because of the hydrogen-deuterium (H/D) exchange occurring in the multipass cell. The line-center frequencies were retrieved with the `PGOPHER` software [159] using the maximum intensity of the lines and their uncertainty is assumed to be $4 \times 10^{-4}$ $cm^{-1}$ in all cases.

**Frequency-modulation millimeter/submillimeter-wave spectrometer**

Pure rotational transitions of $DC_3N$ were recorded in three high-energy vibrational states using the FM-mmW spectrometer described in Chapter 3. For the present measurements, the temperature of the furnace was set to 700 °C in order to increase the population of $DC_3N$ in excited states, while a small flow ($\sim$ 1 Pa) of $DC_3N$ was ensured inside the cell. The accuracy of the retrieved frequencies is estimated to be 30 kHz.

### 4.3.3 Analysis and Results

**Theoretical background**

$DC_3N$ is a closed shell linear molecule which possesses seven vibrational modes: four stretching modes ($\nu_1$, $\nu_2$, $\nu_3$, $\nu_4$; $\Sigma$ symmetry) and three doubly-degenerate bending modes ($\nu_5$, $\nu_6$, $\nu_7$; $\Pi$ symmetry), all of them being IR-active. The low-lying vibrational modes ($\nu_4$, $\nu_5$, $\nu_6$, $\nu_7$) as well as some of their overtone and combination states have been extensively analyzed in the literature [151]. In the present work, the focus was on the fundamental transitions of the $\nu_1$, $\nu_2$, and $\nu_3$ stretching modes, and their hot bands ($\nu_1 + \nu_7 - \nu_7$, $\nu_2 + \nu_7 - \nu_7$, and $\nu_3 + \nu_7 - \nu_7$), which all lie in the MIR region.

The effective Hamiltonian employed in this work to analyze the ro-vibrational transitions of both $DC_3N$ and $HC_3N$, and to retrieve the spectroscopic parameters is described in Ref. [160]. Since the present study focuses on the analysis of three stretching states ($\Sigma$ symmetry) and their $\nu_7$-associated hot bands, the Hamiltonian can be simplified as:

$$H = H_{rv} + H_{\ell-type} \tag{4.2}$$

where $H_{rv}$ is the ro-vibrational Hamiltonian and $H_{\ell-type}$ describes the $\ell$-type interaction between $\ell$ sub-levels of the excited bending states.

In the ro-vibrational part, the diagonal elements of the Hamiltonian can be expressed as:

$$\begin{aligned}\langle \ell_7, k|H_{rv}|\ell_7, k\rangle = G_v + \chi_{L(77)}{\ell_7}^2 + (B_v + d_{JL(77)}{\ell_7}^2)f(J,k) \\ - (D_v + h_{JL(77)}{\ell_7}^2)f(J,k)^2 + (H_v + l_{JL(77)}{\ell_7}^2)f(J,k)^3\end{aligned} \tag{4.3}$$

where $G_v$ is the pure vibrational energy, $B_v$ is the rotational constant, and $D_v$ and $H_v$ are the quartic and sextic centrifugal distortion constants, respectively, of the vibrational state $\nu$. The

dependence of these four constants on the vibrational angular momentum $\ell_7$ is expressed by the terms $\chi_{L(77)}$, $d_{JL(77)}$, $h_{JL(77)}$, and $l_{JL(77)}$.

As far as the vibrational $\ell$-type doubling term is concerned, the elements with $|\Delta k|$=2 can be written as:

$$\begin{aligned}&\langle \ell_7 \pm 2, k \pm 2 | H_{\ell-type} | \ell_7, k \rangle \\ &= \frac{1}{4}[q_7 + q_{7J} J(J+1) + q_{7JJ} J^2 (J+1)^2] \times \sqrt{(v_7 \mp \ell_7)(v_7 \pm \ell_7 + 2)} \times \sqrt{f_{\pm 2}(J,k)}\end{aligned} \tag{4.4}$$

The functions $f(J,k)$ and $f_{\pm n}(J,k)$ appearing in the equations above are defined as follows:

$$f(J,k) = J(J+1) - k^2\,, \tag{4.5}$$

$$f_{\pm n}(J,k) = \prod_{p=1}^{n} J(J+1) - [k \pm (p-1)](k \pm p)\,. \tag{4.6}$$

### 4.3.4 Spectral features

For both $DC_3N$ and $HC_3N$, the $\nu_1$, $\nu_2$, and $\nu_3$ stretching bands are located between 1900 and 3400 cm$^{-1}$ ($2.9 - 5.3$ $\mu$m). An overview of the vibrational bands recorded in this work is provided in Figure 4.3.1. From the inspection of this figure, it is evident that all the twelve bands observed and analyzed show the typical contour of the $\Sigma - \Sigma$ or $\Pi - \Pi$ bands of a linear rotor, thus presenting well-defined $P$ and $R$ branches, but no $Q$ branch.

While the absolute intensities of $DC_3N$ bands are quite similar to each other ($\nu_1 = 81$ atm$^{-1}$ cm$^{-2}$, $\nu_2 = 50$ atm$^{-1}$ cm$^{-2}$, and $\nu_3 = 39$ atm$^{-1}$ cm$^{-2}$ [156]), the situation is different for $HC_3N$ ($\nu_1 = 249$ atm$^{-1}$ cm$^{-2}$, $\nu_2 = 41$ atm$^{-1}$ cm$^{-2}$, and $\nu_3 = 8$ atm$^{-1}$ cm$^{-2}$ [161]), with an overall variation of more than one order of magnitude. Furthermore, the hot-bands analyzed in this work ($\nu_1 + \nu_7 - \nu_7$, $\nu_2 + \nu_7 - \nu_7$, and $\nu_3 + \nu_7 - \nu_7$) are nearly three times weaker than the corresponding fundamental bands because of the Boltzmann factor at room temperature (the energy of the $v_7 = 1$ state is 221.8 cm$^{-1}$). Spectral recordings were performed employing various pressure values to account for these different band intensities, and to obtain a homogeneous S/N for a wide range of $J$ values.

In addition to the IR measurements, pure rotational spectra of three vibrational excited states of $DC_3N$ were recorded between 243 and 295 GHz. In detail, some $J + 1 \leftarrow J$ rotational transitions have been observed for the $v_3 = 1$, $v_2 = 1$, and $v_3 = v_7 = 1$ states, with $J$ ranging

from 28 to 34. Both $v_3 = 1$ and $v_2 = 1$ are $\Sigma$ states and their rotational spectra appear like a sequence of (almost) equally-spaced lines, while the $v_3 = v_7 = 1$ state has a $\Pi$ symmetry, thus showing a series of doublets due to the $\ell$-type resonance.

### Analysis of the spectra

The analysis of the ro-vibrational and pure rotational spectra has been performed with the aid of the PGOPHER program [159] and the CALPGM suite [162]. Initially, more than 1500 ro-vibrational transitions of $DC_3N$ belonging to the $\nu_1$, $\nu_2$, and $\nu_3$ fundamental bands and to their $\nu_1+\nu_7-\nu_7$, $\nu_2+\nu_7-\nu_7$, and $\nu_3+\nu_7-\nu_7$ hot-bands were assigned, and they include high-$J$ transitions up to $J = 110$. However, not all the ro-vibrational transitions assigned could be incorporated in the fit with the estimated experimental accuracy. In particular, the $\nu_2+\nu_7-\nu_7$ hot-band exhibited some deviations from our modelling, especially for transitions with $J$ between 10 and 15. To check and correct possible misassignments, we have also employed the Loomis-Wood for Windows (LWW) program package for symmetric-top molecules [163], which revealed no

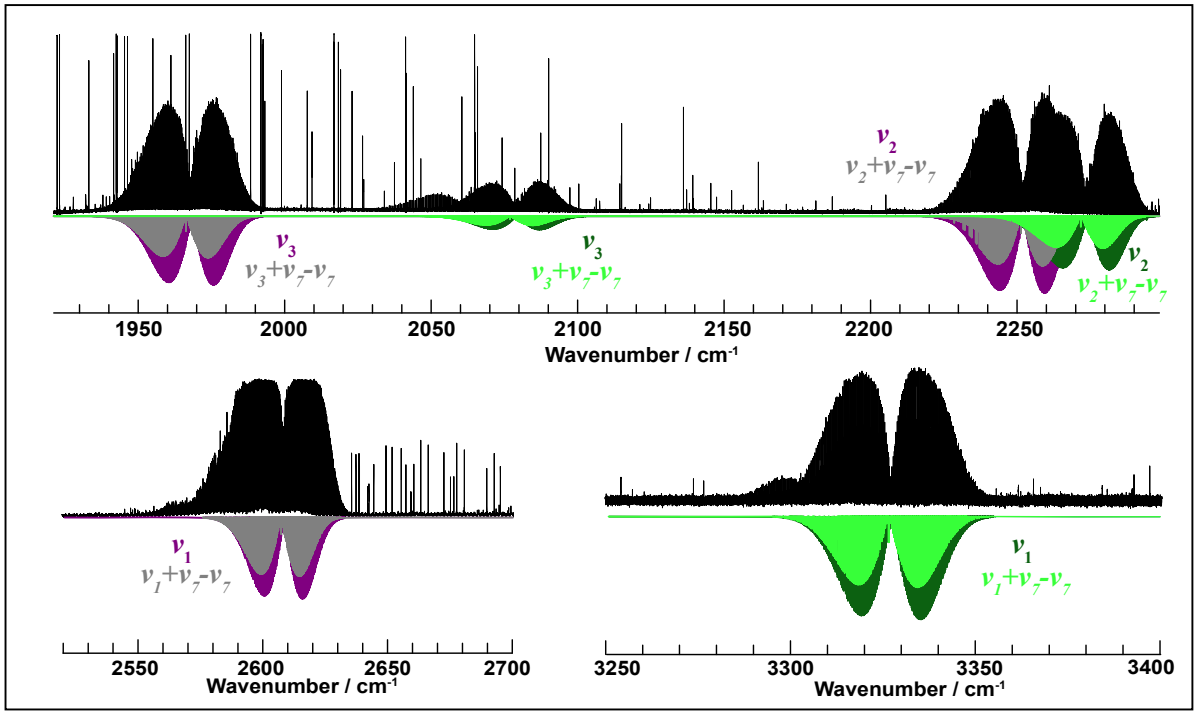


Figure 4.3.1: Portions of the recorded MIR spectra (black traces): 1930-2300 $cm^{-1}$, 2500-2700 $cm^{-1}$ and 3250-3400 $cm^{-1}$. Spectral simulations based on the spectroscopic constants of Tables 4.3.11 and 4.3.13 are reported for both $DC_3N$ (violet traces) and $HC_3N$ (green traces). Recording conditions: $T$ = 298 K, $P$ = 16–32 Pa (top and bottom-left: 32 Pa, bottom-right: 16 Pa), $L_{opt}$ = 8 m, 140–200 scans, unapodized resolution 0.004 $cm^{-1}$.

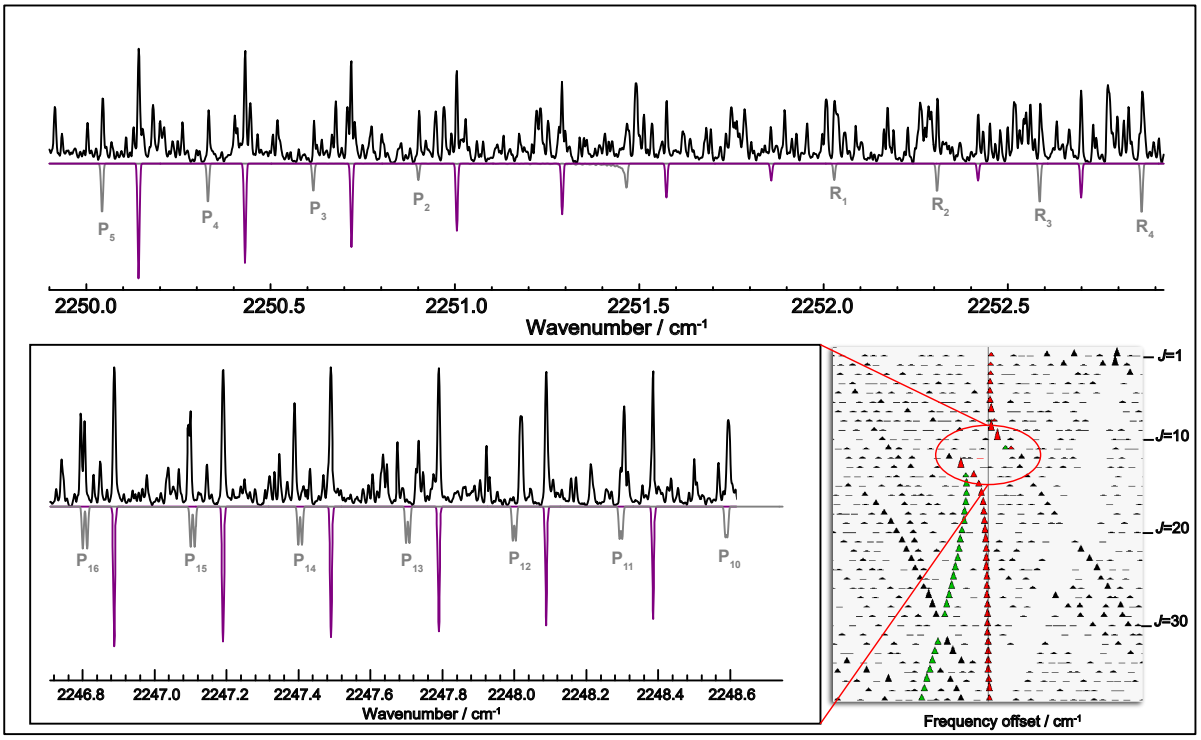


Figure 4.3.2: *(Top panel)*: Portions of the $\nu_2 + \nu_7 - \nu_7$ band of $DC_3N$. Recording conditions: $T$ = 298 K, $P$ = 32 Pa, $L_{\rm opt}$ = 8 m, 200 scans, unapodized resolution 0.004 $cm^{-1}$. *(Bottom panel)*: Detail of the spectrum (*left*) together with its Loomis-Wood plot (*right*) where the strongest perturbations are visible. Additional lines present in the spectra arise from other hot-bands not considered in this study.

errors in our assignments, through both the graphical diagrams and the Ground State Combination Differences (GSCDs) method. Possible perturbations due to a nearby state are therefore plausible. However, the identification of the perturbing state is not feasible at these energies because of the very large number of unknown ro-vibrational levels. Since a complete treatment of all the anharmonic resonances was beyond the goal of this work, an effective approach was adopted and lines showing the largest deviations (10 in total) were removed from the analysis. The comparison between the simulation based on our analysis and the observed $\nu_2 + \nu_7 - \nu_7$ ro-vibrational transitions is shown in Figure 4.3.2, together with the corresponding Loomis-Wood plot.

The analysis of the other five bands was instead rather straightforward and satisfactory, with the Hamiltonian of Eqs. (4.2)–(4.4) able to well reproduce all experimental data within their nominal uncertainty. The quality of the band analyses can be inferred from the root-mean-square (rms) errors of the fits, which are reported in Table 4.3.12.

The spectroscopic constants determined from the preliminary analysis of the six bands of

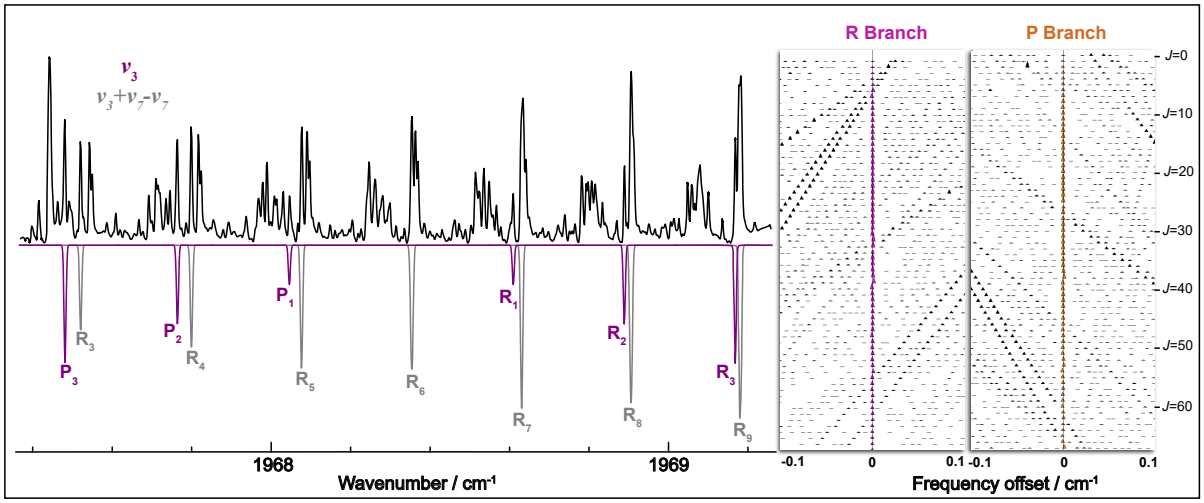


Figure 4.3.3: *(Left panel)*: Portions of the $DC_3N$ spectrum in the region of the $\nu_3$ band system. Recording conditions: same as Figure 4.3.2. *(Right panel)*: Loomis-Wood plots of the $P$ and $R$ branches of the $\nu_3$ band. Additional lines present in the spectra arise from other hot-bands not considered in this study.

$DC_3N$ were used to predict its pure rotational spectrum in the $v_3 = 1$, $v_2 = 1$, and $v_3 = v_7 = 1$ states, which are the three lowest energy states among those investigated in this work. A total of 21 pure rotational transitions, which do not suffer from contamination of nearby lines, have been successfully recorded and then added to the data-set in order to improve the accuracy of the spectroscopic parameters determined in the fit. It should be pointed out that, although the analysis of the $\nu_3$ band gave no hint of perturbations (as evident from its LWW plot in Figure 4.3.3) and the fit has a rms error as low as $3.4 \times 10^{-4}$ cm$^{-1}$, the rotational transitions recorded in the $v_3 = 1$ state show deviations about 10 times larger than the expected error, i.e. around 300 kHz. Once again, a plausible explanation is that the $v_3 = 1$ state is involved in an anharmonic interaction with one or more vibrational states close in energy, but such perturbation is moderately weak and hidden in the larger uncertainty of the IR data. Nonetheless, despite these somewhat large residuals, the inclusion of pure rotational lines reduces the uncertainty of the derived spectroscopic parameters by up to a factor of 3. The upper states spectroscopic parameters determined from the combined analysis of rotational and ro-vibrational transitions are collected in Table 4.3.11. The spectroscopic constants of the ground and $v_7 = 1$ states, i.e., the lower levels involved in the current analysis, were kept fixed at the values determined in the literature (see Tables 4–5 of Ref. [151]).

As far as $HC_3N$ is concerned, being a side-product of our spectral recording, we limited the analysis to its IR spectrum. With the only exception of a few small deviations involving blocks

of 2–3 consecutive $J$ levels, no evident perturbations were observed during the assignment procedure and/or at the fitting stage. Overall, for $HC_3N$, 1221 different lines were assigned to the $\nu_1$, $\nu_2$, and $\nu_3$ fundamental bands and their corresponding hot bands originating from the $v_7 = 1$ state. Similarly to $DC_3N$, the vibrational energies $G_v$ and the rotational constants $B_v$ were determined with high precision for all the six vibrational excited states. Accurate values

Table 4.3.11: Spectroscopic constants[a] determined for $DC_3N$.

| Constant | Unit | $v_1 = 1$ | $v_2 = 1$ | $v_3 = 1$ | $v_1 = v_7 = 1$ | $v_2 = v_7 = 1$ | $v_3 = v_7 = 1$ |
|---|---|---|---|---|---|---|---|
| $G_v$ | $cm^{-1}$ | 2608.5183(2) | 2252.1388(1) | 1968.3280(1) | 2818.8187(1) | 2463.0161(1) | 2177.9480(1) |
| $\chi_{77}$ | GHz | | | | 19.5125[b] | 19.5125[b] | 19.5125[b] |
| $B_v$ | MHz | 4210.218(5) | 4203.792(2) | 4209.911(2) | 4223.177(2) | 4216.951(3) | 4222.925(2) |
| $D_v$ | kHz | 0.445(1) | 0.4555(7) | 0.4541(5) | 0.4678(3) | 0.4583(4) | 0.4757(8) |
| $H_v$ | mHz | 0.14(7) | 0.39(5) | 0.15(4) | 0.0394[c] | 0.0394[c] | 0.0394[c] |
| $d_{J77}$ | kHz | | | | -9.971[b] | -9.971[b] | -9.971[b] |
| $q_7$ | MHz | | | | 5.900(3) | 5.129(3) | 5.942(2) |
| $q_{J7}$ | Hz | | | | -12.3(4) | -25.4(6) | -13.9(3) |

[a] Numbers in parentheses represent $1\sigma$ errors in units of the last significant digit. [b] Fixed at the $v_7 = 1$ value [151] . [c] Fixed at the ground state value [151].

Table 4.3.12: Summary of the ro-vibrational bands recorded and analyzed in this work.

| Species | Band | Sub-band | $J$ max | Freq. Range ($cm^{-1}$) | Lines | rms error ($10^{-4}$ $cm^{-1}$) |
|---|---|---|---|---|---|---|
| $DC_3N$ | | | | | | |
| | $\nu_1$ | $\Sigma - \Sigma$ | 110 | 2600-2633 | 189 | 3.5 |
| | $\nu_2$ | $\Sigma - \Sigma$ | 105 | 2251-2273 | 199 | 3.6 |
| | $\nu_3$ | $\Sigma - \Sigma$ | 110 | 1968-1992 | 219 | 3.4 |
| | $\nu_1 + \nu_7$-$\nu_7$ | $\Pi - \Pi$ | 100 | 2606-2632 | 269 | 6.3 |
| | $\nu_2 + \nu_7$-$\nu_7$ | $\Pi - \Pi$ | 91 | 2252-2220 | 284 | 20.3 |
| | $\nu_3 + \nu_7$-$\nu_7$ | $\Pi - \Pi$ | 97 | 1965-1991 | 292 | 4.1 |
| $HC_3N$ | | | | | | |
| | $\nu_1$ | $\Sigma - \Sigma$ | 91 | 3290-3360 | 174 | 5.0 |
| | $\nu_2$ | $\Sigma - \Sigma$ | 91 | 2240-2300 | 161 | 4.0 |
| | $\nu_3$ | $\Sigma - \Sigma$ | 87 | 2050-2110 | 169 | 3.7 |
| | $\nu_1 + \nu_7$-$\nu_7$ | $\Pi - \Pi$ | 78 | 3300-3350 | 225 | 6.0 |
| | $\nu_2 + \nu_7$-$\nu_7$ | $\Pi - \Pi$ | 93 | 2245-2295 | 240 | 4.3 |
| | $\nu_3 + \nu_7$-$\nu_7$ | $\Pi - \Pi$ | 71 | 2052-2097 | 252 | 4.0 |

for the centrifugal distortion constant $D_v$ and the $\ell$-type doubling constant $q_7$ were derived as well. Table 4.3.13 lists the complete set of upper state spectroscopic parameters used in the final fit, while the quality of the analysis is demonstrated by the low rms error achieved for each band (see Table 4.3.12). Also in this case, the spectroscopic constants of the ground and $v_7 = 1$ states were kept fixed at the values determined in the literature (see Table 5 of Ref. [160]).

Table 4.3.13: Spectroscopic constants[a] determined for $HC_3N$.

| Constant | Unit | $v_1 = 1$ | $v_2 = 1$ | $v_3 = 1$ | $v_1 = v_7 = 1$ | $v_2 = v_7 = 1$ | $v_3 = v_7 = 1$ |
|---|---|---|---|---|---|---|---|
| $G_v$ | $cm^{-1}$ | 3327.37141(7) | 2273.99485(7) | 2079.30610(7) | 3548.40903(7) | 2493.65068(6) | 2298.77771(8) |
| $\chi_{77}$ | GHz | | | | 21.7972[b] | 21.7972[b] | 21.7972[b] |
| $B_v$ | MHz | 4541.774(2) | 4527.493(2) | 4535.116(2) | 4556.205(2) | 4541.989(1) | 4549.738(5) |
| $D_v$ | kHz | 0.5401(2) | 0.5380(2) | 0.5412(3) | 0.5542(3) | 0.5608(2) | 0.569(3) |
| $H_v$ | mHz | 0.0509[c] | 0.0509[c] | 0.0509[c] | 0.0509[c] | 0.0509[c] | 0.0509[c] |
| $d_{J77}$ | kHz | | | | -12.287[b] | -12.287[b] | -12.287[b] |
| $q_7$ | MHz | | | | 6.543(2) | 6.650(2) | 6.457(3) |
| $q_{J7}$ | Hz | | | | -17.3(5) | -18.3(3) | -14.9(7) |

[a] Numbers in parentheses represent $1\sigma$ errors in units of the last significant digit. [b] Fixed at the $v_7 = 1$ value [160] . [c] Fixed at the ground state value [160].

### 4.3.5 Discussion and Conclusions

The improvement of the ground-based IR facilities (e.g., CRIRES+ at VLT) and the perspectives opened by the forthcoming JWST telescope have brought a considerable interest to the ro-vibrational spectrum of simple interstellar molecules, both at low and high wavenumbers. In particular, the possibility of probing the inner portions of young proto-planetary disks where the material is funneled into the planetary formation zone and — at later stages — to directly observe the atmospheres of the mature exoplanets, makes the stretching spectral interval (1500 – 3500 $cm^{-1}$) of particular interest due to its selectivity to the high gas temperatures typical of these regions. In this context, a detailed knowledge of the associated hot bands is as important as that of the fundamentals. In high excitation conditions, many vibrational states are significantly populated and the corresponding satellite features are able to make up a considerable amount of the retrieved flux. Hot bands are thus critical to accurately model the shape of the band profile and to retrieve reliable column densities. The laboratory detection of accurate IR spectra is therefore essential to guide such astronomical investigations. Prior to this work, the knowledge of the MIR spectra of $DC_3N$ and $HC_3N$ above 1200 $cm^{-1}$ was sparse and deficient in terms of

measurement precision.

For these reasons, part of the MIR spectra of $DC_3N$ and $HC_3N$ has been re-investigated with a FT-IR spectrometer, which ensures high-resolution across a broad band spectrum. Three fundamentals ($\nu_1$, $\nu_2$, and $\nu_3$) and three hot bands ($\nu_1+\nu_7-\nu_7$, $\nu_2+\nu_7-\nu_7$, and $\nu_3+\nu_7-\nu_7$) have been recorded and analyzed for each species. Owing to the high resolution of the spectrometer employed, an accuracy of about $5 \times 10^{-4}$ cm$^{-1}$ has been achieved in terms of line positions, and the splittings due to the $\ell$-type resonance in $\Pi$ states could be resolved for most of the transitions.

Additional and complementary measurements were performed with a FM-mmW spectrometer, equipped with a furnace that allowed to record pure rotational transitions in highly excited states (with energies above 2000 cm$^{-1}$). The inclusion of rotational lines, whose precision is intrinsically much higher than ro-vibrational data, led to an improved determination of the upper state spectroscopic parameters. If compared to the literature, our constants are more than two orders of magnitude more accurate than those from Ref. [152], and are consistent with the most recent spectroscopic data available for $DC_3N$ [151] and $HC_3N$ [160]. The new set of spectroscopic constants, in combination with the absolute intensity values derived in refs. [156] and [161], can now be used to produce accurate line catalogs for the $\nu_1$, $\nu_2$, and $\nu_3$ band systems of both $DC_3N$ and $HC_3N$. However, a full modeling of the MIR spectra of these species would require the analysis of additional features, i.e., combination, overtone, and hot-bands [152, 156, 161].

## 4.4 Aminoacetonitrile

### 4.4.1 Introduction

The search of amino acids in the ISM is a hot topic in astrochemistry because of the role they might have played in the origin of life on Earth and because they might indicate the presence of extraterrestrial life. Recently, the Hayabusa-2 spacecraft returned samples from the Ryugu asteroid, and their analysis indicated that more than 20 amino acids are present on its surface [164]. This recent discovery further confirms the presence of amino acids in space, these being found in meteorites and comets [165, 166]. Nevertheless, no direct evidence for the presence of amino acids in the gas phase of the ISM has been found so far. This is likely related to the complexity of their rotational spectra [7]. However, they are also easily destroyed in the extreme cosmic conditions. Indeed, ultraviolet (UV) radiation is ubiquitous in the universe and such radiation can photolyze amino acids. Nitriles are proven to be more stable than the corresponding acids under vacuum UV (VUV) radiation [167]. Therefore, nitriles might be considered good proxies for amino acids in the ISM.

Among nitriles, aminoacetonitrile, one of the prebiotic species detected in the ISM, if hydrolyzed, leads to glycine. Aminoacetonitrile can be produced as an intermediate in Strecker synthesis [168], a famous reaction for the formation of amino acids. Over the decades, several chemical pathways have been proposed for the formation of aminoacetonitrile in different astrophysical conditions [169–171]. For example, aminoacetonitrile is suggested to be produced from methanimine ($CH_2NH$) and HCN on the surface of icy grains [169]. Furthermore, aminoacetonitrile is postulated to be formed in Titan aerosol analogs [172]. This further stresses the importance of this molecule and might help in gaining information on the prebiotic chemistry of the early Earth because Titan is considered a good proxy of the primitive stages of our planet. In view of its astrochemical relevance, aminoacetonitrile has been chosen as the subject of an accurate spectroscopic characterization.

Numerous are the previous spectroscopic studies on aminoacetonitrile. MacDonald [173] reported a microwave study, in the 9-35 GHz range, using a Stark modulation spectrometer, with the deuterated species $NHDCH_2CN$ and $ND_2CH_2CN$ also observed. Because of the limited number of observed rotational transitions, only the three rotational constants could be deduced for $NH_2CH_2CN$ and $NHDCH_2CN$, which reduce to only two rotational constants ($B$ and $C$) for $ND_2CH_2CN$. Pickett [174] further investigated the rotational spectra of aminoacetonitrile

and its deuterated isotopologues, thus providing an improved determination of all rotational constants. For the main isotopic species, Bogey [175] further expanded the investigation to the millimeter-wave region (115-352 GHz range), allowing the derivation of the centrifugal distortion constants up to the sextic terms. More than 20 years later, the centrifugal distortion constants up to the sextic terms have been determined for the deuterated isotopologues [176]. Recently, Kolesniková et al [177] recorded and analyzed the pure rotational spectra of the vibrational ground and excited states of aminoacetonitrile. Moreover, several rotational transitions observed in the experiment were attributed to the $^{13}$C isotopologues, thus leading to derivation of their rotational and quartic centrifugal distortion constants.

Owing to the characterization of its rotational spectrum, aminoacetonitrile could be detected in the ISM. Its first detection was toward one protocluster of Sagittarius B2 (Sgr B2) [178], known as Sgr B2(N1), and the derived column density of aminoacetonitrile was found to be $2.8\times10^{16}$ cm$^{-2}$ at temperature of 100 K. In the same year, rotational features of aminoacetonitrile were also identified toward Sgr B2(N2) [179]. In a recent study, the mm/submm-wave data from Degli Esposti *et al.* [180] were combined with high-resolution IR data to determine precise vibrational energies of the three lowest vibrational excited states. This precise spectroscopic investigation in the FIR region led to the first detection of rotational emissions in vibrational excited states towards Sgr B2(N) [181].

Aminoacetonitrile possesses 18 vibrational modes that can be classified – according to the irreducible representations of the $C_s$ point group – into 11 normal modes of $A'$ symmetry and 7 of $A''$ symmetry. At present, the knowledge of the IR spectrum of aminoacetonitrile relies on the works by Bak et al. [182] and Bernstein et al. [183]. The former provided the first tentative assignment of each normal mode from the analysis of a gas-phase spectrum recorded at low resolution with an accuracy of *ca.* 1 cm$^{-1}$, while the latter reported the IR spectrum obtained in a low-temperature matrix isolation experiment. Both studies were guided by low-level harmonic force-field calculations.

Prior to this work, investigations on the high-resolution IR spectra of aminoacetonitrile were limited to the 100-500 cm$^{-1}$ frequency range, with the $v_{11} = 1$, $v_{18} = 1$ and $v_{17} = 1$ states being characterized [181]. In this work, the study has been extended above 500 cm$^{-1}$.

### 4.4.2 Experimental details

The gas-phase IR spectrum of aminoacetonitrile has been recorded between 500 and 1500 $cm^{-1}$ using the Bruker IFS 125 FT interferometer located at the AILES beamline of the SOLEIL synchrotron facility [184]. For this purpose, the spectrometer has been equipped with a White-type cell adjusted to attain an optical path length of 150 m [185, 186], a globar lamp as IR radiation source, a KBr beamsplitter, and a MCT detector [187]. The iris aperture was set to 1.15 mm, thus allowing for a spectral resolution of 0.0015 $cm^{-1}$ in the entire frequency range. Two diamond windows were used to isolate the cell from the interferometer, which was kept evacuated under continuous pumping to limit the absorption of atmospheric water. Aminoacetonitrile has been injected inside the cell at a pressure of 3 $\mu$bar to limit the saturation of the intense band at $\sim$ 790 $cm^{-1}$.

The final spectrum consists of a sum of 112 individual scans, co-added in order to improve its S/N. After the baseline removal, the spectrum was calibrated using the IR bands of two interfering species, namely HCN and $CO_2$. The HCN frequencies were taken from HITRAN2020 database [144], while the band of $CO_2$ around 670 $cm^{-1}$ was taken from Ref. [188]. No apodization functions were applied to the interferograms.

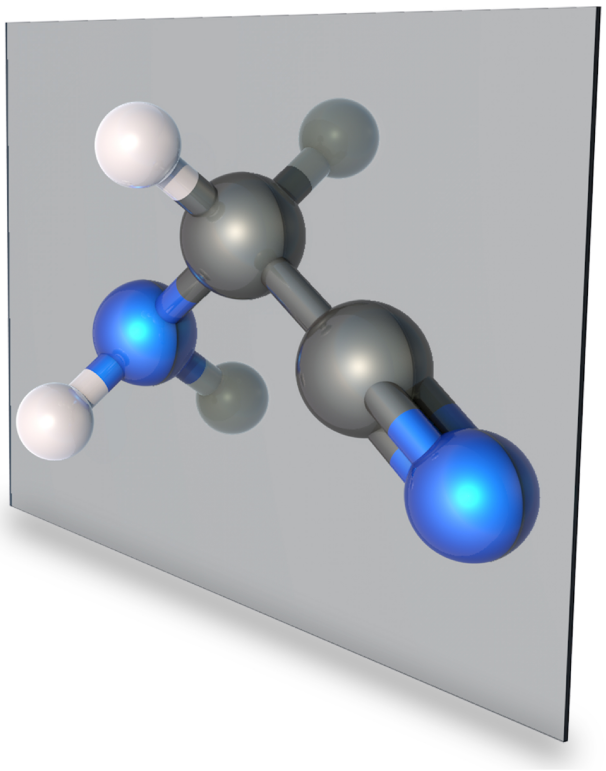

Figure 4.4.1: Molecular structure of aminoacetonitrile

### 4.4.3 Spectral analysis and spectroscopic properties

The global minima of aminoacetonitrile, *trans*-aminoacetonitrile (see Figure 4.4.1), is a near prolate asymmetric rotor. In the present work, the $\nu_{10}$, $\nu_9$, and $\nu_8$ bands have been considered, all belonging to the $A'$ symmetry. Their overview is shown in Figure 4.4.2.

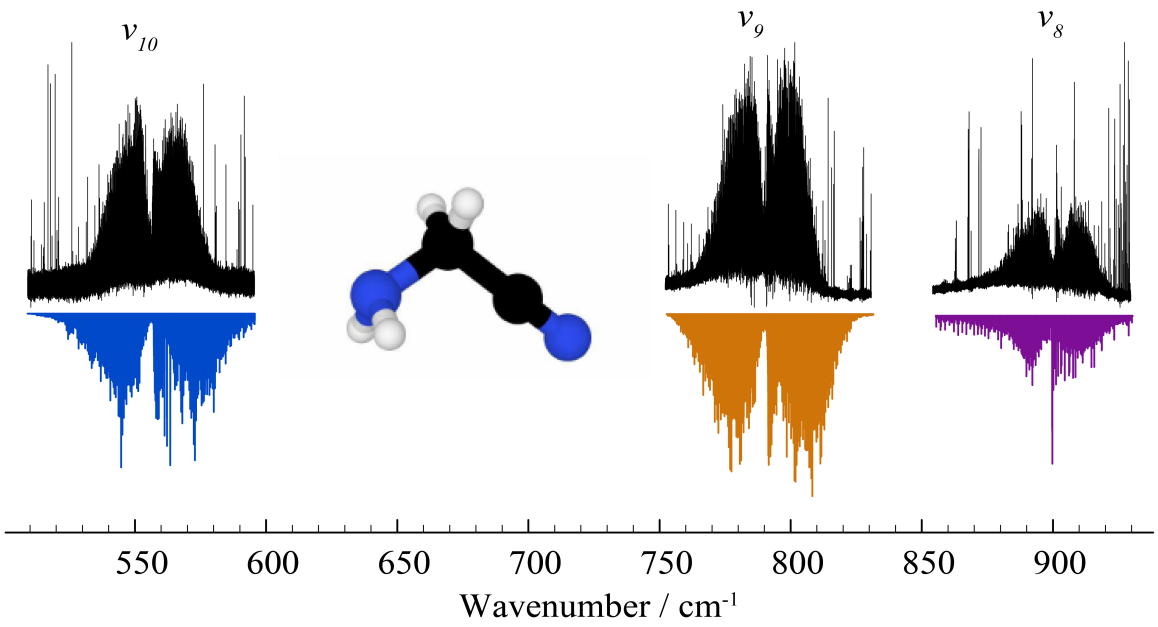


Figure 4.4.2: An overview of the $\nu_8$, $\nu_9$, and $\nu_{10}$ bands in the 3 $\mu$bar spectrum

All these three fundamentals show the typical structure of an $a$-type band, i.e. strong $P$ and $R$ branches with a less pronounced $Q$ branch. To guide the analysis of the rotational structure of each band, spectral simulations have been obtained by combining the ground state spectroscopic constants from Ref. [176] and a set of vibrational excited state parameters obtained from ab initio computations carried out in the lab for band centers and vibration-rotation interaction constants. The spectral simulation has been performed with the `PGOPHER` package [159], while the assignment procedure has been carried out using the graphical tools offered by the LWW program [163]. Moreover, the correctness of the assigned transitions has been checked using the GSCDs method and the MARVEL algorithm [18]. At the end of the assignment procedure, the spectral analysis has been performed using the `SPFIT` subroutine of the `CALPGM` suite of program [162] and employing a $S$-reduced Watson-type Hamiltonian for a semi-rigid nearly-prolate rotor [15].

For the $\nu_{10}$ band (see Figure 4.4.3) – observed in the 534-577 cm$^{-1}$ range – we were able to assign and successfully analyze 1180 distinct transitions, which involve energy levels with $J$

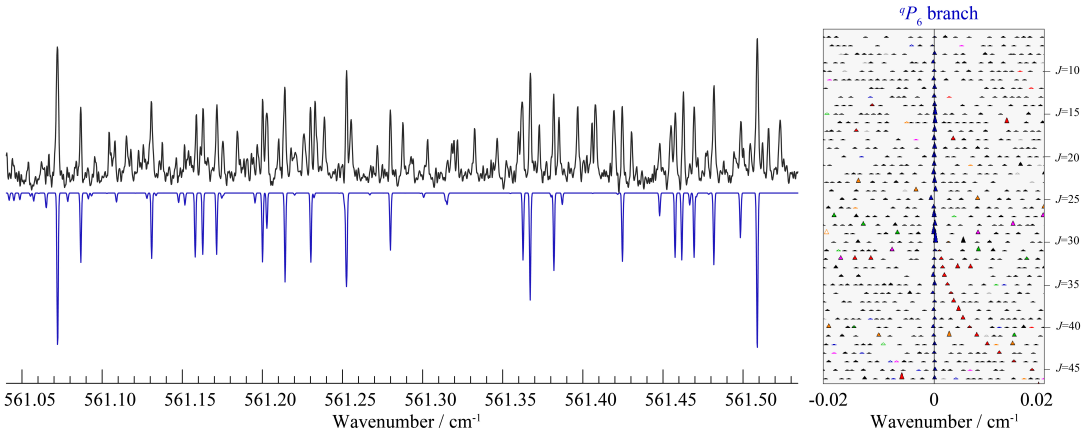


Figure 4.4.3: (Left panel) portion of the $\nu_{10}$ band; (Right panel) Loomis-Wood diagram of the $^qP_6$ branch (blue symbols).

and $K_a$ values up to 75 and 10, respectively. A sub-set of 147 transitions having high values for both quantum numbers (including all the $K_a = 11$ transitions identified) have been discarded from the analysis. The rms error of the final fit is $2.6 \times 10^{-4}$ cm$^{-1}$, which is in line with the expected frequency accuracy. The experimental rotational constants of the $v_{10} = 1$ state have been obtained with good precision and the corresponding vibration-rotation interaction constants $\alpha^A = 382$ MHz, $\alpha^B = -8.6$ MHz, and $\alpha^C = -7.9$ MHz agree very well with those determined in a millimeter-wave study ($\alpha^A = 384$ MHz, $\alpha^B = -8.6$ MHz, and $\alpha^C = -7.9$ MHz) [177]. Moreover, the centrifugal distortion constants of the vibrational excited state are very similar to that of the ground state, which seems to indicate that the $v_{10} = 1$ state is not strongly perturbed by another vibrational state. The band center, predicted at 560 cm$^{-1}$, is found to be at 556.56467(2) cm$^{-1}$. Finally, we estimate that the $b$-type component of this band is at least 10 times weaker than the $a$-type component. Therefore, the unassigned features in this portion of the spectrum (see Figure 4.4.3) belong mainly to hot-bands arising from low-lying energy states, e.g. $v_{11} = 1$, $v_{17} = 1$, $v_{18} = 1$.

The analysis of the $\nu_9$ band (see Figure 4.4.4) was slightly more problematic. In this case, we were able to assign a smaller number of transitions (707 lines in the 775-804 cm$^{-1}$ range, 623 of which were included in the analysis and 84 were discarded), whose maxima values of $J$ and $K_a$ are 47 and 7, respectively. A rms error of $7.1 \times 10^{-4}$ cm$^{-1}$ together with anomalous values obtained for $D_K$ and $d_2$ point out the existence of a moderate perturbation for the $v_9 = 1$ state. This is also supported by the large difference found between the theoretical $\alpha^A$ of 60 MHz and its experimental value of 204 MHz. The interaction occurs most likely with the $v_8 = 1$ and $v_{16} =$

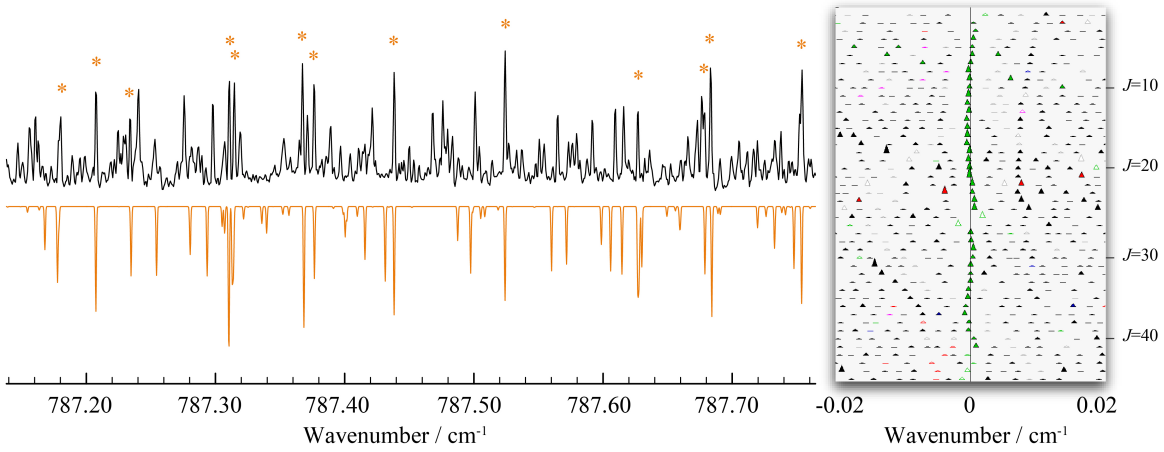


Figure 4.4.4: (Left panel) portion of the $\nu_9$ band. Asterisks indicate the assigned rotational transitions; (Right panel) Loomis-Wood diagram of the ${}^qP_6$ branch (green symbols).

1 states, but many other overtone and combination states can produce accidental degeneracy and thus perturb the $v_9 = 1$ energy levels. Given the difficulty in obtaining a thorough knowledge of the complete manifold of the vibrational excited states of aminoacetonitrile, we limit the present investigation to an effective and partial analysis. Still, the origin of this band has been determined at 790.95908(7) $cm^{-1}$ with good accuracy and compares well with our predicted value of 812 $cm^{-1}$. As a last remark, we note that the tentative assignment made for this state by Kolesnikova et al. [177] is correct, as demonstrated by the similar vibration-rotation interactions constants derived.

The $\nu_8$ band (Figure 4.4.5) was even more difficult to analyze. For this band, only 114 transitions with $J \leq 21$ and $K_a$ values between 5 and 8 could be assigned safely. Attempts to

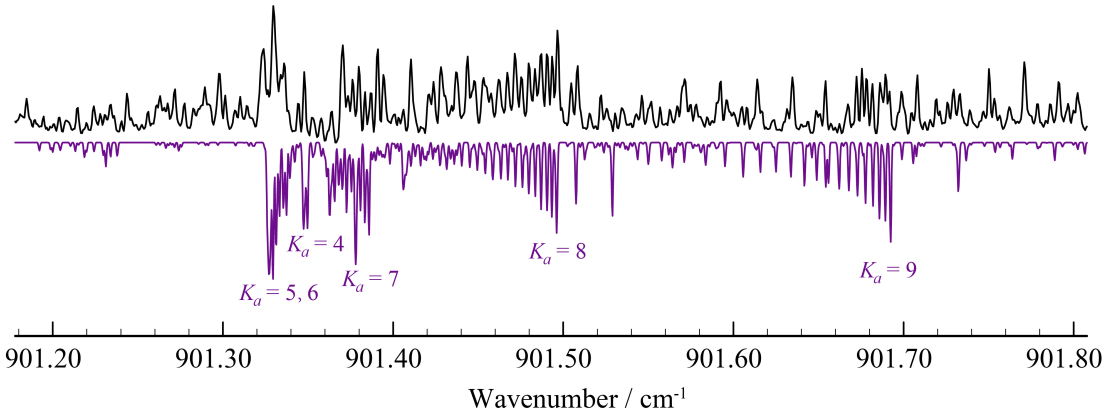


Figure 4.4.5: Portion of the $Q$ branch in the $\nu_8$ vibrational band.

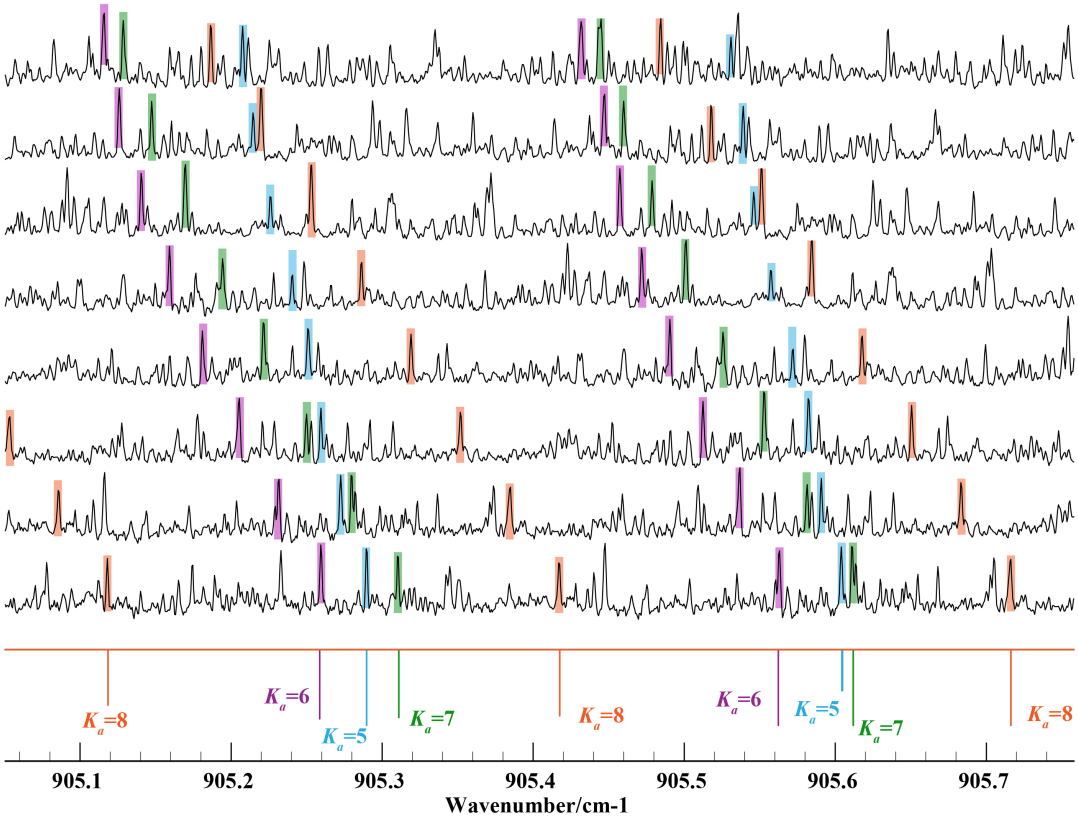


Figure 4.4.6: Portion of the $\nu_8$ band repeatedly shifted in frequency by the $B_0 + C_0$ value, sorted from bottom to top.

derive a consistent set of spectroscopic constants and to search for further transitions – especially those with lower $K_a$ values – were unsuccessful. Figure 4.4.6 shows clearly there is not a consistent tend of the spectral lines except for the four $K_a$ transitions that have been assigned. This implies that the other $K_a$ transitions of the $v_8 = 1$ state are strongly perturbed.

Presumably, the resonances affecting the $v_8 = 1$ state are much more pronounced due to its proximity to the $v_{16} = 1$ state, whose energy levels are unknown at present. In this case, only the band center has been estimated, the value being 901.4(1) $\mathrm{cm}^{-1}$. This is able to reasonably reproduce the shape of the $Q$ branches (see Figure 4.4.5) and is in excellent agreement with our computed value of 899 $\mathrm{cm}^{-1}$.

The spectroscopic constants determined from the analysis of the $\nu_{10}$ and $\nu_9$ bands are listed in Table 4.4.14.

Table 4.4.14: Spectroscopic constants[a] determined from the analysis of the $\nu_{10}$ and $\nu_9$ bands.

| Constant | Unit | $v_{10} = 1$ | $v_9 = 1$ |
|---|---|---|---|
| $E_{\text{vib}}$ | $\text{cm}^{-1}$ | 556.56467(2) | 790.95908(7) |
| $A$ | MHz | 30628.15(4) | 30450.1(2) |
| $B$ | MHz | 4752.461(2) | 4739.10(5) |
| $C$ | MHz | 4302.8854(8) | 4298.94(5) |
| $D_J$ | kHz | 3.0541(3) | 2.517(10) |
| $D_{JK}$ | kHz | -55.89(2) | -54.4(3) |
| $D_K$ | kHz | 748.3(4) | 512.(5) |
| $d_1$ | kHz | -0.6712(2) | -0.72(4) |
| $d_2$ | kHz | -0.02976(6) | -0.09(3) |
| No. of lines | | 1180 | 623 |
| $J, K_a$ max | | 75, 10 | 47, 7 |
| rms $\times 10^3$ | $\text{cm}^{-1}$ | 0.26 | 0.71 |

[a] Numbers in parentheses are standard errors and apply to the last significant digits.

### 4.4.4 Conclusions

The importance of aminoacetonitrile in astrochemistry demands for a deep knowledge of its spectroscopic properties. In this work, we presented the first partial analysis of the three strongest vibrational bands observed between 500 and 1000 $\text{cm}^{-1}$, namely the $\nu_8$, $\nu_9$, and $\nu_{10}$ bands. While the spectral analysis of the $\nu_{10}$ band was satisfactory and the determined spectroscopic constants are in line with those from previous rotational studies [177], the analysis of the $\nu_8$ and $\nu_9$ bands revealed the presence of strong perturbations. Still, the correct assignment of more than 2000 ro-vibrational transitions has been validated using the MARVEL algorithm and should provide a solid base for future investigations.

## 4.5 2-aza-1,3-butadiene

### 4.5.1 Introduction

1,3-butadiene ($CH_2$=CH−CH=$CH_2$, hereafter shortly denoted as butadiene) is a textbook species for understanding conjugation effects and, being the simplest conjugated diene, represents the prototypical reactant for Diels-Alder reactions. Molecules that are isoelectronic to butadiene and share a similar conjugated $\pi$ system form an interesting family of species. Indeed, they allow the investigation of the heteroatom effects in the butadiene skeleton [189]. Limiting ourselves to the second row of the periodic table, there are three singly-substituted species isoelectronic to butadiene: acrolein (O=CH−CH=$CH_2$, also known as propenal), allylimine (NH=CH−CH=$CH_2$, also known as 1-aza-1,3-butadiene), and 2-aza-1,3-butadiene ($CH_2$=N−CH=$CH_2$, hereafter 2-azabutadiene).

These butadiene-like species and butadiene itself are not easy to characterize experimentally. For example, due to the lack of a permanent electric dipole moment, the most stable *trans* form of butadiene does not possess any rotational spectrum. Hence, it is not possible to take the advantage of the inherent accuracy of rotational spectroscopy to determine its molecular structure. In such a case, a rigorous geometrical determination could only be achieved by the analysis of ro-vibrational spectra for several isotopic species [190–194]. As far as *gauche*-butadiene is concerned, its higher energy with the respect to the *trans* form ($\sim$ 12 kJ/mol) together with its small dipole moment value (0.09 D) prevented from establishing unambiguously its non-planarity until recently [195].

Whenever a heteroatom is introduced in the butadiene skeleton, the molecular symmetry reduces noticeably, the resulting asymmetry then generating both an appreciable electric dipole moment and an increased number of active IR modes. For these reasons, acrolein, allylimine, and 2-azabutadiene represent more suitable spectroscopic targets. For example, owing to its large dipole moment values (about 3 D and 2.5 D for the *trans* and *cis* forms, respectively [196]), acrolein has been well characterized from a spectroscopic point of view, as demonstrated by a vast literature on this subject [197–203]. On the other hand, the spectroscopic study of 1- and 2-azabutadiene is quite limited to date [204–208] as both species are unstable and require an efficient and selective production method.

The exhaustive characterization of the high-resolution rotational spectra for these butadiene-like species is also crucial for a different aspect: the study of the chemistry occurring in the ISM.

Despite the harsh conditions of molecular clouds, unsaturated carbon-chains are often abundant (see, for example, the case of TMC-1 [209] or Lupus-1A [210]), thus making butadiene and heterodienes good candidate for astronomical searches. However, because of its centrosymmetric nature, *trans*-butadiene cannot be detected in space through rotational emission and the observation of the more energetic *gauche* form in cold molecular clouds is very unlikely. Abundances of centrosymmetric species, such as molecular nitrogen, cyanogen, or benzene, have been indirectly estimated through the observation of their protonated [211], isomeric [212], or functionalized forms [213]. Analogously, it is here suggested that the presence of interstellar butadiene can be proxied by the detection of its isoelectronic heterodienes. This strategy represents a promising route, given the fact that acrolein has been recently discovered in the ISM [214] and the detection of allylimine is being reported tentatively [215]. However, to the best of our knowledge, astronomical searches of 2-azabutadiene have never been reported. This is probably due to the fact that, in addition to the limited spectral data reported in the literature, no entry for 2-azabutadiene is available in the widely used CDMS database [2, 3] or in the JPL catalog [4]. For this reason, the rotational spectrum of 2-azabutadiene has been further investigated and a refined analysis reported. The experimental work has also been supported by high-level quantum-chemical calculations, which have been obtained by other members of the research group. Even if not part of this thesis, they will be mentioned because they guided the spectral interpretation and provided a good reference set of spectroscopic parameters.

### 4.5.2 Experiment

The sample of 2-azabutadiene has been synthesized in a two-step procedure and directly sent into the cell of the spectrometer as shown in Figure 4.5.1. The rotational spectrum of 2-azabutadiene has been recorded between 225 and 330 GHz by means of the FM-mmW spectrometer described in Chapter 3.

The synthetic reaction reported in the literature for obtaining 2-azabutadiene [216, 217] has been slightly revised and the experimental conditions were optimized with the aim of maximizing the S/N of the rotational spectrum and minimizing the number of possible interfering lines. The production of 2-azabutadiene proceeded in two steps, described in the following, which concerned the synthesis of the precursor (step I) and its transformation in the title molecule (step II).

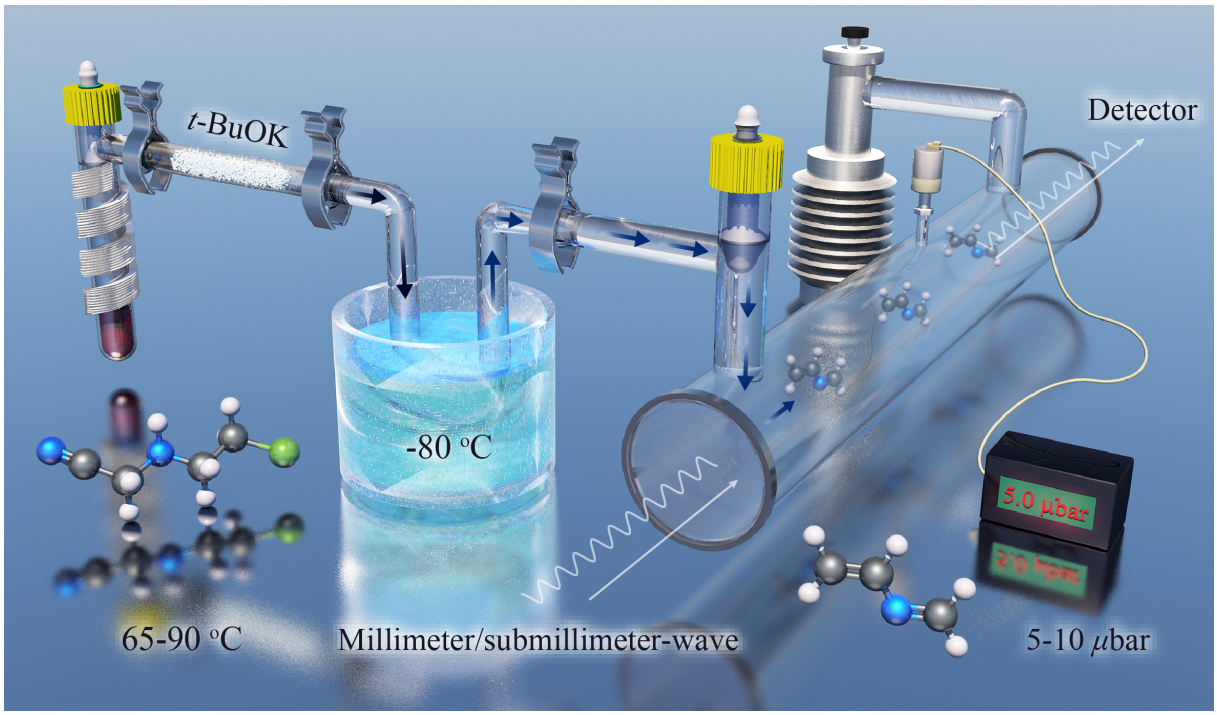


Figure 4.5.1: Graphical representation of the synthesis of gas-phase 2-azabutadiene for the recording of its rotational spectrum with a FM-mmW spectrometer.

**Step I. Synthesis of the precursor**

The precursor is 2-[(2-chloroethyl)amino]acetonitrile, which has been synthesized in a Strecker reaction starting from 2-chloroethylamine hydrochloride (0.1 mol, 11.6 g) and sodium cyanide (0.1 mol, 5 g) in methanol (30 mL) and water (20 mL). The reaction mixture was cooled to 0 °C and formaldehyde (37% in water, 0.1 mol) was added slowly. The solution was allowed to warm up to room temperature and stirred for one hour. Organic compounds were then extracted with dichloromethane (3 times 50 mL). The organic phase was dried over magnesium sulfate and the solvents were removed in vacuo. The crude product obtained in a 90% yield (10.6 g) was sufficiently pure to be used directly in the next step [216,217]. Distillation under vacuum (0.1 mbar) gave the pure product in a 43% yield (5.1 g). 2-chloroethylamine hydrochloride, formaldehyde in water, and sodium cyanide were purchased from Sigma Aldrich and used without further purification.

**Step II. Synthesis of 2-azabutadiene**

2-azabutadiene was synthesized by vaporizing 2-[(2-chloroethyl)amino]acetonitrile (2 g) on potassium tert-butylate (*t*-BuOK, 30 g) introduced in a horizontal tube and filling its lower half. In this reaction, *t*-butanol is also produced and selectively trapped in a U-tube immersed in a

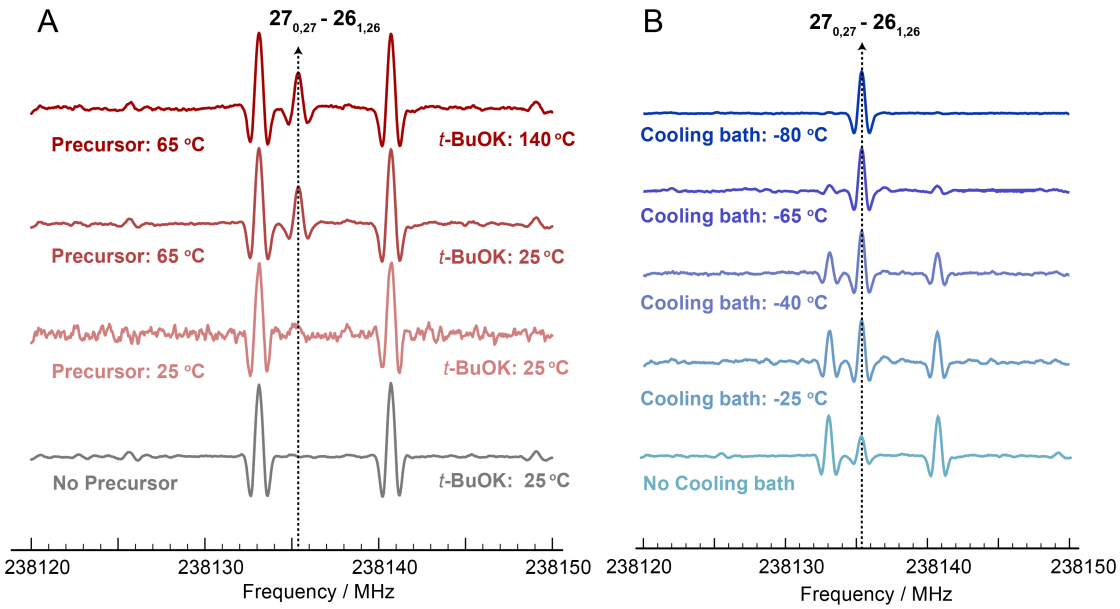


Figure 4.5.2: Portion of the rotational spectra around the $J_{Ka,\,Kc} = 27_{0,\,27} \leftarrow 26_{1,\,26}$ transition of *trans*-2-azabutadiene recorded while optimizing the experimental conditions. The two lines adjacent to the one of interest belong to *t*-BuOH, formed during the reaction. Panel A shows several spectra acquired during the optimization of the reactant temperatures, whereas the spectra shown in Panel B were recorded while keeping 2-[(2-chloroethyl)amino]acetonitrile at 65 °C and *t*-BuOK at room temperature, and varying the temperature of the cooling bath.

cooling bath, while the gaseous flow of almost pure 2-azabutadiene is directly introduced into the spectrometer cell.

The best conditions were optimized by monitoring the spectral S/N for the $J_{Ka,\,Kc} = 27_{0,\,27} \leftarrow 26_{1,\,26}$ transition of *trans*-2-azabutadiene, predicted on the basis of literature data [207]. Figure 4.5.2 shows several spectra recorded upon changing the temperature of (i) the precursor species, (ii) *t*-BuOK, and (iii) the cooling bath. Ultimately, the maximum yield of 2-azabutadiene (and consequently, the best S/N in the spectrum) was achieved by maintaining the precursor compound between 65 °C and 90 °C, with the potassium tert-butylate sample at room temperature, and the cooling bath at -80 °C. The cooling bath was obtained by mixing acetone with liquid nitrogen and allowed for the complete removal of the interfering lines belonging to the *t*-BuOH formed during the reaction.

### 4.5.3 Results

2-azabutadiene exists in two conformations, depending on the value of the C=N−C=C dihedral angle ($\phi$) (see Figure 4.5.3): the most stable planar *trans* form ($\phi = 180°$) and the more

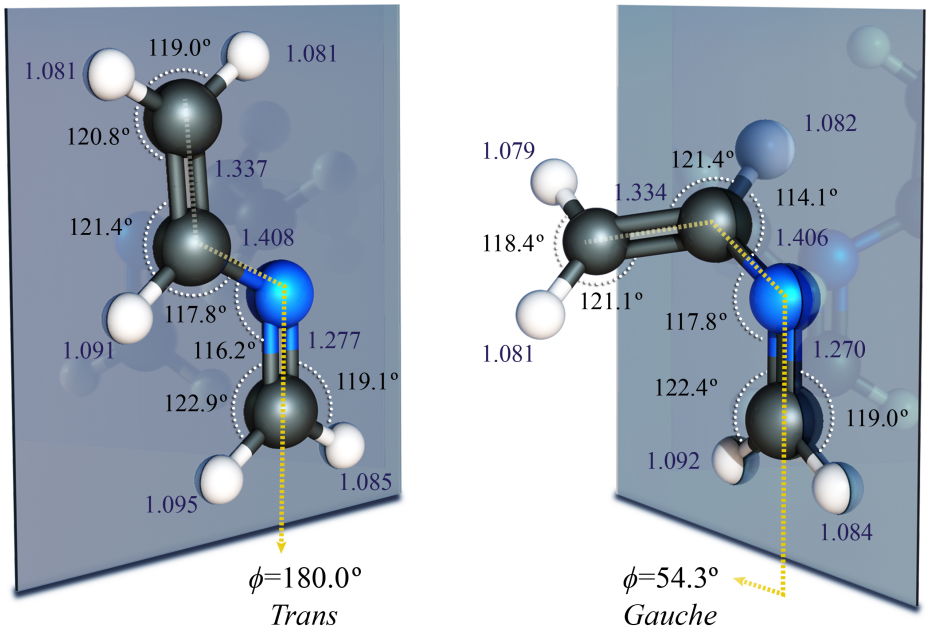


Figure 4.5.3: Molecular structures of *trans*- and *gauche*-2-azabutadiene together with the computed geometrical parameters (bond lengths in Å, angles in degrees).

energetic *gauche* isomer ($\phi = 54°$). In Figure 4.5.3, the structures of these two forms together with accurate geometrical parameters (see Ref. [218]) are also reported. Except for the dihedral angle, most of the bond lengths and angles are similar in the two forms.

At a high computational level, the equilibrium energy difference ($\Delta E^{(gauche-trans)}$) between the two conformers is 6.5 kJ/mol. By incorporating zero-point energy (ZPE) correction, $\Delta E^{(gauche-trans)}$ increases to 7.2 kJ/mol. Based on this energy difference, the population of *gauche*-2-azabutadiene is about 7% of that of the *trans* form at room temperature. Since the computed $(\mu_b^{(gauche)}/\mu_b^{(trans)})^2$ ratio is $\sim 0.7$ (see Table 4.5.15), rotational transitions belonging to *gauche*-2-azabutadiene are expected to be roughly 20 times weaker than those of the *trans* species. Even though the attained S/N of the spectrum is about 150 for *trans*-2-azabutadiene, this is expected to be less than 10 for the *gauche* form. In addition to that, the *trans* species possesses eight vibrational states lying below the energy of *gauche*-2-azabutadiene. Therefore, in conclusion, the identification of the weak spectrum of the *gauche* form was prevented by the huge number of interfering lines and only the *trans* conformer could be experimentally characterized. Nonetheless, for comparison purposes, the computed spectroscopic constants of provided *gauche*-2-azabutadiene are provided in Table 4.5.15.

*Trans*-2-azabutadiene is an asymmetric rotor with a strong nearly-prolate nature ($\kappa = -0.979$). In its principal inertia system, the molecule lies on the $ab$ plane with the $c$-axis perpendicular to

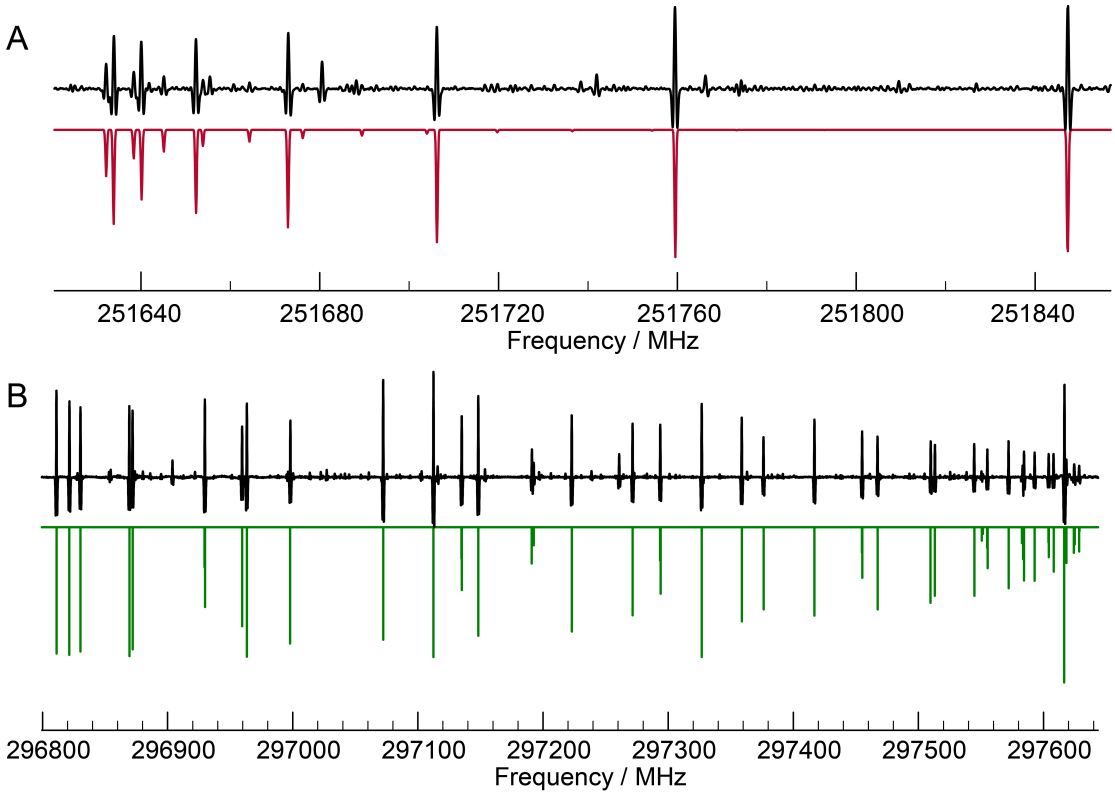


Figure 4.5.4: Portion of the rotational spectrum of 2-azabutadiene (black plot). The red trace depicts $a$-type transitions (Panel A), while the green trace represents $b$-type transitions (Panel B).

it. The experimental dipole moment components are $\mu_a = 0.44(3)$ D and $\mu_b = 1.90(7)$ D [218], with $\mu_c$ being null for symmetry reasons (the point group symmetry is $C_s$).

Exploiting the best experimental conditions, almost 600 new rotational transitions, both of $a$- and $b$-type, were recorded between 225 and 330 GHz (examples are provided in Figure 4.5.4). They probe energy levels with $J$ up to 76 and $K_a$ up to 20, such a difference in the upper limits of $J$ and $K_a$ being ascribable to the relatively large $A$ rotational constant ($\sim$ 47 GHz) with the respect to the much smaller $B$ and $C$ values ($\sim$ 4.4 GHz). Indeed, the population of the rotational energy levels decreases quickly by increasing $K_a$ and slowly by increasing $J$.

The rotational spectrum has been analyzed using a Hamiltonian composed by a purely rotational and a hyperfine term. For the former, the $S$-reduced Watson-type rotational Hamiltonian in $I^r$ representation [15] including the centrifugal distortion up to sextic terms has been used. The latter describes the $^{14}$N-quadrupole interaction. Details on both Hamiltonians are provided in Charpter 2. Our newly observed rotational transitions were combined with previous low-frequency data [207] and analyzed in a weighted least-squares procedure using the `SPFIT`

program [162]. The results are collected in Table 4.5.15. Despite the relatively high $J$ values targeted in this work, the hyperfine structure arising from the quadrupolar $^{14}$N nucleus has been partially resolved for some low $K_a$, $b$-type transitions. Therefore, we were able to determine the $(\chi_{bb} - \chi_{cc})/4$ parameter, whereas the value of $1.5 \times \chi_{aa}$ has been kept fixed to its computed value.

Table 4.5.15: Ground-state spectroscopic parameters of *trans*- and *gauche*-2-azabutadiene ($S$ reduction, $I^r$ representation).

| | | *trans* | | | *gauche* | |
|---|---|---|---|---|---|---|
| Parameter | Unit | Exp.[a] | Theo.[b] | Ref. [207][c] | Theo.[b] | Scaled[d] |
| $A$ | MHz | 47186.0004(7) | 47231.509 | 47186.012(7) | 24021.128 | 23997.983 |
| $B$ | MHz | 4886.5219(1) | 4887.740 | 4886.5223(8) | 6071.991 | 6070.478 |
| $C$ | MHz | 4430.0772(1) | 4430.824 | 4430.0778(8) | 5120.829 | 5119.966 |
| $D_J$ | kHz | 0.97917(8) | 0.960416 | 0.980(3) | 5.42141 | 5.52727 |
| $D_{JK}$ | kHz | −8.0641(7) | −7.38104 | −7.99(9) | −40.8174 | −44.5947 |
| $D_K$ | kHz | 341.95(2) | 309.12 | 341.(1) | 207.669 | 229.722 |
| $d_1$ | kHz | −0.117415(5) | −0.120169 | −0.1173(1) | −1.82008 | −1.77837 |
| $d_2$ | kHz | −0.006949(1) | −0.006235 | −0.00695(2) | −0.19994 | −0.22283 |
| $H_J$ | mHz | 0.29(1) | 0.217 | | −12.7 | −16.97 |
| $H_{JK}$ | mHz | −8.0(2) | −3.856 | | 308.2 | 639.4 |
| $H_{KJ}$ | Hz | −0.267(2) | −0.411 | | −3.736 | −2.431 |
| $H_K$ | Hz | 1.3(1) | 5.75 | | 14.019 | 3.167 |
| $h_1$ | mHz | 0.0691(9) | 0.0786 | | −7.35 | −6.462 |
| $h_2$ | mHz | 0.0104 | 0.0104 | | −1.12 | −1.12 |
| $h_3$ | mHz | 0.0016 | 0.0016 | | −0.0691 | −0.0691 |
| $1.5 \times \chi_{aa}$ | MHz | 1.411 | 1.411 | 0.8(15) | 1.275 | 1.275 |
| $(\chi_{bb} - \chi_{cc})/4$ | MHz | −2.142(7) | −2.13 | −2.1(12) | −0.839 | −0.839 |
| $\lvert\mu_a\rvert$ | D | 0.44(3)[e] | 0.47 | | 0.029 | 0.027 |
| $\lvert\mu_b\rvert$ | D | 1.90(7)[e] | 1.46 | | 1.206 | 1.569 |
| $\lvert\mu_c\rvert$ | D | | | | 0.806 | 0.806 |
| No. data | | 675 | | 82 | | |
| $J_{\max}, K_{\mathrm{a\,max}}$ | | 76, 20 | | 31, 4 | | |
| rms error | kHz | 32.9 | | 31.8 | | |
| $\sigma$ | | 1.09 | | 1.06 | | |

[a] Values in parentheses are one standard deviation and refer to the last digits. Parameters without uncertainties are held fixed at the corresponding computed value.
[b] High-level computed spectroscopic data. For details, see Ref. [218].
[c] Converted from $A$- to $S$-reduction.
[d] Obtained using Equation (4.7). See text for details.
[e] Determined by Stark effect measurements in Ref. [207].

From the inspection of Table 4.5.15, we note that the rms error of the residuals (32.9 kHz) is in line with the estimated accuracy of both our transition frequencies and those reported in literature [207]. The semi-rigid model is appropriate for the description of the rotational energy levels, as demonstrated by the standard deviation of the fit ($\sigma$), which is 1.09. The rotational constants $A$, $B$, and $C$ have been determined with a remarkably good accuracy, the

associated errors being smaller than 1 kHz. Notably, all quartic centrifugal distortion constants have been obtained with an uncertainty smaller than 0.01% and most of the sextic terms could be derived, with the exception of two off-diagonal constants ($h_2$ and $h_3$) that have been kept fixed at the corresponding computed values. The agreement between the experimental and theoretical parameters is very good.

The improvement in the accuracy of our spectroscopic parameters over those derived by Sugie *et al.* [207] is evident (see Table 4.5.15); the uncertainty on rotational and centrifugal distortion constants has been reduced by one and two order of magnitude, respectively. Owing to the higher $J$ and $K_a$ values sampled in our measurements and to the enlarged dataset available, the centrifugal analysis of *trans*-2-azabutadiene has been expanded and now includes distortion terms up to the sextic constants.

Concerning the *gauche* form of 2-azabutadiene, based on the comparison between theory and experiment for the *trans* species, the computational estimates of the spectroscopic parameters should be reliable. They can be further improved by applying an empirical, well-tested, scaling procedure based on the ratio between the computed and experimental constants for the *trans* form:

$$p_{\text{scaled}}^{(\text{gauche})} = p_{\text{theo}}^{(\text{gauche})} \times \left( \frac{p_{\text{exp}}^{(\text{trans})}}{p_{\text{theo}}^{(\text{trans})}} \right) \tag{4.7}$$

where $p^{(\text{X})}$ represents a generic parameters of the X isomer. The scaled parameters are collected in the last column of Table 4.5.15, and their accuracy is expected to be increased by one order of magnitude with respect to computed values.

### 4.5.4 Discussion and Conclusions

Given the similar heavy-atom skeleton and the conjugated $\pi$ system shared by 2-azabutadiene, butadiene, acrolein, and allylimine, it is interesting to qualitatively compare the values of the rotational and centrifugal distortion constants available for each species. This comparison is performed separately for the *trans* and the *cis/gauche* species, the results being reported in Tables 4.5.16 and 4.5.17, respectively. As far as the *trans* species are concerned, the similarity is evident. The order of magnitude and the sign of each constant listed in Table 4.5.16 are the same for all the species considered. This indicates a similar mass distribution (i.e. molecular geometry) and stiffness of the chemical bonds due to the analogy between the conjugated systems.

The case of the *gauche/cis* species is slightly different. Here, the similarity is less pronounced due to two facts. First, the higher energy conformer of acrolein displays a planar *cis* geometry, while both butadiene and 2-azabutadiene possess non-planar *gauche* forms. Second, *gauche*-butadiene exhibits tunneling between two equivalent minima, whereas no large amplitude motion occurs in the heterodienes. That being said, it is likely that the differences observed for the two inversion states of butadiene are due to an unsatisfactory treatment of the Coriolis interaction occurring between the $0^+$ and $0^-$ states. In this framework, the centrifugal distortion constants of acrolein and 2-azabutadiene might be used as a reference to guide the analysis towards a better modelling.

The centrifugal analysis of 2-azabutadiene has another important outcome. The rotational spectrum of the most stable *trans* form can be now predicted with high accuracy in a wide range of frequencies. This represents a key prerequisite for enabling astronomical searches of this species in dense spectral line surveys of molecular-rich objects, where an unambiguous spectroscopic identification typically requires a match within a few tens of kHz.

One isomer of 2-azabutadiene, namely ethyl cyanide, has been observed in high-mass star forming regions with remarkable high abundances [219–222], while another isomer –i.e. allylimine– is being reported as tentatively detected in G+0.693 [215]. These discoveries tell us that molecules showing the same degree of complexity as 2-azabutadiene can be formed efficiently in interstellar conditions, thus making the 2-azabutadiene a good candidate for future detections. Besides giving information about the kinetics and thermodynamics of the $C_3H_5N$ isomeric family, 2-azabutadiene can be used –together with the other heterodienes– to proxy the abundance

Table 4.5.16: Rotational and quartic centrifugal distortion constants of the *trans* species[a]

| Constant | Unit | butadiene[b] | allylimine[c] | | acrolein[d] | 2-azabutadiene |
|---|---|---|---|---|---|---|
| | | | *Trans-anti (Ta)* | *Trans-syn (Ts)* | | |
| $A$ | MHz | 41682.6292(11) | 45773.6451(9) | 43755.656(2) | 47353.7034(20) | 47186.0004(7) |
| $B$ | MHz | 4433.50067(18) | 4560.93131(7) | 4564.54014(7) | 4659.48810(18) | 4886.5219(1) |
| $C$ | MHz | 4008.04876(19) | 4148.24852(6) | 4134.46273(6) | 4242.70127(16) | 4430.0772(1) |
| $D_J$ | kHz | 0.861735(27) | 0.90964(3) | 0.95037(4) | 1.028148(56) | 0.97917(8) |
| $D_{JK}$ | kHz | -7.15724(48) | -7.531(1) | -7.589(1) | -8.70159(74) | -8.0641(7) |
| $D_K$ | kHz | 218.6356(33) | 296.80(3) | 257.29(7) | 360.142(30) | 341.95(2) |
| $d_1$ | kHz | -0.107889(16) | -0.10715(1) | -0.114863(5) | -0.120228(21) | -0.117415(5) |
| $d_2$ | kHz | -0.0056450(72) | -0.005863(2) | -0.006237(3) | -0.0069896(77) | -0.006949(1) |

[a] Values in parentheses are one standard deviation and refer to the last digits. [b] From Ref. [190]. [c] From Ref. [215]. [d] From Ref. [203]. Converted from $A$- to $S$-reduction.

Table 4.5.17: Rotational and quartic centrifugal distortion constants of the *cis* and *gauche* species[a]

| Constant | Unit | butadiene[b] | | acrolein[c] | 2-azabutadiene |
|---|---|---|---|---|---|
| | | $0^+$ state | $0^-$ state | | |
| $A$ | MHz | 21223.0467(18) | 21232.3005(80) | 22831.6513(51) | 24021.128 |
| $B$ | MHz | 5671.39702(56) | 5667.6405(10) | 6241.02408(38) | 6071.991 |
| $C$ | MHz | 4577.35202(47) | 4581.14000(70) | 4902.23005(24) | 5120.829 |
| $D_J$ | kHz | 4.630(34) | 4.630(34) | 4.893610(178) | 5.42141 |
| $D_{JK}$ | kHz | -6.99(24) | 97.67(40) | -27.8640(13) | -40.8174 |
| $D_K$ | kHz | 114.65(32) | 1039.6(76) | 106.63(13) | 207.669 |
| $d_1$ | kHz | -1.2045(112) | -1.932(28) | -1.480975(128) | -1.82008 |
| $d_2$ | kHz | 0.635(41) | -3.57(17) | -0.109707(78) | -0.199939 |

[a] Values in parentheses are one standard deviation and refer to the last digits. [b] From Ref. [195]. [c] From Ref. [203]. Converted from $A$- to $S$-reduction.

of interstellar butadiene or even ethene. While we do not have yet any evidence that this suggestion might work, an indirect support to this idea is provided by the relative abundances of CCH over CN cyclic-hydrocarbon derivatives in TMC-1, which are highly correlated [223]. In Cernicharo *et al.* [223], it has also been suggested that their relative abundances probably reflect the abundance of the CCH and CN radicals. In this respect, we note that 2-azabutadiene can be seen as substituted ethene, where the $H_2CN$ radical is linked to the latter through the N atom.

Finally, Titan's chemistry deserves a note. Organic nitriles and, more generally, N-substituted hydrocarbons are largely present in the nitrogen-rich atmosphere Titan. In this view, the spectroscopic characterization of 2-azabutadiene might turn useful to gain further information on the chemistry occurring in this moon which is considered to resemble the primitive Earth.

## 4.6 Allylimine

### 4.6.1 Introduction

Imines are a series of N-containing molecules playing an important role in the interstellar chemistry because of their prebiotic character. In fact, they represent key intermediates toward the formation of building blocks of amino acids [224, 225]. To date, a number of imines have been observed in the ISM [226–230]. The simplest one, methanimine ($CH_2NH$), was first detected in the giant molecular cloud complex Sgr B2 in 1973 [226]. Ketenimine ($CH_2CNH$) was tentatively detected toward Sgr B2(N) [227], a star-forming region in the Galactic center source, where $E$-cyanomethanimine [228] and ethanimine ($CH_3CH{=}NH$) [229] were also later identified. More recently, $E$- and $Z$-cyanomethanimine (NC$-$CH=NH) [230] as well as propargylimine (HC=CCH=NH) [231] were discovered in the quiescent G+0.693-0.027 molecular cloud, located at the Galactic Center.

One complex imine of potential astrochemical interest that has been poorly characterized in the past is allylimine. The limited spectroscopic investigations are probably due to its short lifetime, even in the gas phase, because of its high reactivity. The rotational spectrum of allylimine was first studied in Ref. [204], where a Stark modulated spectrometer was employed. Shortly after, the spectroscopic study was extended to the IR region at a low resolution [206]. These studied did not provide a sufficient knowledge for guiding the astronomical search of this molecule in the ISM. This is the reason that motivated this work, which reports the high-resolution rotational spectum and precise spectroscopic constants of allylimine.

From a structural point of view, allylimine can be viewed as an iminic moiety (–CH=NH) connected to a vinyl group ($CH_2{=}CH$) by a single C$-$C bond. With respect to the central C$-$C bond, these two moieties can have a *cis* ($C$) or *trans* ($T$) arrangement. Then, for each of them, the iminic H atom can point toward the vinyl group or away from it: in the first case, we have the *syn* (s) orientation, while in the second case, we have the *anti* (a) orientation. By combining these possible arrangements, four geometrical isomers occur: *Ta*, *Ts*, *Ca*, and *Cs*, which are shown in Figure 4.6.1. All isomers but *Cs* have a planar structure. In *Cs*-allylimine, the backbone is titled because of the repulsion between the iminic H and one terminal vinyl H.

Quantum-chemical calculations [215] pointed out that *Ta*-allylimine is the global minimum, with the *Ts* isomer lying about 280 $cm^{-1}$ higher in energy. The *Ca* and *Cs* isomers are instead much more unstable, lying higher in energy by about 1000 $cm^{-1}$ or even more. This is the reason

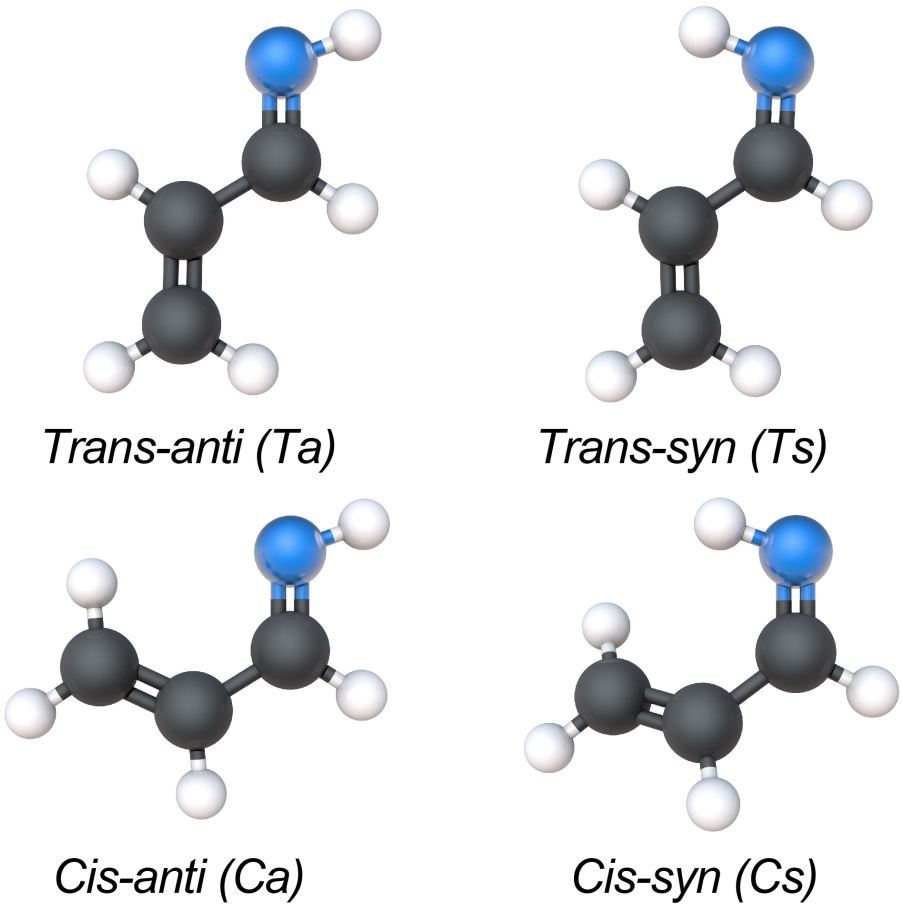


Figure 4.6.1: The four isomers of allylimine.

why only the rotational spectra of *Ta*- and *Ts*-allylimine have been recorded and analyzed in the present work.

### 4.6.2 Experiment

Two different spectrometers were employed to record the rotational spectrum of allylimine: the CASAC (Center for Astrochemical Studies Absorption Cell) spectrometer has been employed in the 80-240 GHz range (the instrument is described in Ref. [232]), while the FM-mmW spectrometer located in Bologna (described in Chapeter 3) has been used for measurements in the 240-310 GHz interval.

In Bologna, allylimine was produced directly inside the absorption cell by heating diallylamine vapors at a temperature of 500 °C. Spectra with a good S/N were obtained already at 100 °C, but a working temperature of 500 °C was chosen in order to have stable experimental

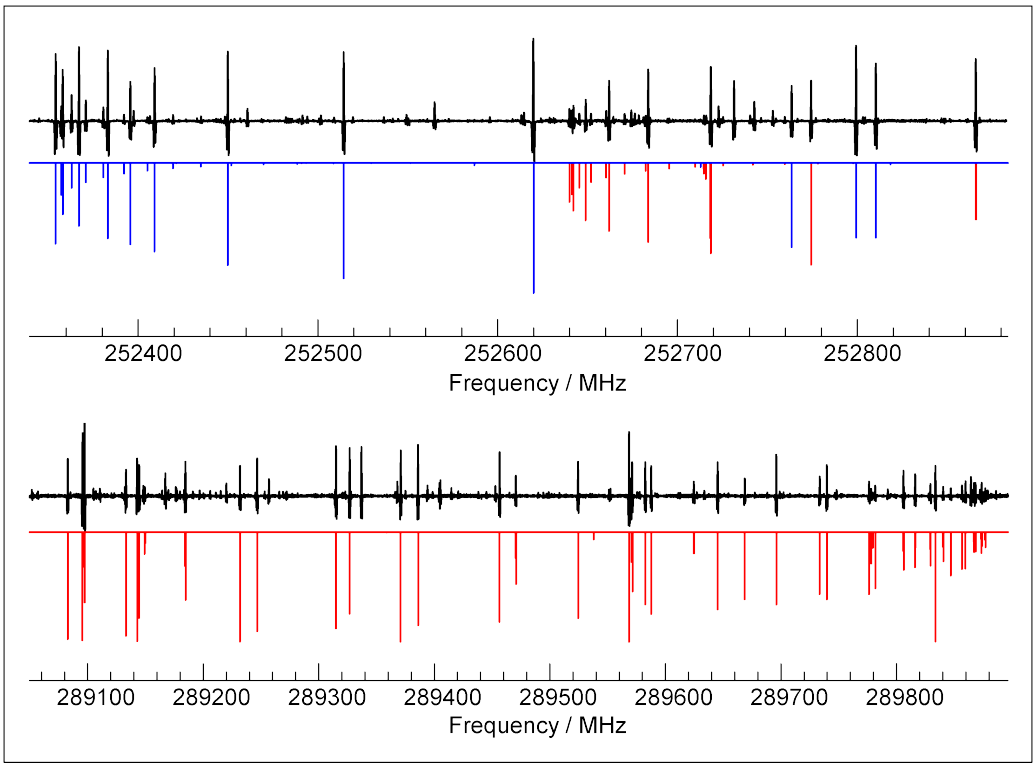


Figure 4.6.2: Portions of the experimental spectrum (in black) showing both $a$- and $b$-type spectral features (blue lines for *Ts*- and red lines for *Ta*-allylimine). Intensity is in arbitrary units.

conditions (the ON/OFF control of the oven causes some oscillation at lower temperatures). In addition, due to the short-life time of allylimine, measurements have been performed in dynamical conditions, with a tenuous flow of gas maintaining a constant pressure of about 4 mTorr (0.5 Pa).

### 4.6.3 Analysis and results

Both *Ta*- and *Ts*-allylimine are nearly-prolate asymmetric top rotors with $\kappa \sim -0.98$. The total dipole moment ($|\boldsymbol{\mu}| \approx 2$ D,) is similar in the two isomers, but very different are the two nonzero components. Based on the computed data (see Table 1 of Ref. [215]), the spectrum of the *Ts* species is dominated by $a$-type transitions, whereas the spectrum of *Ta* has almost equally strong of $a$- and $b$-type transitions. Two portions exhibiting typical $a$- and $b$-type patterns are shown in Figure 4.6.2.

A total of 617 and 470 new rotational transitions have been recorded for *Ta* and *Ts*, respectively. A portion of the rotational spectrum recorded in millimeter-wave range is shown in Figure 4.6.3. The *Ts* spectrum presents strong $R$ branch with $a$-type transitions spaced

by $\Delta\nu \approx (B + C)$. For the *Ta* isomer, instead, $b$-type transitions of $Q$ branch spaced by $\Delta\nu \approx 2A - B - C$ dominate the spectrum, leading to a more complicated pattern. From the relative intensity of two closely spaced *Ts* and *Ta* lines recorded under the same experimental conditions (source power, sample pressure, temperature, and modulation depth), we derived a population ratio of [*Ts*]/[*Ta*] = 3.3 ± 0.8, which is in good agreement with the computed energy difference.

In addition, allylimine contains the $^{14}$N quadrupolar nucleus. The resulting hyperfine structure has been resolved in 293 and 65 transition of *Ts* and *Ta*, respectively. An example is provided by Figure 4.6.4. For transitions with unresolved hyperfine structure, the intensity-averaged calculated frequency was instead compared with the recorded line. The final data sets also included 32 transitions (22 and 10 transitions for *Ta* and *Ts*, respectively) taken from the literature [204].

The analysis has been performed using the same Hamiltonian as in the investigation on 2-azabutadiene. The spectral analyses were carried out using the `CALPGM` program suite [162]. Rotational transitions with the *J* quantum number as high as 52 and 46 have been included for the *Ta* and *Ts* species, respectively, whereas the maximum $K_a$ value reached is 18 and 22, respectively. The spectroscopic constants determined from the fits are collected in Ta-

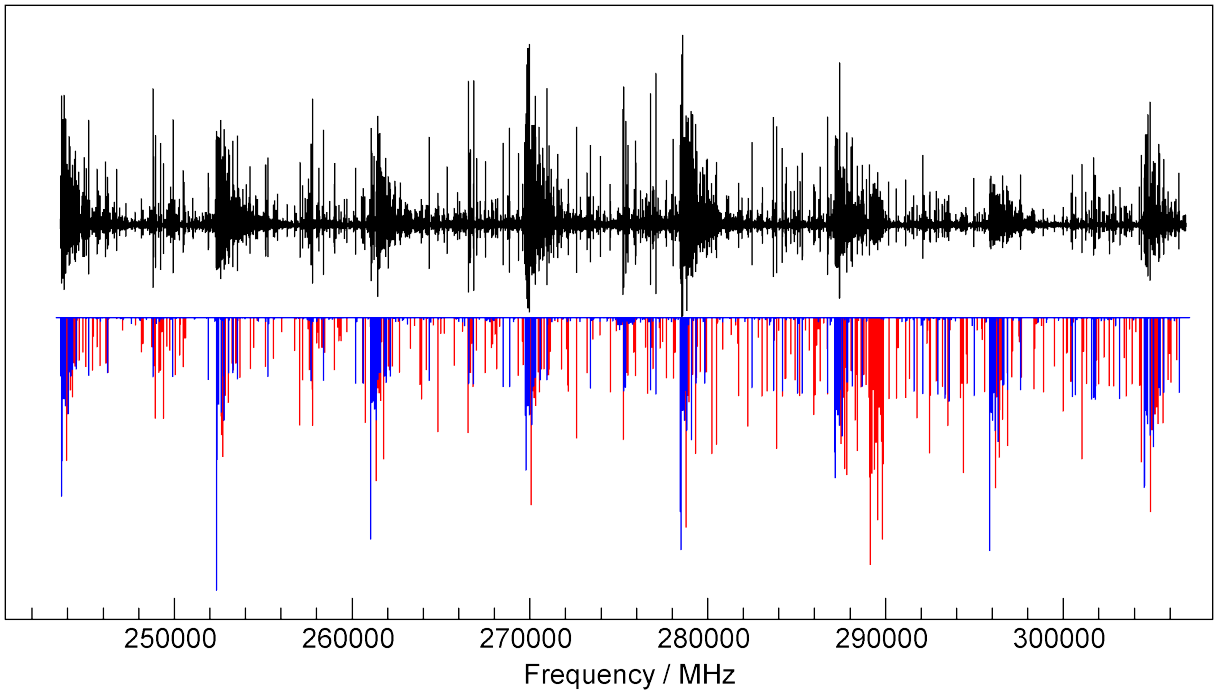


Figure 4.6.3: The portion of the rotational spectra recorded in millimeter-wave range. The black trace is the experimental spectrum, while the blue and red traces present are $Ta$- and $Ts$-allylimine.

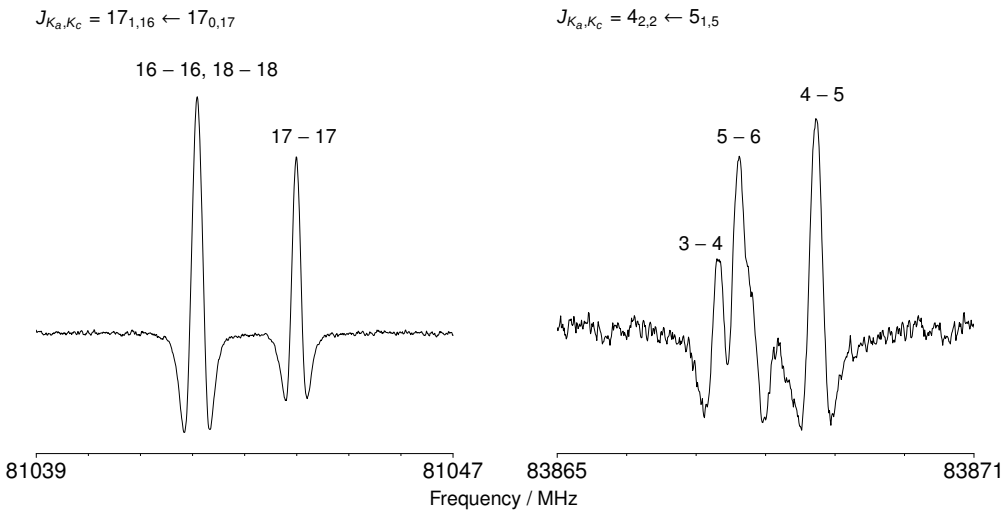


Figure 4.6.4: Recordings of two b-type transitions of *Ta*-allylimine. The nitrogen quadrupole coupling splitting is evident (each hyperfine component is marked with the $F' - F$ label. Left panel: $J_{Ka,Kc} = 5_{1,5} - 4_{0,4}$; right panel: $J_{Ka,Kc} = 5_{2,3} - 6_{1,6}$.

Table 4.6.18: Spectroscopic constants of the *Ta* and *Ts* isomers of allylimine[a].

| | | *Ta*-allylimine | | *Ts*-allylimine | |
|---|---|---|---|---|---|
| constant | unit | experiment | ab initio | experiment | ab initio[b] |
| $A$ | / MHz | 45773.64504(81) | 45797.91440 | 43755.655(17) | 43766.134 |
| $B$ | / MHz | 4560.931313(62) | 4561.224130 | 4564.54014(68) | 4565.77443 |
| $C$ | / MHz | 4148.248522(60) | 4148.336622 | 4134.46273(64) | 4135.28507 |
| $D_J$ | / kHz | 0.909645(28) | 0.9054 | 0.95037(37) | 0.9472 |
| $D_{JK}$ | / kHz | −7.53100(98) | −7.5154 | −7.589(12) | −7.4241 |
| $D_K$ | / kHz | 296.804(27) | 286.9488 | 257.29(74) | 243.0085 |
| $d_1$ | / kHz | −0.107148(13) | −0.1094 | −0.114863(46) | −0.1182 |
| $d_2$ | / kHz | −0.0058627(15) | −0.0055 | −0.006237(31) | −0.0059 |
| $H_J$ | / mHz | 0.21719[b] | 0.21719 | 0.22243[b] | 0.22243 |
| $H_{JK}$ | / Hz | −0.00604(44) | −0.00306 | −0.00723(54) | −0.0034 |
| $H_{KJ}$ | / Hz | −0.2997(20) | −0.3809 | −0.196(15) | −0.299 |
| $H_K$ | / Hz | 2.89(24) | 4.55 | 3.61474[b] | 3.61474 |
| $h_1$ | / mHz | 0.0667(43) | 0.0762 | 0.08093[b] | 0.08093 |
| $h_2$ | / mHz | 0.01095[b] | 0.01095 | 0.01087[b] | 0.01087 |
| $h_3$ | / mHz | 0.00157[b] | 0.00157 | 0.00152[b] | 0.00152 |
| $\chi_{aa}$ | / MHz | 0.751(23) | 0.731 | −2.963(17) | −2.974 |
| $\chi_{bb} - \chi_{cc}$ | / MHz | −6.985(19) | −6.906 | −3.267(10) | −3.263 |
| No. of lines | | 617 | | 470 | |
| $\sigma_{\text{rms}}$ | | 1.03 | | 1.00 | |

[a] Numbers in parentheses represent $1\sigma$ standard deviation in unit of the last digit. [b] Fixed at the corresponding computed value. For details on computations, the reader is referred to Ref. [215].

ble 4.6.18, together with the corresponding computed values (for the latter, details can be found in Ref. [215]). For *Ta*- and *Ts*-allylimine, $\sigma_{rms}$ values of 1.03 and 1.00 have been obtained, thus indicating that the data sets were reproduced within experimental uncertainties on average. The uncertainties on the rotational constants $A$, $B$, and $C$ have been reduced by three orders of magnitude (a factor of $\sim 350$ for the *Ts* isomer) compared to what was published before [204]. In addition, for the first time, a complete set of quartic centrifugal distortion constants (with a precision of $\sim 0.1\%$) and four sextic terms have been determined.

### 4.6.4 Conclusion

The extensive spectroscopic characterization of allyllimine carried out for *Ta* and *Ts*-allyllimine provided an extremely precise set of rotational constants, a complete set of quartic, and some sextic centrifugal distortion constants. These parameters were used to generate an accurate line catalog that was employed for the astronomical searches of allylimine in the G+0.693-0.027 molecular cloud, located at the Galactic Center. A tentative detection for both allylimine isomers has been reported in Ref. [215].

# Chapter 5

# Conclusion

More than 270 molecules have been identified in extraterrestrial environments so far [2, 3, 6], most of them discovered thanks to the detection of their rotational emissions. Molecules of astrochemical relevance might be difficult to produce and study in the laboratory because of the great difference between the interstellar conditions and those typical of Earth. For instance, radicals, ions, and unstable unsaturated organic molecules survive long enough to be detected because of the extremely low density of the interstellar medium, which is thus devoided of collisions. The spectroscopic characterization of these molecules is thus particularly challenging and has been the main goal of my PhD work.

The spectroscopic characterization of selected molecules of astronomical significance, ranging from linear to asymmetric-top rotors, is presented in this thesis. The purpose of these studies is to determine the rotational or ro-vibrational spectroscopic parameters of these species in order to support their astronomical observation. From a spectroscopic point of view, the rotational spectra can be very complicated because of various reasons, ranging from resonances, to hyperfine interactions, to difficulties in their production.

In the last three years, my work was mainly focused on the investigation of the rotational and ro-vibrational spectroscopy of molecules of astronomical significance. Several of these molecules are well known interstellar molecules, such as HDS and $H_2CO$, for which a large amount of spectroscopic data has been published. For them, a detailed MARVEL analysis of the rotational and ro-vibrational energy levels have been performed. This approach allowed us to derive energy levels and the corresponding uncertainties from the inversion of different rotational and ro-vibrational transitions through a weighted least-squares procedure. Literature data have also been combined with our laboratory Lamb-dip measurements, thus obtaining the

most detailed spectral networks of HDS and $H_2CO$ to date.

In general, the acquisition and analysis of spectral data of a molecule in the mm/submm-wave regions play a crucial role for the determination of accurate centrifugal distortion constants, which are essential for predicting the position of rotational transitions, which in turn can be used in astronomical searches. I extended the rotational spectra of $H_2C{=}CH{-}CH{=}NH$ and $H_2C{=}CH{-}N{=}CH_2$ to the millimeter-wave range, with the overall result of obtaining very accurate spectroscopic parameters. In addition to being possible interstellar candidates, both of these two molecules can be considered as good proxies for deriving the abundance of symmetric butadiene. Based on our study, emissions due to two isomers of allylimine were tentatively detected towards the G+0.693 molecular cloud.

Moving to infrared spectroscopy, in addition to the characterization of the Earth atmosphere, high-resolution infrared spectroscopy is of a great importance for the exploration of numerous interstellar sources, such as planet atmospheres, comets, protoplanetary disks, and so on. In this framework, I have investigated the high-resolution infrared spectra of molecules of interstellar relevance: $DC_3N$ / $HC_3N$ and aminoacetonitrile. $HC_3N$ and $DC_3N$ emissions have been widely exploited for probing deuterium fractionation (deuterium enrichment) in star-forming regions. $HC_3N$ is not only an abundant interstellar species, but it has also been observed in the atmosphere of Titan, where the presence of aminoacetonitrile is postulated. Since this Saturn's moon is thought to be a good proxy of the primitive Earth and in view of the powerful JWST telescope, the ro-vibrational transitions of $HC_3N$ and aminoacetonitrile can be considered important features to be searched in the atmospheres of exoplanets.

# Bibliography


[1] S. Yamamoto, ed., *Introduction to Astrochemistry (Chemical Evolution from Interstellar Clouds to Star and Planet Formation)*. Springer, 2017.

[2] C. P. Endres, S. Schlemmer, P. Schilke, J. Stutzki, and H. S. Müller, "The Cologne Database for Molecular Spectroscopy, CDMS, in the Virtual Atomic and Molecular Data Centre, VAMDC," *J. Mol. Spectrosc.*, vol. 327, pp. 95–104, 2016.

[3] "Cologne Database for Molecular Spectroscopy (CDMS)." https://cdms.astro.uni-koeln.de/.

[4] "Jet Propulsion Laboratory (JPL) catalog." https://spec.jpl.nasa.gov/.

[5] B. A. McGuire, "2021 census of interstellar, circumstellar, extragalactic, protoplanetary disk, and exoplanetary molecules," *Astrophys. J. Suppl. Ser.*, vol. 259, no. 2, p. 30, 2022.

[6] D. Woon, "List of interstellar molecules on the Astrochymist." http://www.astrochymist.org/.

[7] B. A. McGuire, "2018 census of interstellar, circumstellar, extragalactic, protoplanetary disk, and exoplanetary molecules," *Astrophys. J. Suppl. Ser.*, vol. 239, no. 2, p. 17, 2018.

[8] A. Wootten and A. R. Thompson, "The Atacama Large Millimeter/submillimeter Array," *Proceedings of the IEEE*, vol. 97, no. 8, pp. 1463–1471, 2009.

[9] F. Tercero, J. López-Pérez, J. Gallego, F. Beltrán, O. García, M. Patino-Esteban, I. López-Fernández, G. Gómez-Molina, M. Diez, P. García-Carreño, *et al.*, "Yebes 40 m radio telescope and the broad band NANOCOSMOS receivers at 7 mm and 3 mm for line surveys," *Astron. Astrophys.*, vol. 645, p. A37, 2021.

[10] W. Gordy and R. L. Cook, *Microwave molecular spectra*. Wiley New York, 3rd ed., 1984.

[11] K. Narahari Rao and G. Herzberg, *Molecular spectroscopy: modern research. Vol. II.* Academic New York, 1976.

[12] D. Papousek and M. R. Aliev, *Molecular vibrational-rotational spectra*. Elsevier New York, 1982.

[13] E. B. Wilson, J. C. Decius, and P. C. Cross, *Molecular vibrations: The theory of infrared and Raman vibrational spectra*. Courier Corporation, 1980.

[14] C. Puzzarini, J. F. Stanton, and J. Gauss, "Quantum-chemical calculation of spectroscopic parameters for rotational spectroscopy," *Int. Rev. Phys. Chem.*, vol. 29, no. 2, pp. 273–367, 2010.

[15] J. K. Watson, "Aspects of quartic and sextic centrifugal effects on rotational energy levels," *Vibrational spectra and structure*, vol. 6, pp. 1–89, 1977.

[16] H. M. Pickett, "Vibration—rotation interactions and the choice of rotating axes for polyatomic molecules," *J. Chem. Phys.*, vol. 56, no. 4, pp. 1715–1723, 1972.

[17] A. G. Császár, G. Czakó, T. Furtenbacher, and E. Mátyus, "An active database approach to complete rotational–vibrational spectra of small molecules," *Ann. Rep. Comput. Chem.*, vol. 3, pp. 155–176, 2007.

[18] T. Furtenbacher, A. G. Császár, and J. Tennyson, "MARVEL: Measured Active Rotational–Vibrational Energy Levels," *J. Mol. Spectrosc.*, vol. 245, no. 2, pp. 115–125, 2007.

[19] J. Tennyson, P. F. Bernath, L. R. Brown, A. Campargue, M. R. Carleer, A. G. Császár, R. R. Gamache, J. T. Hodges, A. Jenouvrier, O. V. Naumenko, *et al.*, "IUPAC critical evaluation of the rotational–vibrational spectra of water vapor. Part I—Energy levels and transition wavenumbers for $H_2{}^{17}O$ and $H_2{}^{18}O$," *J. Quant. Spectrosc. Rad. Transf.*, vol. 110, no. 9-10, pp. 573–596, 2009.

[20] C. Ceccarelli, L. Loinard, A. Castets, A. Tielens, E. Caux, B. Lefloch, and C. Vastel, "Extended $D_2CO$ emission: The smoking gun of grain surface-chemistry," *Astron. Astrophys.*, vol. 372, no. 3, pp. 998–1004, 2001.

[21] P. Schilke, D. Benford, T. Hunter, D. Lis, and T. Phillips, "A line survey of Orion-KL from 607 to 725 GHz," *Astrophys. J. Suppl. Ser.*, vol. 132, no. 2, p. 281, 2001.

[22] M. Womack, S. Stern, and M. Festou, "Millimeter-wavelength spectroscopy of CO, HCN, $H_2CO$, and $CH_3OH$ in C/1996 B2 (Hyakutake)," *Planet. Space Sci.*, vol. 45, no. 6, pp. 711–715, 1997.

[23] D. Downes and T. Wilson, "Formaldehyde line emission at 4.8 GHz near NGC 7538," *Astrophys. J.*, vol. 191, p. L77, 1974.

[24] W. A. Baan, R. Güsten, and A. D. Haschick, "Formaldehyde absorption and maser emisson in galaxies," *Astrophys. J.*, vol. 305, pp. 830–836, 1986.

[25] O. Korablev, M. Ackerman, V. Krasnopolsky, V. Moroz, C. Muller, A. Rodin, and S. K. Atreya, "Tentative identification of formaldehyde in the Martian atmosphere," *Planet. Space Sci.*, vol. 41, no. 6, pp. 441–451, 1993.

[26] J. Forster, W. Goss, T. Wilson, D. Downes, and H. Dickel, "A formaldehyde maser in NGC 7538," *Astron. Astrophys.*, vol. 84, pp. L1–L3, 1980.

[27] I. M. Hoffman, W. Goss, and P. Palmer, "The formaldehyde masers in Sgr B2: very long baseline array and very large array observations," *Astrophys. J.*, vol. 654, no. 2, p. 971, 2007.

[28] J.-Z. Wang, Z.-Y. Zhang, and Y. Gao, "High resolution observations of the 6 cm $H_2CO$ maser in NGC 6240," *Res. Astron. Astrophys.*, vol. 13, no. 3, p. 270, 2013.

[29] S. Y. Parfenov and A. Sobolev, "On the class II methanol maser periodic variability due to the rotating spiral shocks in the gaps of discs around young binary stars," *Mon. Not. R. Astron. Soc.*, vol. 444, no. 1, pp. 620–628, 2014.

[30] J. T. van Scheltinga, M. R. Hogerheijde, L. I. Cleeves, R. A. Loomis, C. Walsh, K. I. Öberg, E. A. Bergin, J. B. Bergner, G. A. Blake, J. K. Calahan, *et al.*, "The TW Hya Rosetta stone project. II. Spatially resolved emission of formaldehyde hints at low-temperature gas-phase formation," *Astrophys. J.*, vol. 906, no. 2, p. 111, 2021.

[31] P. Theulé, A. Callegari, T. R. Rizzo, and J. S. Muenter, "Fluorescence detected microwave Stark effect measurements in excited vibrational states of $H_2CO$," *J. Chem. Phys.*, vol. 119, pp. 8910–8915, 2003.

[32] S. Nadler, D. C. Reuter, S. J. Daunt, and J. W. C. Johns, "The $\nu_3$, $\nu_4$ and $\nu_6$ bands of formaldehyde: a spectral catalog from 900 to 1580 $cm^{-1}$," NASA technical memorandum, NASA, 1988.

[33] R. J. Bouwens, J. A. Hammerschmidt, M. M. Grzeskowiak, T. A. Stegink, P. M. Yorba, and W. F. Polik, "Pure vibrational spectroscopy of $S_0$ formaldehyde by dispersed fluorescence," *J. Chem. Phys.*, vol. 104, pp. 460–479, 1996.

[34] H. Barry, L. Corner, G. Hancock, R. Peverall, and G. A. D. Ritchie, "Cross sections in the $2\nu_5$ band of formaldehyde studied by cavity enhanced absorption spectroscopy near 1.76 $\mu$m," *Phys. Chem. Chem. Phys.*, vol. 4, pp. 445–450, 2002.

[35] S. Brünken, H. S. P. Müller, F. Lewen, and G. Winnewisser, "High accuracy measurements on the ground state rotational spectrum of formaldehyde ($H_2CO$) up to 2 THz," *Phys. Chem. Chem. Phys.*, vol. 5, pp. 1515–1518, 2003.

[36] A. Perrin, F. Keller, and J. M. Flaud, "New analysis of the $\nu_2$, $\nu_3$, $\nu_4$, and $\nu_6$ bands of formaldehyde, $H_2{}^{12}C^{16}O$ line positions and intensities in the 5–10 $\mu$m spectral region," *J. Mol. Spectrosc.*, vol. 221, pp. 192–198, 2003.

[37] M. Staak, E. W. Gash, D. S. Venables, and A. A. Ruth, "The rotationally-resolved absorption spectrum of formaldehyde from 6547 to 6804 $cm^{-1}$," *J. Mol. Spectrosc.*, vol. 229, pp. 115–121, 2005.

[38] J. M. Flaud, W. J. Lafferty, R. L. Sams, and S. W. Sharpe, "High resolution spectroscopy of $H_2{}^{12}C^{16}O$ in the 1.9 to 2.56 $\mu$m spectral range," *Mol. Phys.*, vol. 104, pp. 1891–1903, 2006.

[39] A. Perrin, A. Valentin, and L. Daumont, "New analysis of the $2\nu_4$, $\nu_4+\nu_6$, $2\nu_6$, $\nu_3+\nu_4$, $\nu_3+\nu_6$, $\nu_1$, $\nu_5$, $\nu_2+\nu_4$, $2\nu_3$, $\nu_2+\nu_6$ and $\nu_2+\nu_3$ bands of formaldehyde $H_2{}^{12}C^{16}O$: line positions and intensities in the 3.5 $\mu$m spectral region," *J. Mol. Struct.*, vol. 780-781, pp. 28–44, 2006.

[40] R. Perez, J. M. Brown, Y. Utkin, J. Han, and R. F. Curl, "Observation of hot bands in the infrared spectrum of $H_2CO$," *J. Mol. Spectrosc.*, vol. 236, pp. 151–157, 2006.

[41] F. K. Tchana, A. Perrin, and N. Lacome, "New analysis of the $\nu_2$ band of formaldehyde ($H_2{}^{12}C^{16}O$): line positions for the $\nu_2$, $\nu_3$, $\nu_4$ and $\nu_6$ interacting bands," *J. Mol. Spectrosc.*, vol. 245, pp. 141–144, 2007.

[42] W. Zhao, X. Gao, L. Deng, T. Huang, T. Wu, and W. Zhang, "Absorption spectroscopy of formaldehyde at 1.573 $\mu$m," *J. Quant. Spectrosc. Rad. Transf.*, vol. 107, pp. 331–339, 2007.

[43] S. Saha, H. Barry, G. Hancock, G. A. D. Ritchie, and C. M. Western, "Rotational analysis of the $2\nu_5$ band of formaldehyde," *Mol. Phys.*, vol. 105, pp. 797–805, 2007.

[44] L. Margulés, A. Perrin, R. Janeckova, S. Bailleux, C. P. Endres, T. F. Giesen, and S. Schlemmer, "Rotational transitions within the $2^1$, $3^1$, $4^1$, and $6^1$ states of formaldehyde $H_2{}^{12}C^{16}O$," *Can. J. Phys.*, vol. 87, pp. 425–435, 2009.

[45] A. Perrin, D. Jacquemart, F. K. Tchana, and N. Lacome, "Absolute line intensities measurements and calculations for the 5.7 and 3.6 $\mu$m bands of formaldehyde," *J. Quant. Spectrosc. Rad. Transf.*, vol. 110, pp. 700–716, 2009.

[46] J. Cihelka, I. Matulková, and S. Civiš, "Laser diode photoacoustic and FTIR laser spectroscopy of formaldehyde in the 2.3 $\mu$m and 3.5 $\mu$m spectral range," *J. Mol. Spectrosc.*, vol. 256, pp. 68–74, 2009.

[47] D. Jacquemart, A. Laraia, F. K. Tchana, R. R. Gamache, A. Perrin, and N. Lacome, "Formaldehyde around 3.5 and 5.7 $\mu$m: measurement and calculation of broadening coefficients," *J. Quant. Spectrosc. Rad. Transf.*, vol. 111, pp. 1209–1222, 2010.

[48] S. Eliet, A. Cuisset, M. Guinet, F. Hindle, G. Mouret, R. Bocquet, and J. Demaison, "Rotational spectrum of formaldehyde reinvestigated using a photomixing THz synthesizer," *J. Mol. Spectrosc.*, vol. 279, pp. 12–15, 2012.

[49] A. A. Ruth, U. Heitmann, E. Heinecke, and C. Fittschen, "The rotationally-resolved absorption spectrum of formaldehyde from 6547 to 7051 $cm^{-1}$," *Z. Phys. Chem.*, vol. 229, pp. 1609–1624, 2015.

[50] H. S. P. Müller and F. Lewen, "Submillimeter spectroscopy of $H_2C^{17}O$ and a revisit of the rotational spectra of $H_2C^{18}O$ and $H_2C^{16}O$," *J. Mol. Spectrosc.*, vol. 331, pp. 28–33, 2017.

[51] T. L. Tan, R. Ádawiah, and L. L. Ng, "The $2\nu_2$ bands of $H_2^{12}CO$ and $H_2^{13}CO$ by high-resolution FTIR spectroscopy," *J. Mol. Spectrosc.*, vol. 340, pp. 16–20, 2017.

[52] T. Oka, "Microwave spectrum of formaldehyde. II. Molecular structure in the ground state," *J. Phys. Soc. Jpn.*, vol. 15, pp. 2274–2279, 1960.

[53] T. Shigenari, S. Kobayashi, and H. Takuma, "(6.3) Rotational spectrum of $H_2CO$ by a radiofrequency beam-type maser," *J. Phys. Soc. Jpn.*, vol. 18, pp. 312–313, 1963.

[54] A. F. Krupnov, L. I. Gershtein, V. G. Shustrov, and V. V. Polyakov, "Submillimeter microwave spectroscopy of formaldehyde," *Opt. Spectrosc.*, vol. 28, p. 257, 1970.

[55] K. D. Tucker, G. R. Tomasevich, and P. Thaddeus, "Laboratory measurement of the 2-centimeter, $2_{11}-2_{12}$, transition of normal formaldehyde and its carbon-13 and oxygen-18 species," *Astrophys. J.*, vol. 174, pp. 463–466, 1972.

[56] K. D. Tucker, G. R. Tomasevich, and P. Thaddeus, "Laboratory measurement of the 6 centimeter formaldehyde transitions," *Astrophys. J.*, vol. 169, pp. 429–440, 1971.

[57] J.-C. Chardon and J.-J. Miller, "Spectroscopie résonance électrique des jets moléculaires: formes des raies de résonance en présence d'effet Doppler," *Can. J. Phys.*, vol. 59, pp. 378–386, 1981.

[58] J. C. Chardon and D. Guichon, "Structure hyperfine du spectre basse fréquence de $H_2CO$," *J. Phys. (Paris)*, vol. 34, pp. 791–802, 1973.

[59] M. Takami, "$K$-type doubling lines of $H_2CO$ and HCOOH in the HF region," *J. Phys. Soc. Jpn.*, vol. 24, pp. 372–376, 1968.

[60] J. C. Chardon and D. Guichon, "Spectre radiofréquence de $H_2CO$ dans des états vibrationnels excités," *J. Phys. (Paris)*, vol. 38, no. 2, pp. 113–120, 1977.

[61] R. Bocquet, J. Demaison, L. Poteau, M. Liedtke, S. Belov, K. M. T. Yamada, G. Winnewisser, C. Gerke, J. Gripp, and T. Köhler, "The ground state rotational spectrum of formaldehyde," *J. Mol. Spectrosc.*, vol. 177, pp. 154–159, 1996.

[62] H. Takuma, K. M. Evenson, and T. Shigenari, "Zeeman effect and magnetic hyperfine structure in low frequency transitions of $H_2CO$," *J. Phys. Soc. Jpn.*, vol. 21, pp. 1622–1623, 1966.

[63] B. Fabricant, D. Krieger, and J. S. Muenter, "Molecular beam electric resonance study of formaldehyde, thioformaldehyde, and ketene," *J. Chem. Phys.*, vol. 67, pp. 1576–1586, 1977.

[64] L. Esterowitz, "Rotational transitions and centrifugal distortion in UHF spectrum of formaldehyde," *J. Chem. Phys.*, vol. 39, p. 247, 1963.

[65] R. Cornet and G. Winnewisser, "A precise study of the rotational spectrum of formaldehyde $H_2{}^{12}C^{16}O$, $H_2{}^{13}C^{16}O$, $H_2{}^{12}C^{18}O$, $H_2{}^{13}C^{18}O$," *J. Mol. Spectrosc.*, vol. 80, pp. 438–452, 1980.

[66] R. B. Nerf, "Laboratory measurement of millimeter-wavelength spectrum of formaldehyde," *Astrophys. J.*, vol. 174, pp. 467–468, 1972.

[67] R. B. Lawrance and M. W. P. Strandberg, "Centrifugal distortion in asymmetric top molecules. I. Ordinary formaldehyde, $H_2{}^{12}CO$," *Phys. Rev.*, vol. 83, pp. 363–369, 1951.

[68] G. Erlandsson, "Millimeter wave spectrum of formaldehyde," *J. Chem. Phys.*, vol. 25, pp. 579–580, 1956.

[69] T. Oka, K. Takagi, and Y. Morino, "Microwave spectrum of formaldehyde in vibrationally excited states," *J. Mol. Spectrosc.*, vol. 14, pp. 27–52, 1964.

[70] S. Carter, N. C. Handy, and J. Demaison, "The rotational levels of the ground vibrational state of formaldehyde," *Mol. Phys.*, vol. 90, pp. 729–737, 1997.

[71] D. R. Johnson, F. J. Lovas, and W. H. Kirchhoff, "Microwave spectra of molecules of astrophysical interest: 1. Formaldehyde, formamide, and thioformaldehyde," *J. Phys. Chem. Ref. Data*, vol. 1, pp. 1011–1046, 1972.

[72] D. Dangoisse, E. Willemot, and J. Bellet, "Microwave spectrum of formaldehyde and its isotopic species in D, $^{13}C$, and $^{18}O$: study of Coriolis resonance between $\nu_4$ and $\nu_6$ vibrational excited states," *J. Mol. Spectrosc.*, vol. 71, pp. 414–429, 1978.

[73] F. Y. Chu, S. M. Freund, J. W. C. Johns, and T. Oka, "$\Delta K = 2$ transitions in $H_2CO$ and $D_2CO$," *J. Mol. Spectrosc.*, vol. 48, pp. 328–335, 1973.

[74] T. Tipton, J.-I. Choe, S. G. Kukolich, and R. Hubbard, "Fourier transform spectroscopy on the $3\nu_2$, $2\nu_2 + \nu_6$ and $\nu_3 + \nu_5$ bands of $H_2CO$," *J. Mol. Spectrosc.*, vol. 114, pp. 239–256, 1985.

[75] C. Bréchignac, J. W. C. Johns, A. R. W. McKellar, and M. Wong, "The $\nu_2$ fundamental band of $H_2CO$," *J. Mol. Spectrosc.*, vol. 96, pp. 353–361, 1982.

[76] L. R. Brown, R. H. Hunt, and A. S. Pine, "Wavenumbers, line strengths, and assignments in the Doppler-limited spectrum of formaldehyde from 2700 $cm^{-1}$ to 3000 $cm^{-1}$," *J. Mol. Spectrosc.*, vol. 75, pp. 406–428, 1979.

[77] D. M. Sweger and R. L. Sams, "Diode laser spectra of the $\nu_2$ band of $H_2{}^{12}CO$ and $H_2{}^{13}CO$," *J. Mol. Spectrosc.*, vol. 87, pp. 18–28, 1981.

[78] D. S. Cline and P. L. Varghese, "High resolution spectral measurements in the $\nu_5$ band of formaldehyde using a tunable IR diode laser," *Appl. Optics*, vol. 27, pp. 3219–3224, 1988.

[79] F. Ito, T. Nakanaga, and H. Takeo, "FTIR spectra of the $2\nu_4$, $\nu_4 + \nu_6$ and $2\nu_6$ bands of formaldehyde," *Spectrochim. Acta A*, vol. 50, pp. 1397–1412, 1994.

[80] R. A. Toth, "High resolution measurements of the line positions and strengths of the $2\nu_2$ band of $H_2CO$," *J. Mol. Spectrosc.*, vol. 46, pp. 470–489, 1973.

[81] M. Allegrini, J. Johns, and A. McKellar, "A study of the Coriolis-coupled $\nu_4$, $\nu_6$, and $\nu_3$ fundamental bands and the $\nu_5 \leftarrow \nu_6$ difference band of $H_2CO$; measurement of the dipole moment for $\nu_5 = 1$," *J. Mol. Spectrosc.*, vol. 67, pp. 476–495, 1977.

[82] M. Allegrini, J. W. C. Johns, and A. R. W. McKellar, "Stark spectroscopy with the CO laser: the $\nu_3$ fundamental band of $H_2CO$," *J. Mol. Spectrosc.*, vol. 66, pp. 69–78, 1977.

[83] T. Nakagawa, K. Yamada, and K. Kuchitsu, "Vibration-rotation spectrum of formaldehyde: C–H stretching fundamentals $\nu_1$ and $\nu_5$," *J. Mol. Spectrosc.*, vol. 63, pp. 485–508, 1976.

[84] I. E. Gordon, L. S. Rothman, C. Hill, R. V. Kochanov, Y. Tan, P. F. Bernath, M. Birk, V. Boudon, A. Campargue, K. Chance, *et al.*, "The HITRAN 2016 molecular spectroscopic database," *J. Quant. Spectrosc. Rad. Transf.*, vol. 203, pp. 3–69, 2017.

[85] H. Takuma, T. Shimizu, and K. Shimoda, "Magnetic hyperfine spectrum of $H_2CO$ by a maser," *J. Phys. Soc. Jpn.*, vol. 14, pp. 1595–1599, 1959.

[86] K. D. Tucker, P. Thaddeus, and G. R. Tomasevich, "Precise laboratory measurement of 4830-MHz formaldehyde rotational transition," *Astrophys. J.*, vol. 161, pp. L153–L154, 1970.

[87] P. Fjodorow, O. Hellmig, V. M. Baev, H. B. Levinsky, and A. V. Mokhov, "Intracavity absorption spectroscopy of formaldehyde from 6230 to 6420 $cm^{-1}$," *Appl. Phys. B*, vol. 123, p. 147, 2017.

[88] D. Luckhaus, M. J. Coffey, M. D. Fritz, and F. F. Crim, "Experimental and theoretical vibrational overtone spectra of $v_{\mathrm{CH}} = 3, 4, 5$, and 6 in formaldehyde ($H_2CO$)," *J. Chem. Phys.*, vol. 104, pp. 3472–3478, 1996.

[89] D. C. Reuter, S. Nadler, S. J. Daunt, and J. W. C. Johns, "Frequency and intensity analysis of the $\nu_3$ band, $\nu_4$ band and $\nu_6$ band of formaldehyde," *J. Chem. Phys.*, vol. 91, pp. 646–654, 1989.

[90] S. Nadler, S. J. Daunt, and D. C. Reuter, "Tunable diode-laser measurements of formaldehyde foreign-gas broadening parameters and line strengths in the 9–11 $\mu$m region," *Appl. Optics*, vol. 26, pp. 1641–1646, 1987.

[91] A. S. Pine, "Doppler-limited spectra of C–H stretching fundamentals of formaldehyde," *J. Mol. Spectrosc.*, vol. 70, pp. 167–178, 1978.

[92] R. B. Nerf, "Pressure broadening and shift in the millimeter-wave spectrum of formaldehyde," *J. Mol. Spectrosc.*, vol. 58, pp. 451–473, 1975.

[93] J. W. C. Johns and A. R. W. McKellar, "Stark spectroscopy with the CO laser: The $\nu_2$ fundamentals of $H_2CO$ and $D_2CO$," *J. Mol. Spectrosc.*, vol. 48, pp. 354–371, 1973.

[94] T. Oka, H. Hirakawa, and K. Shimoda, "Microwave spectrum of formaldehyde. I. $K$-type doubling spectra," *J. Phys. Soc. Jpn.*, vol. 15, pp. 2265–2273, 1960.

[95] A. G. Császár, T. Furtenbacher, and P. Árendás, "Small molecules – big data," *J. Phys. Chem. A*, vol. 120, pp. 8949–8969, 2016.

[96] R. Tóbiás, T. Furtenbacher, I. Simkó, A. G. Császár, M. L. Diouf, F. M. J. Cozijn, J. M. A. Staa, E. J. Salumbides, and W. Ubachs, "Spectroscopic-network-assisted precision spectroscopy and its application to water," *Nat. Commun.*, vol. 11, p. 1708, 2020.

[97] J. L. Hardvick and S. M. Till, "Laser excited resonance fluorescence in formaldehyde," *J. Chem. Phys.*, vol. 70, p. 2340, 1979.

[98] A. F. Al-Refaie, S. N. Yurchenko, A. Yachmenev, and J. Tennyson, "ExoMol line lists VIII: a variationally computed line list for hot formaldehyde," *Mon. Not. R. Astron. Soc.*, vol. 448, pp. 1704–1714, 2015.

[99] K. Yamada, "Resonance between ground and excited vibrational state due to centrifugal distortion coupling in the rotational spectrum of HNCO," *J. Mol. Spectrosc.*, vol. 81, no. 1, pp. 139–151, 1980.

[100] L. H. Coudert, "Extreme anomalous centrifugal distortion in methylene," *J. Chem. Phys.*, vol. 153, no. 14, p. 144115, 2020.

[101] S. Urban and K. Yamada, "A breakdown of the Watson-type Hamiltonian for some asymmetric top molecules," *J. Mol. Spectrosc.*, vol. 160, no. 1, pp. 279–288, 1993.

[102] I. Scivetti, J. Kohanoff, and N. I. Gidopoulos, "On the treatment of singularities of the Watson Hamiltonian for nonlinear molecules," *Int. J. Quant. Chem.*, vol. 111, no. 2, pp. 307–317, 2011.

[103] C. Puzzarini, G. Cazzoli, M. E. Harding, J. Vázquez, and J. Gauss, "A new experimental absolute nuclear magnetic shielding scale for oxygen based on the rotational hyperfine structure of $H_2{}^{17}O$," *J. Chem. Phys.*, vol. 131, no. 23, pp. 234304–234304, 2009.

[104] M. Melosso, L. Dore, J. Gauss, and C. Puzzarini, "Deuterium hyperfine splittings in the rotational spectrum of $NH_2D$ as revealed by Lamb-dip spectroscopy," *J. Mol. Spectrosc.*, vol. 370, p. 111291, 2020.

[105] M. Melosso, M. L. Diouf, L. Bizzocchi, M. E. Harding, F. M. Cozijn, C. Puzzarini, and W. Ubachs, "Hyperfine-resolved near-infrared spectra of $H_2{}^{17}O$," *J. Phys. Chem. A*, vol. 125, no. 36, pp. 7884–7890, 2021.

[106] Y. Aikawa, V. Wakelam, F. Hersant, R. T. Garrod, and E. Herbst, "From prestellar to protostellar cores. II. Time dependence and deuterium fractionation," *Astrophys. J.*, vol. 760, no. 1, p. 40, 2012.

[107] H.-R. Chen, S.-Y. Liu, Y.-N. Su, and M.-Y. Wang, "Deuterium fractionation as an evolutionary probe in massive protostellar/cluster cores," *Astrophys. J.*, vol. 743, no. 2, p. 196, 2011.

[108] M. Emprechtinger, P. Caselli, N. Volgenau, J. Stutzki, and M. Wiedner, "The $N_2D^+/N_2H^+$ ratio as an evolutionary tracer of Class 0 protostars," *Astron. Astrophys.*, vol. 493, no. 1, pp. 89–105, 2009.

[109] F. Fontani, A. Palau, P. Caselli, Á. Sánchez-Monge, M. Butler, J. Tan, I. Jiménez-Serra, G. Busquet, S. Leurini, and M. Audard, "Deuteration as an evolutionary tracer in massive-star formation," *Astron. Astrophys.*, vol. 529, p. L7, 2011.

[110] E. Bianchi, C. Ceccarelli, C. Codella, J. Enrique-Romero, C. Favre, and B. Lefloch, "Astrochemistry as a tool to follow protostellar evolution: The class I stage," *ACS Earth Space Chem.*, vol. 3, no. 12, pp. 2659–2674, 2019.

[111] A. Cheung, D. M. Rank, C. Townes, D. D. Thornton, and W. Welch, "Detection of water in interstellar regions by its microwave radiation," *Nature*, vol. 221, no. 5181, pp. 626–628, 1969.

[112] B. Turner, B. Zuckerman, N. Fourikis, M. Morris, and P. Palmer, "Microwave detection of interstellar HDO," *Astrophys. J.*, vol. 198, pp. L125–L128, 1975.

[113] T. Jacq, P. Jewell, C. Henkel, C. Walmsley, and A. Baudry, "$H_2{}^{18}O$ in hot dense molecular cloud cores," *Astron. Astrophys.*, vol. 199, pp. L5–L8, 1988.

[114] Å. Hjalmarson, P. Bergman, N. Biver, H.-G. Florén, U. Frisk, T. Hasegawa, K. Justtanont, B. Larsson, S. Lundin, M. Olberg, *et al.*, "Recent astronomy highlights from the Odin satellite," *Adv. Space Res.*, vol. 36, no. 6, pp. 1031–1047, 2005.

[115] H. Butner, S. Charnley, C. Ceccarelli, S. Rodgers, J. Pardo, B. Parise, J. Cernicharo, and G. Davis, "Discovery of interstellar heavy water," *Astrophys. J.*, vol. 659, no. 2, p. L137, 2007.

[116] E. F. van Dishoeck, D. J. Jansen, P. Schilke, and T. Phillips, "Detection of the interstellar $NH_2$ radical," *Astrophys. J.*, vol. 416, p. L83, 1993.

[117] M. Melosso, L. Bizzocchi, O. Sipilä, B. Giuliano, L. Dore, F. Tamassia, M.-A. Martin-Drumel, O. Pirali, E. Redaelli, and P. Caselli, "First detection of NHD and $ND_2$ in the interstellar medium. Amidogen deuteration in IRAS 16293–2422," *Astron. Astrophys.*, vol. 641, p. A153, 2020.

[118] J. M. Hollis, P. R. Jewell, and F. J. Lovas, "Confirmation of interstellar methylene," *Astrophys. J.*, vol. 438, pp. 259–264, 1995.

[119] P. Thaddeus, M. Kutner, A. Penzias, R. Wilson, and K. Jefferts, "Interstellar hydrogen sulfide," *Astrophys. J.*, vol. 176, p. L73, 1972.

[120] Y. Minh, L. M. Ziurys, W. M. Irvine, and D. McGonagle, "Observations of the $H_2S$ toward OMC-1," *Astrophys. J.*, vol. 360, pp. 136–141, 1990.

[121] C. Vastel, T. Phillips, C. Ceccarelli, and J. Pearson, "First detection of doubly deuterated hydrogen sulfide," *Astrophys. J.*, vol. 593, no. 2, p. L97, 2003.

[122] G. Macdonald, A. Gibb, R. Habing, and T. Millar, "A 330-360 GHz spectral survey of G34.3+0.15. I. Data and physical analysis," *Astron. Astrophys. Suppl. Ser.*, vol. 119, no. 2, pp. 333–367, 1996.

[123] M. N. Drozdovskaya, E. F. van Dishoeck, J. K. Jørgensen, U. Calmonte, M. H. van der Wiel, A. Coutens, H. Calcutt, H. S. Müller, P. Bjerkeli, M. V. Persson, *et al.*, "The ALMA-PILS survey: the sulphur connection between protostars and comets: IRAS 16293–2422 B and 67P/Churyumov–Gerasimenko," *Mon. Not. R. Astron. Soc.*, vol. 476, no. 4, pp. 4949–4964, 2018.

[124] S. Viti, P. Caselli, T. W. Hartquist, and D. A. Williams, "Chemical signatures of shocks in hot cores," *Astron. Astrophys.*, vol. 370, no. 3, pp. 1017–1025, 2001.

[125] N. Sakai, T. Sakai, T. Hirota, Y. Watanabe, C. Ceccarelli, C. Kahane, S. Bottinelli, E. Caux, K. Demyk, C. Vastel, *et al.*, "Change in the chemical composition of infalling gas forming a disk around a protostar," *Nature*, vol. 507, no. 7490, pp. 78–80, 2014.

[126] L. Podio, C. Codella, F. Gueth, S. Cabrit, R. Bachiller, A. Gusdorf, C.-F. Lee, B. Lefloch, S. Leurini, B. Nisini, *et al.*, "The jet and the disk of the HH 212 low-mass protostar imaged by ALMA: SO and $SO_2$ emission," *Astron. Astrophys.*, vol. 581, p. A85, 2015.

[127] D. Ruffle, T. Hartquist, P. Caselli, and D. Williams, "The sulphur depletion problem," *Mon. Not. R. Astron. Soc.*, vol. 306, no. 3, pp. 691–695, 1999.

[128] D. Bockelée-Morvan, D. Lis, J. Wink, D. Despois, J. Crovisier, R. Bachiller, D. Benford, N. Biver, P. Colom, J. Davies, *et al.*, "New molecules found in comet C/1995 O1 (Hale-Bopp). Investigating the link between cometary and interstellar material," *Astron. Astrophys.*, vol. 353, pp. 1101–1114, 2000.

[129] R. Hillger and M. Strandberg, "Centrifugal distortion in asymmetric molecules. II. HDS," *Phys. Rev.*, vol. 83, no. 3, p. 575, 1951.

[130] P. Helminger, R. L. Cook, and F. C. De Lucia, "Microwave spectrum and centrifugal distortion effects of HDS," *J. Mol. Spectrosc.*, vol. 40, no. 1, pp. 125–136, 1971.

[131] P. Helminger, F. C. DeLucia, and W. H. Kirchhoff, "Microwave spectra of molecules of astrophysical interest: IV. hydrogen sulfide," *J. Phys. Chem. Ref. Data*, vol. 2, no. 2, pp. 215–224, 1973.

[132] F. J. Lovas, "Microwave spectral tables II. Triatomic molecules," *J. Phys. Chem. Ref. Data*, vol. 7, no. 4, pp. 1445–1750, 1978.

[133] C. Camy-Peyret, J.-M. Flaud, L. Lechuga-Fossat, and J. Johns, "The far-infrared spectrum of deuterated hydrogen sulfide: The ground state rotational constants of $D_2{}^{32}S$, $D_2{}^{34}S$, $HD^{32}S$, and $HD^{34}S$," *J. Mol. Spectrosc.*, vol. 109, no. 2, pp. 300–333, 1985.

[134] O. N. Ulenikov, R. Tolchenov, E. Melekhina, M. Koivusaari, S. Alanko, and R. Anttila, "High resolution study of deuterated hydrogen sulfide in the region 2400–3000 $cm^{-1}$," *J. Mol. Spectrosc.*, vol. 170, no. 2, pp. 397–416, 1995.

[135] C. Sydow, O. Ulenikov, E. Bekhtereva, O. Gromova, Z. Xintong, P. Glushkov, C. Maul, and S. Bauerecker, "Extended analysis of FTIR high resolution spectra of $HD^{32}S$ and $HD^{34}S$ in the region of the $\nu_2$ band: Positions and strengths of individual lines," *J. Quant. Spectrosc. Rad. Transf.*, vol. 225, pp. 286–300, 2019.

[136] O. Ulenikov, E. Bekhtereva, O. Gromova, N. Raspopova, C. Sydow, and S. Bauerecker, "Extended analysis of the $\nu_3$ band of $HD^{32}S$: Line positions, energies, and line strengths," *J. Quant. Spectrosc. Rad. Transf.*, vol. 230, pp. 131–141, 2019.

[137] O. N. Ulenikov, A.-W. Liu, E. S. Bekhtereva, G. Onopenko, O. V. Gromova, L. Wan, S.-M. Hu, and J.-M. Flaud, "Joint ro-vibrational analysis of the HDS high resolution infrared data," *J. Mol. Spectrosc.*, vol. 240, no. 1, pp. 32–44, 2006.

[138] A.-W. Liu, B. Gao, G.-S. Cheng, F. Qi, and S.-M. Hu, "High-resolution rotational analysis of HDS: $2\nu_3$, $\nu_2$+ $2\nu_3$, $3\nu_3$, and $\nu_2$+ $3\nu_3$ bands," *J. Mol. Spectrosc.*, vol. 232, no. 2, pp. 279–290, 2005.

[139] V. G. Tyuterev, L. Régalia-Jarlot, D. W. Schwenke, S. A. Tashkun, and Y. G. Borkov, "Global variational calculations of high-resolution rovibrational spectra: isotopic effects, intensity anomalies and experimental confirmations for $H_2S$, HDS, $D_2S$ molecules," *Comptes Rendus Physique*, vol. 5, no. 2, pp. 189–199, 2004.

[140] P. Thaddeus, L. Krisher, and J. Loubser, "Hyperfine structure in the microwave spectrum of HDO, HDS, $CH_2O$, and CHDO: Beam-maser spectroscopy on asymmetric-top molecules," *J. Chem. Phys.*, vol. 40, no. 2, pp. 257–273, 1964.

[141] O. Ulenikov, R. Tolchenov, M. Koivusaari, S. Alanko, and R. Antilla, "Study of the fine rotational structure of the $\nu_2$ band of HDS," *J. Mol. Spectrosc.*, vol. 170, no. 1, pp. 1–9, 1995.

[142] O. Ulenikov, G. Onopenko, I. Olekhnovitch, S. Alanko, V.-M. Horneman, M. Koivusaari, and R. Anttila, "High-resolution fourier transform spectra of HDS in the regions of the bands $\nu_1$ and $2\nu_1/\nu_2$+ $\nu_3$," *J. Mol. Spectrosc.*, vol. 189, no. 1, pp. 74–82, 1998.

[143] O. Ulenikov, E. Ditenberg, I. Olekhnovitch, S. Alanko, M. Koivusaari, and R. Anttila, "Isotope substitution in near local mode molecules: Bending overtones n$\nu_2$ (n= 2, 3) of the HDS molecule," *J. Mol. Spectrosc.*, vol. 191, no. 2, pp. 239–247, 1998.

[144] I. Gordon, L. Rothman, R. Hargreaves, R. Hashemi, E. Karlovets, F. Skinner, E. Conway, C. Hill, R. Kochanov, Y. Tan, *et al.*, "The HITRAN2020 molecular spectroscopic database," *J. Quant. Spectrosc. Rad. Transf.*, p. 107949, 2022.

[145] W. Langer, F. Schloerb, R. Snell, and J. Young, "Detection of deuterated cyanoacetylene in the interstellar cloud TMC-1," *Astrophys. J.*, vol. 239, pp. L125–L128, 1980.

[146] D. Howe, T. Millar, P. Schilke, and C. Walmsley, "Observations of deuterated cyanoacetylene in dark clouds," *Mon. Not. R. Astron. Soc.*, vol. 267, no. 1, pp. 59–68, 1994.

[147] G. B. Esplugues, J. Cernicharo, S. Viti, J. R. Goicoechea, B. Tercero, N. Marcelino, A. Palau, T. A. Bell, E. A. Bergin, N. R. Crockett, *et al.*, "Combined IRAM and Herschel/HIFI study of cyano(di)acetylene in Orion KL: tentative detection of $DC_3N$," *Astron. Astrophys.*, vol. 559, p. A51, 2013.

[148] A. Belloche, H. Müller, R. Garrod, and K. Menten, "Exploring molecular complexity with ALMA (EMoCA): Deuterated complex organic molecules in Sagittarius B2 (N2)," *Astron. Astrophys.*, vol. 587, p. A91, 2016.

[149] V. Rivilla, L. Colzi, F. Fontani, M. Melosso, P. Caselli, L. Bizzocchi, F. Tamassia, and L. Dore, "$DC_3N$ observations towards high-mass star-forming regions," *Mon. Not. R. Astron. Soc.*, vol. 496, pp. 1990–1999, 2020.

[150] C. Ceccarelli, P. Caselli, D. Bockelée-Morvan, O. Mousis, S. Pizzarello, F. Robert, and D. Semenov, "Deuterium fractionation: The Ariadne's thread from the precollapse phase to meteorites and comets today," *Protostars and Planets VI*, pp. 859–882, 2014.

[151] M. Melosso, L. Bizzocchi, A. Adamczyk, E. Canè, P. Caselli, L. Colzi, L. Dore, B. M. Giuliano, J.-C. Guillemin, M.-A. Martin-Drumel, *et al.*, "Extensive ro-vibrational analysis of deuterated-cyanoacetylene ($DC_3N$) from millimeter-wavelengths to the infrared domain," *J. Quant. Spectrosc. Rad. Transf.*, vol. 254, p. 107221, 2020.

[152] P. Mallinson and A. Fayt, "High resolution infra-red studies of HCCCN and DCCCN," *Mol. Phys.*, vol. 32, no. 2, pp. 473–485, 1976.

[153] K. Yamada, R. Schieder, G. Winnewisser, and A. Mantz, "Diode laser spectrum of HCCCN near 5 $\mu$m," *Z. Naturforsch. A*, vol. 35, no. 7, pp. 690–693, 1980.

[154] K. Yamada and G. Winnewisser, "Diode laser spectrum of HCCCN near 5 $\mu$m. The hot band," *Z. Naturforsch. A*, vol. 36, no. 1, pp. 23–29, 1981.

[155] K. Yamada, R. Best, and G. Winnewisser, "Diode laser spectrum of HCCCN: CN stretching band," *Z. Naturforsch. A*, vol. 38, no. 12, pp. 1296–1308, 1983.

[156] Y. Bénilan, A. Jolly, F. Raulin, and J.-C. Guillemin, "IR band intensities of $DC_3N$ and $HC_3^{15}N$: Implication for observations of Titan's atmosphere," *Planet. Space Sci.*, vol. 54, no. 6, pp. 635–640, 2006.

[157] P. Stoppa, N. Tasinato, A. Baldacci, A. P. Charmet, S. Giorgianni, F. Tamassia, E. Cané, and M. Villa, "FTIR spectra of $CH_2F_2$ in the 1000–1300 $cm^{-1}$ region: Rovibrational analysis and modeling of the Coriolis and anharmonic resonances in the $\nu_3$, $\nu_5$, $\nu_7$, $\nu_9$ and $2\nu_4$ polyad," *J. Quant. Spectrosc. Rad. Transf.*, vol. 175, pp. 8–16, 2016.

[158] F. Tamassia, M. Melosso, L. Dore, M. Pettini, E. Canè, P. Stoppa, and A. P. Charmet, "Spectroscopy of a low global warming power refrigerant. Infrared and millimeter-wave spectra of trifluoroethene (HFO-1123) in the ground and some vibrational excited states," *J. Quant. Spectrosc. Rad. Transf.*, vol. 248, p. 106980, 2020.

[159] C. M. Western, "PGOPHER: A program for simulating rotational, vibrational and electronic spectra," *J. Quant. Spectrosc. Rad. Transf.*, vol. 186, pp. 221–242, 2017.

[160] L. Bizzocchi, F. Tamassia, J. Laas, *et al.*, "Rotational and high-resolution infrared spectrum of $HC_3N$: global ro-vibrational analysis and improved line catalog for astrophysical observations," *Astrophys. J. Suppl. Ser.*, vol. 233, no. 1, p. 11, 2017.

[161] A. Jolly, Y. Benilan, and A. Fayt, "New infrared integrated band intensities for $HC_3N$ and extensive line list for the $\nu_5$ and $\nu_6$ bending modes," *J. Mol. Spectrosc.*, vol. 242, no. 1, pp. 46–54, 2007.

[162] H. M. Pickett, "The fitting and prediction of vibration-rotation spectra with spin interactions," *J. Mol. Spectrosc.*, vol. 148, no. 2, pp. 371–377, 1991.

[163] W. Łodyga, M. Kreglewski, P. Pracna, and Š. Urban, "Advanced graphical software for assignments of transitions in rovibrational spectra," *J. Mol. Spectrosc.*, vol. 243, no. 2, pp. 182–188, 2007.

[164] E. Nakamura, K. Kobayashi, R. Tanaka, T. Kunihiro, H. Kitagawa, C. Potiszil, T. Ota, C. Sakaguchi, M. Yamanaka, D. M. Ratnayake, *et al.*, "On the origin and evolution of the asteroid Ryugu: a comprehensive geochemical perspective," *Proc. Jap. Ac., Ser. B*, vol. 98, no. 6, pp. 227–282, 2022.

[165] M. A. Sephton, "Organic compounds in carbonaceous meteorites," *Nat. Pro. Rep.*, vol. 19, no. 3, pp. 292–311, 2002.

[166] K. Altwegg, H. Balsiger, A. Bar-Nun, J.-J. Berthelier, A. Bieler, P. Bochsler, C. Briois, U. Calmonte, M. R. Combi, H. Cottin, *et al.*, "Prebiotic chemicals—amino acid and phosphorus—in the coma of comet 67P/Churyumov-Gerasimenko," *Sci. Adv.*, vol. 2, no. 5, p. e1600285, 2016.

[167] M. P. Bernstein, S. F. Ashbourn, S. A. Sandford, and L. J. Allamandola, "The lifetimes of nitriles (CN) and acids (COOH) during ultraviolet photolysis and their survival in space," *Astrophys. J.*, vol. 601, no. 1, p. 365, 2004.

[168] A. Strecker, "Ueber die künstliche bildung der milchsäure und einen neuen, dem glycocoll homologen körper," *Justus Liebigs Annalen der Chemie*, vol. 75, no. 1, pp. 27–45, 1850.

[169] D. M. Koch, C. Toubin, G. H. Peslherbe, and J. T. Hynes, "A theoretical study of the formation of the aminoacetonitrile precursor of glycine on icy grain mantles in the interstellar medium," *J. Phys. Chem. C*, vol. 112, no. 8, pp. 2972–2980, 2008.

[170] G. Danger, J.-B. Bossa, P. De Marcellus, F. Borget, F. Duvernay, P. Theulé, T. Chiavassa, and L. d'Hendecourt, "Experimental investigation of nitrile formation from VUV photochemistry of interstellar ices analogs: acetonitrile and amino acetonitrile," *Astron. Astrophys.*, vol. 525, p. A30, 2011.

[171] Y. Kim and R. Kaiser, "On the formation of amines ($RNH_2$) and the cyanide anion ($CN^-$) in electron-irradiated ammonia–hydrocarbon interstellar model ices," *Astrophys. J.*, vol. 729, no. 1, p. 68, 2011.

[172] C. He and M. A. Smith, "Identification of nitrogenous organic species in Titan aerosols analogs: Implication for prebiotic chemistry on Titan and early Earth," *Icarus*, vol. 238, pp. 86–92, 2014.

[173] J. MacDonald and J. Tyler, "The microwave spectrum of aminoacetonitrile," *J. Chem. Soc. Chem. Comm.*, no. 17, pp. 995–995, 1972.

[174] H. M. Pickett, "The microwave spectrum, structure, and dipole moment of amino acetonitrile," *J. Mol. Spectrosc.*, vol. 46, no. 3, pp. 335–340, 1973.

[175] M. Bogey, H. Dubus, and J. Guillemin, "The millimeter-wave spectrum of aminoacetonitrile," *J. Mol. Spectrosc.*, vol. 143, no. 1, pp. 180–182, 1990.

[176] Y. Motoki, Y. Tsunoda, H. Ozeki, and K. Kobayashi, "Submillimeter-wave spectrum of aminoacetonitrile and its deuterated isotopologues, possible precursors of the simplest amino acid glycine," *Astrophys. J. Suppl. Ser.*, vol. 209, no. 2, p. 23, 2013.

[177] L. Kolesniková, E. Alonso, S. Mata, and J. Alonso, "Rotational spectra in 29 vibrationally excited states of interstellar aminoacetonitrile," *Astrophys. J. Suppl. Ser.*, vol. 229, no. 2, p. 26, 2017.

[178] A. Belloche, K. Menten, C. Comito, H. Müller, P. Schilke, J. Ott, S. Thorwirth, and C. Hieret, "Detection of amino acetonitrile in Sgr B2 (N)," *Astron. Astrophys.*, vol. 492, no. 3, pp. 769–773, 2008.

[179] C. Richard, A. Belloche, L. Margulès, R. Motiyenko, K. Menten, R. Garrod, and H. Müller, "Rotational spectrum of 3-aminopropionitrile and searches for it in Sagittarius B2 (N)," *J. Mol. Spectrosc.*, vol. 345, pp. 51–59, 2018.

[180] C. Degli Esposti, L. Dore, M. Melosso, K. Kobayashi, C. Fujita, and H. Ozeki, "Millimeter-wave and submillimeter-wave spectra of aminoacetonitrile in the three lowest vibrational excited states," *Astrophys. J. Suppl. Ser.*, vol. 230, no. 2, p. 26, 2017.

[181] M. Melosso, A. Belloche, M.-A. Martin-Drumel, O. Pirali, F. Tamassia, L. Bizzocchi, R. Garrod, H. Müller, K. Menten, L. Dore, and C. Puzzarini, "Far-infrared laboratory spectroscopy of aminoacetonitrile and first interstellar detection of its vibrationally excited transitions," *Astron. Astrophys.*, vol. 641, p. A160, 2020.

[182] B. Bak, E. Hansen, F. Nicolaisen, and O. Nielsen, "Vibrational spectra of aminoacetonitrile," *Can. J. Phys.*, vol. 53, no. 19, pp. 2183–2188, 1975.

[183] M. P. Bernstein, C. W. Bauschlicher Jr, and S. A. Sandford, "The infrared spectrum of matrix isolated aminoacetonitrile, a precursor to the amino acid glycine," *Adv. Space Res.*, vol. 33, no. 1, pp. 40–43, 2004.

[184] J.-B. Brubach, L. Manceron, M. Rouzières, O. Pirali, D. Balcon, F. Kwabia-Tchana, V. Boudon, M. Tudorie, T. Huet, A. Cuisset, and P. Roy, "Performance of the AILES THz-Infrared beamline at SOLEIL for High resolution spectroscopy," in *WIRMS 2009*, vol. 1214 of *AIP Conference Proceedings*, pp. 81–84, 2010.

[185] O. Pirali, V. Boudon, J. Oomens, and M. Vervloet, "Rotationally resolved infrared spectroscopy of adamantane," *J. Chem. Phys.*, vol. 136, p. 024310, 2012.

[186] O. Pirali, M. Goubet, T. R. Huet, R. Georges, P. Soulard, P. Asselin, J. Courbe, P. Roy, and M. Vervloet, "The far infrared spectrum of naphthalene characterized by high resolution synchrotron FTIR spectroscopy and anharmonic DFT calculations," *Phys. Chem. Chem. Phys.*, vol. 15, no. 25, pp. 10141–10150, 2013.

[187] M. Faye, M. Bordessoule, B. Kanouté, J.-B. Brubach, P. Roy, and L. Manceron, "Improved mid infrared detector for high spectral or spatial resolution and synchrotron radiation use," *Rev. Sci. Instrum.*, vol. 87, p. 063119, 2016.

[188] V.-M. Horneman, R. Anttila, S. Alanko, and J. Pietilä, "Transferring calibration from $CO_2$ laser lines to far infrared water lines with the aid of the $\nu_2$ band of OCS and the $\nu_2$, $\nu_1$- $\nu_2$, and $\nu_1$+ $\nu_2$ bands of $^{13}CS_2$: Molecular constants of $^{13}CS_2$," *J. Mol. Spectrosc.*, vol. 234, no. 2, pp. 238–254, 2005.

[189] K. B. Wiberg, P. R. Rablen, and J. H. Baraban, "Butadiene and heterodienes revisited," *J. Org. Chem.*, vol. 83, no. 15, pp. 8473–8482, 2018.

[190] M.-A. Martin-Drumel, J. P. Porterfield, M. Goubet, P. Asselin, R. Georges, P. Soulard, M. Nava, P. B. Changala, B. Billinghurst, O. Pirali, *et al.*, "Synchrotron-based high resolution far-infrared spectroscopy of *trans*-butadiene," *J. Phys. Chem. A*, vol. 124, no. 12, pp. 2427–2435, 2020.

[191] N. C. Craig, K. A. Hanson, R. W. Pierce, S. D. Saylor, and R. L. Sams, "Rotational analysis of bands in the high-resolution infrared spectra of the three species of butadiene-1,4-$d_2$; refinement of the assignments of the vibrational fundamentals," *J. Mol. Spectrosc.*, vol. 228, no. 2, pp. 401–413, 2004.

[192] N. C. Craig, J. L. Davis, K. A. Hanson, M. C. Moore, K. J. Weidenbaum, and M. Lock, "Analysis of the rotational structure in bands in the high-resolution infrared spectra of butadiene and butadiene-2,3-$d_2$: refinement in assignments of fundamentals," *J. Mol. Struct.*, vol. 695-696, pp. 59–69, 2004.

[193] N. C. Craig, K. A. Hanson, M. C. Moore, and R. L. Sams, "Rotational analysis of several bands in the high-resolution infrared spectrum of butadiene-1-$^{13}C_1$: assignment of vibrational fundamentals," *J. Mol. Struct.*, vol. 742, no. 1, pp. 21–29, 2005.

[194] N. C. Craig, M. C. Moore, A. K. Patchen, and R. L. Sams, "Analysis of rotational structure in the high-resolution infrared spectrum and assignment of vibrational fundamentals of butadiene-2,3-$^{13}C_2$," *J. Mol. Struct.*, vol. 235, no. 2, pp. 181–189, 2006.

[195] J. H. Baraban, M.-A. Martin-Drumel, P. B. Changala, S. Eibenberger, M. Nava, D. Patterson, J. F. Stanton, G. B. Ellison, and M. C. McCarthy, "The molecular structure of *gauche*-1,3-butadiene: Experimental establishment of non-planarity," *Angew. Chem.*, vol. 130, no. 7, pp. 1839–1843, 2018.

[196] C. Puzzarini, E. Penocchio, M. Biczysko, and V. Barone, "Molecular structure and spectroscopic signatures of acrolein: Theory meets experiment," *J. Phys. Chem. A*, vol. 118, no. 33, pp. 6648–6656, 2014.

[197] J. Fine, J. Goldstein, and J. Simmons, "Microwave spectrum of *s-trans* acrolein," *J. Chem. Phys.*, vol. 23, no. 3, pp. 601–601, 1955.

[198] R. Wagner, J. Fine, J. Simmons, and J. Goldstein, "Microwave spectrum, structure, and dipole moment of *s-trans* acrolein," *J. Chem. Phys.*, vol. 26, no. 3, pp. 634–637, 1957.

[199] E. Cherniak and C. Costain, "Microwave spectrum and molecular structure of *trans*-acrolein," *J. Chem. Phys.*, vol. 45, no. 1, pp. 104–110, 1966.

[200] M. Winnewisser, G. Winnewisser, T. Honda, and E. Hirota, "Ground state centrifugal distortion constants of *Trans*-acrolein, $CH_2$=CH−CHO from the microwave and millimeter wave rotational spectra," *Z. Naturforsch. A*, vol. 30, no. 8, pp. 1001–1014, 1975.

[201] C. Blom and A. Bauder, "Microwave spectrum, rotational constants and dipole moment of *s-cis* acrolein," *Chem. Phys. Lett.*, vol. 88, no. 1, pp. 55–58, 1982.

[202] L. Evangelisti, A. Maris, F. Grieco, C. Calabrese, and S. Melandri, "Millimeter wave free-jet spectrum of acrolein and several isotopologues," *Can. J. Phys.*, vol. 98, no. 6, pp. 555–559, 2020.

[203] A. M. Daly, C. Bermúdez, L. Kolesniková, and J. Alonso, "Comprehensive analysis of prebiotic propenal up to 660 GHz," *Astrophys. J. Suppl. Ser.*, vol. 218, no. 2, p. 30, 2015.

[204] R. E. Penn, "Microwave spectrum of 2-propene-1-imine, $CH_2$=CH−CH=NH," *J. Mol. Spectrosc.*, vol. 69, no. 3, pp. 373–382, 1978.

[205] R. D. Brown, P. D. Godfrey, and D. A. Winkler, "Hyperfine interactions in the microwave spectrum of 2-propen-1-imine (vinylimine)," *Chem. Phys.*, vol. 59, no. 3, pp. 243–247, 1981.

[206] Y. Hamada, M. Tsuboi, T. Matsuzawa, K. Yamanouchi, K. Kuchitsu, Y. Koga, and S. Kondo, "Pyrolysis of amines: Infrared spectrum of allylimine," *J. Mol. Spectrosc.*, vol. 105, no. 2, pp. 453–464, 1984.

[207] M. Sugie, H. Takeo, and C. Matsumura, "A study of the thermal decomposition and dehydrochlorination of N-chloroazetidine. microwave spectra of N-chloromethylenimine, 1-azetine, and 2-azabutadiene," *J. Am. Chem. Soc.*, vol. 111, no. 3, pp. 906–910, 1989.

[208] Y. Amatatsu, Y. Hamada, and M. Tsuboi, "FTIR detection of unstable molecules: infrared spectrum of 2-azabutadiene," *J. Mol. Spectrosc.*, vol. 123, no. 2, pp. 276–285, 1987.

[209] P. Gratier, L. Majumdar, M. Ohishi, E. Roueff, J. Loison, K. Hickson, and V. Wakelam, "A new reference chemical composition for TMC-1," *Astrophys. J. Supp. Ser.*, vol. 225, no. 2, p. 25, 2016.

[210] N. Sakai, T. Shiino, T. Hirota, T. Sakai, and S. Yamamoto, "Long carbon-chain molecules and their anions in the starless core, Lupus-1A," *Astrophys. J. Lett.*, vol. 718, no. 2, p. L49, 2010.

[211] B. Turner, "U93.174 – a new interstellar line with quadrupole hyperfine splitting," *Astrophys. J.*, vol. 193, pp. L83–L87, 1974.

[212] M. Agúndez, N. Marcelino, and J. Cernicharo, "Discovery of interstellar isocyanogen (CNCN): Further evidence that dicyanopolyynes are abundant in space," *Astrophys. J. Lett.*, vol. 861, no. 2, p. L22, 2018.

[213] A. M. Burkhardt, R. A. Loomis, C. N. Shingledecker, K. L. K. Lee, A. J. Remijan, M. C. McCarthy, and B. A. McGuire, "Ubiquitous aromatic carbon chemistry at the earliest stages of star formation," *Nat. Astron.*, vol. 5, no. 2, pp. 181–187, 2021.

[214] S. Manigand, A. Coutens, J.-C. Loison, V. Wakelam, H. Calcutt, H. Müller, J. K. Jørgensen, V. Taquet, S. Wampfler, T. Bourke, *et al.*, "The ALMA-PILS survey: first detection of the unsaturated 3-carbon molecules propenal ($C_2H_3CHO$) and propylene ($C_3H_6$) towards IRAS 16293–2422 B," *Astron. Astrophys.*, vol. 645, p. A53, 2021.

[215] D. Alberton, L. Bizzocchi, N. Jiang, M. Melosso, V. M. Rivilla, A. Pietropolli Charmet, P. Caselli, C. Puzzarini, S. Alessandrini, L. Dore, I. Jiménez-Serra, and J. Martín-Pintado, "Laboratory spectroscopy of allylimine and tentative detection towards the G+0.693-0.027 molecular cloud.," *Astron. Astrophys., Accepted*, 2022.

[216] J.-C. Guillemin and J.-M. Denis, "Flash vacuum thermolysis of $\alpha$-aminonitriles and subsequent HCN removal on solid base, a 'one line' multistep sequence to reactive n-methyleneamines," *J. Chem. Soc. Chem. Comm.*, no. 14, pp. 951–952, 1985.

[217] J.-C. Guillemin and J.-M. Denis, "Synthèse d'imines linéaires non-stabilisées par réactions gaz-solide sous vide," *Tetrahedron*, vol. 44, no. 14, pp. 4431–4446, 1988.

[218] N. Jiang, M. Melosso, L. Bizzocchi, S. Alessandrini, J.-C. Guillemin, L. Dore, and C. Puzzarini, "Spectroscopic and computational characterization of 2-aza-1,3-butadiene, a molecule of astrochemical significance," *J. Phys. Chem. A*, vol. 126, no. 11, pp. 1881–1888, 2022.

[219] D. Johnson, F. Lovas, C. Gottlieb, E. Gottlieb, M. Litvak, M. Guelin, and P. Thaddeus, "Detection of interstellar ethyl cyanide," *Astrophys. J.*, vol. 218, pp. 370–376, 1977.

[220] L. Margulès, R. Motiyenko, K. Demyk, B. Tercero, J. Cernicharo, M. Sheng, M. Weidmann, J. Gripp, H. Mäder, and J. Demaison, "Rotational spectrum of deuterated and $^{15}$N ethyl cyanides: $CH_3CHDCN$ and $CH_2DCH_2CN$ and of $CH_3CH_2C^{15}N$," *Astron. Astrophys.*, vol. 493, no. 2, pp. 565–569, 2009.

[221] L. Margulès, A. Belloche, H. Müller, R. Motiyenko, J.-C. Guillemin, R. Garrod, and K. Menten, "Spectroscopic study and astronomical detection of doubly $^{13}$C-substituted ethyl cyanide," *Astron. Astrophys.*, vol. 590, p. A93, 2016.

[222] S. Zeng, I. Jiménez-Serra, V. Rivilla, S. Martín, J. Martín-Pintado, M. Requena-Torres, J. Armijos-Abendaño, D. Riquelme, and R. Aladro, "Complex organic molecules in the galactic centre: the N-bearing family," *Mon. Not. R. Astron. Soc.*, vol. 478, no. 3, pp. 2962–2975, 2018.

[223] J. Cernicharo, M. Agúndez, R. I. Kaiser, C. Cabezas, B. Tercero, N. Marcelino, J. R. Pardo, and P. de Vicente, "Discovery of two isomers of ethynyl cyclopentadiene in TMC-1: Abundances of CCH and CN derivatives of hydrocarbon cycles," *Astron. Astrophys.*, vol. 655, p. L1, 2021.

[224] N. Balucani, "Elementary reactions and their role in gas-phase prebiotic chemistry," *Int. J. Mol. Sci.*, vol. 10, no. 5, pp. 2304–2335, 2009.

[225] J. P. Ferris and W. J. Hagan Jr, "HCN and chemical evolution: the possible role of cyano compounds in prebiotic synthesis," *Tetrahedron*, vol. 40, no. 7, pp. 1093–1120, 1984.

[226] P. Godfrey, R. Brown, B. Robinson, and M. Sinclair, "Discovery of interstellar methanimine (formaldimine)," *Astrophys. Lett.*, vol. 13, p. 119, 1973.

[227] F. J. Lovas, J. Hollis, A. J. Remijan, and P. Jewell, "Detection of ketenimine ($CH_2CNH$) in Sagittarius B2 (N) hot cores," *Astrophys. J. Lett.*, vol. 645, no. 2, p. L137, 2006.

[228] D. P. Zaleski, N. A. Seifert, A. L. Steber, M. T. Muckle, R. A. Loomis, J. F. Corby, O. Martinez Jr, K. N. Crabtree, P. R. Jewell, J. M. Hollis, *et al.*, "Detection of E-cyanomethanimine toward Sagittarius B2 (N) in the Green Bank Telescope PRIMOS survey," *Astrophys. J. Lett.*, vol. 765, no. 1, p. L10, 2013.

[229] R. A. Loomis, D. P. Zaleski, A. L. Steber, J. L. Neill, M. T. Muckle, B. J. Harris, J. M. Hollis, P. R. Jewell, V. Lattanzi, F. J. Lovas, *et al.*, "The detection of interstellar ethanimine ($CH_3CHNH$) from observations taken during the GBT PRIMOS survey," *Astrophys. J. Lett.*, vol. 765, no. 1, p. L9, 2013.

[230] V. Rivilla, J. Martín-Pintado, I. Jiménez-Serra, S. Zeng, S. Martin, J. Armijos-Abendano, M. Requena-Torres, R. Aladro, and D. Riquelme, "Abundant Z-cyanomethanimine in the interstellar medium: paving the way to the synthesis of adenine," *Mon. Not. R. Astron. Soc. Lett.*, vol. 483, no. 1, pp. L114–L119, 2019.

[231] L. Bizzocchi, D. Prudenzano, V. M. Rivilla, A. Pietropolli-Charmet, B. M. Giuliano, P. Caselli, J. Martín-Pintado, I. Jiménez-Serra, S. Martín, M. A. Requena-Torres, *et al.*, "Propargylimine in the laboratory and in space: millimetre-wave spectroscopy and its first detection in the ISM," *Astron. Astrophys.*, vol. 640, p. A98, 2020.

[232] L. Bizzocchi, V. Lattanzi, J. Laas, S. Spezzano, B. M. Giuliano, D. Prudenzano, C. Endres, O. Sipilä, and P. Caselli, "Accurate sub-millimetre rest frequencies for $HOCO^+$ and $DOCO^+$ ions," *Astron. Astrophys.*, vol. 602, p. A34, 2017.

# Acknowledgement

In particular, I would like to thank my two supervisors, Prof. Dr. Cristina Puzzarini and Dr. Mattia Melosso, who helped me so much during my PhD. I am grateful that they brought me into such an interesting research field that I particularly enjoy. There is a proverb in China: “Even if someone is your teacher for only a day, you should treat her/him like your mother/father for the rest of your life.” The knowledge and guidance my supervisors have taught me in these three years will benefit me for the rest of my life!

I would like to thank Dr. Luca Bizzocchi for his help both in the thesis and experiments! And I would like to thank my colleagues in the ROT&Comp group, Dr. Silvia Alessandrini, Alessio Melli, Francesca Tonolo, and Hexu Ye, for their help in my research and in my life. There are 7 billion people in this world. How fortunate I am to have met you all!

I would also like to thank China Scholarships Council (CSC) for financial support. Finally, I would like to thank my boyfriend, Wentao Song, and my family for their support and assistance, both in life and in my studies. Due to the pandemic, I haven’t gone back to my hometown for three years, and my parents have kept giving me courage and power from about 8000 kilometres away.

The spectrum of a molecule may well be predicted, while life is not. Life is never easy. What we can do is try our hardest every day and leave the rest to God!